RSC Advances

REVIEW

View Article Online
View Journal | View Issue

Cite this: *RSC Adv.*, 2020, **10**, 31622

Spinel ferrite (AFe_2O_4)-based heterostructured designs for lithium-ion battery, environmental monitoring, and biomedical applications

Tuyet Nhung Pham, [a] Tran Quang Huy [ac] and Anh-Tuan Le *[ab]

The development of spinel ferrite nanomaterial (SFN)-based hybrid architectures has become more popular owing to the fascinating physicochemical properties of SFNs, such as their good electro-optical and catalytic properties, high chemothermal stability, ease of functionalization, and superparamagnetic behaviour. Furthermore, achieving the perfect combination of SFNs and different nanomaterials has promised to open up many unique synergistic effects and advantages. Inspired by the above-mentioned noteworthy properties, numerous and varied applications have been recently developed, such as energy storage in lithium-ion batteries, environmental pollutant monitoring, and, especially, biomedical applications. In this review, recent development efforts relating to SFN-based hybrid designs are described in detail and logically, classified according to 4 major hybrid structures: SFNs/carbonaceous nanomaterials; SFNs/metal–metal oxides; SFNs/MS_2; and SFNs/other materials. The underlying advantages of the additional interactions and combinations of effects, compared to the standalone components, and the potential uses have been analyzed and assessed for each hybrid structure in relation to lithium-ion battery, environmental, and biomedical applications.

Received 11th June 2020
Accepted 6th August 2020

DOI: 10.1039/d0ra05133k

rsc.li/rsc-advances

[a]*Phenikaa University Nano Institute (PHENA), Phenikaa University, Hanoi 12116, Vietnam. E-mail: tuan.leanh@phenikaa-uni.edu.vn*

[b]*Faculty of Materials Science and Engineering, Phenikaa University, Hanoi 12116, Vietnam*

[c]*Faculty of Electric and Electronics, Phenikaa University, Hanoi 12116, Vietnam*

Tuyet Nhung Pham received an Engineering Degree in Chemical Engineering Technology from Ha Noi University of Mining and Geology, Vietnam, in 2017, and then she received a Master's Degree in Nanomaterials from Gachon University, South Korea, in 2019. Now, she is working as a Researcher at Phenikaa University Nano Institute (PHENA), Vietnam. Her current research focuses on developing advanced nanomaterials for lithium-ion battery, cosmetic, and environmental applications.

Dr Tran Quang Huy is a biophysicist. He obtained his PhD in Materials Science from Hanoi University of Science and Technology (HUST), Vietnam, in 2012. He worked at the National Institute of Hygiene and Epidemiology (NIHE), Hanoi, as a researcher from 2001–2019. He also had responsibilities as Vice-Editor in Chief of the Vietnam Journal of Preventive Medicine (2016–2019); Chair of the Vietnam Young Academy for the term of 2017; and a member of the Global Young Academy (GYA) for the term of 2017–2022. In August 2019, he moved to work at Phenikaa University, Vietnam, as Vice-Director of the Phenikaa University Nano Institute (PHENA). His research has focused on the ultra-small world of nanotechnology applied to the biomedical field, including innovative biosensors/biochips, and bio-nanomaterials applied to the rapid detection of infectious pathogens, disinfection, and environmental monitoring.

1. Introduction

In the past decade, spinel ferrite nanomaterials (SFNs) have emerged as an advanced class of nanostructured material in the fields of nanoscience and technology due to their extremely prominent features at nanometric sizes. A series of scientific reports concerning new synthetic methods and techniques relating to SFNs has been made.[1–3] It was found that through varying or modifying the fabricating technologies, SFNs can be produced with many varied morphologies, such as zero-dimensional (0D) nanoparticles (NPs) and nanospheres, one-dimensional (1D) nanotubes, nanowires, and nanofibers, two-dimensional (2D) nanosheets and nanoplates, and three-dimensional (3D) nanofoams and nanoflowers. More particularly, each particular SFN morphology shows unique, distinctive characteristics corresponding to its spatial structure. However, despite differences in morphology, these structures still share the common significant advantages of a typical spinel structure, such as showing superparamagnetic behavior and excellent physicochemical properties, like optical, electrical, and catalytic properties, a high aspect ratio, chemical and thermal stability, and easy functionalization. Apart from the above-mentioned noteworthy properties, toxicity, low surface area, and poor dispersibility can also be found, which result in many limitations in relation to the widespread application of SFNs. Furthermore, there is a lack of in-depth fundamental knowledge about the properties of SFNs, leading to many difficulties in taking advantage of the merits of SFNs and in solving the issues relating to each application. This fact, combined with their unique features, has motivated the strong explosion in the number of studies and reviews examining their potential use in energy storage, environmental pollutant monitoring, and biomedical applications.

When looking at the recent nanostructured SFN development trend for energy storage applications, almost all interest has been devoted to lithium-ion batteries (LIBs) because of their performance superiority in terms of energy capacity, cycle life, and energy density, and easier construction process, compared with others.[4] There is no denying that the presence of SFNs in the electrode material can offer many positives for LIBs, such as higher electrical conductivity and theoretical specific capacity, better surface electrochemical reactivity, and lower cost, which would be promising for sufficiently meeting the increasing demand for energy generation. This has been demonstrated *via* some brief review reports relating to the utilization of SFNs in energy storage and conversion devices, in which the mechanisms and the effects of morphology and structure on LIB electrochemical performance were proposed and investigated in detail.[2,5] Along with this, these reports pointed out promising future strategies for overcoming current issues and optimizing the SFN performance space, surface area, and size in SFN-based electrodes. Significant findings and achievements have been obtained in the environmental treatment field due to SFNs possessing excellent magnetic properties, high adsorption capacities, good stability, safety, and good optoelectronic tunability. This has paved promising paths to enhancing pollutant removal efficiencies in terms of both quantity and quality *via* adsorption and photodegradation process, and improved reusability thanks to the easing of recovery under an external magnetic field.[6] In addition, another discovery is the start of the development of new SFN-based sensors to detect pollutants in an early manner at low concentrations, with low production costs and simple fabrication techniques while maintaining high selectivity and sensitivity. Some recent excellent review articles have once again confirmed that using SFs is one of the most suitable approaches for purification applications that require high efficiencies and rapid kinetics. Some key parameters that directly affect the removal efficiencies of metal ions, dyes, and pharmaceuticals, like size, shape, treatment temperature, and surface modification, have been discussed.[3,7] Furthermore, it should be noted that the use of SFNs may become inevitable, as they have been assessed as having many potential advantages for biomedical applications owing to their low toxicity, high biocompatibility, high physicochemical stability, ease of fabrication, tunable size and shape, and great superparamagnetic behavior. Also, their unique physiochemical properties make SFNs more particularly attractive for various applications such as drug delivery, magnetic resonance imaging (MRI), magnetic hyperthermia, and bio/chemosensor use.[1,8,9]

Additionally, it seems that special attention is being shifted towards the development of SFN-based heterostructured

Professor Anh-Tuan Le received his PhD in Materials Science and Engineering from Chung Nam National University at Daejeon City in South Korea in 2007. He has been a fellow of the Vietnam Society of Materials Science, the Vietnam Society of Physics, and the Vietnam Society of Magnetism and Magnetic Physics from 2008 to date. He worked as a lecturer and Associate Professor at the Department of Nanoscience and Nanotechnology in Hanoi University of Science and Technology, Vietnam, from 2008–2019. He moved to Phenikaa University, an emerging university in Vietnam, worked as the Director of the Phenikaa University Nano Institute (PHENA) from Feb 2019, and was promoted to Full Professor of Materials Science in Dec 2019 at the Phenikaa University. He was also appointed as a group leader for a key research group in Phenikaa University: Nanomaterials for Environmental and Biomedical Applications (NEB) Group (http://neblab.phenikaa-uni.edu.vn). His research interests include magnetic nanomaterials, colloidal plasmonic metal nanocrystals, metal oxide nanoparticles, 2D nanomaterials, hybrid/composite nanostructures, innovative bio/chemo-sensing technologies, and the utilization and realization of multidimensional nanomaterials and their hybrid composites in different technological fields, such as the biomedical, environmental, agricultural, and energy nanotechnology fields.

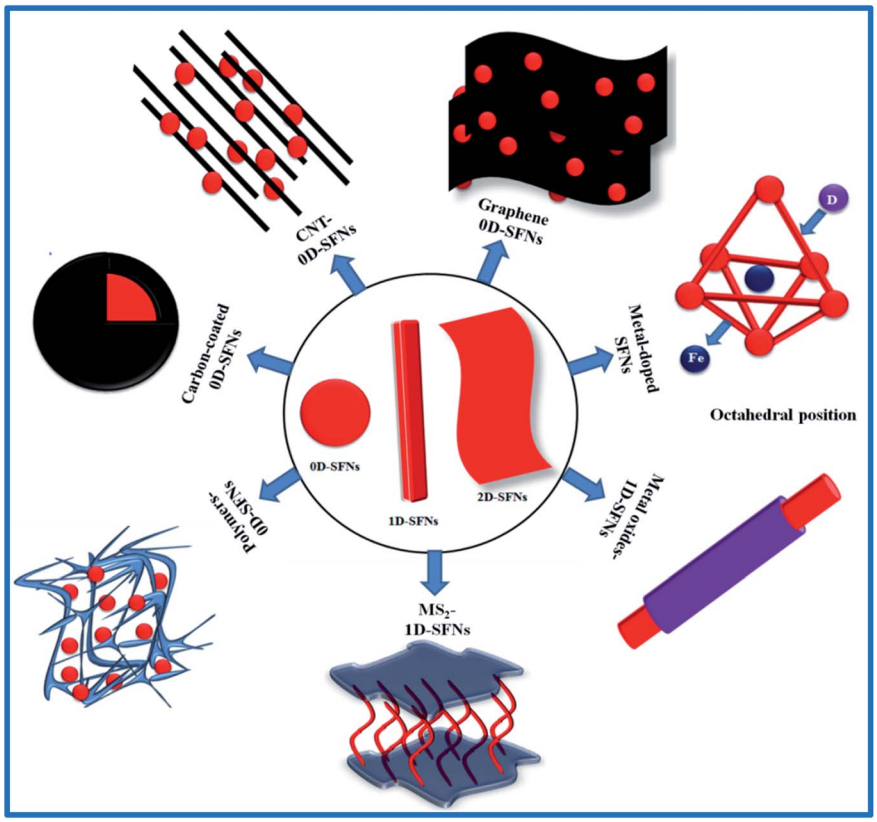

Fig. 1 The formation of spinel ferrite (AFe_2O_4)-based heterostructured designs with various nanomaterials.

designs. According to a large number of published reports, this development trend is considered to-date to be an impressive achievement in the nanostructured material production field.[7,10–12] It is undeniable that the large number of combinations between SFNs and other nanomaterials, such as carbonaceous materials (carbon coatings, carbon nanotubes (CNTs), graphene, graphene oxide (GO), *etc.*), metals, metal oxides, transition-metal dichalcogenides (TMDs), and polymers, has helped to form heterostructures possessing special synergistic effects and has had many further dramatic effects on their properties with respect to the single SFN counterparts (Fig. 1). In general, there has been a rapid increase in the number of recorded positive results from SFN-based design models to date; most of these arise from optimizing the performances and unique features of the constituents through changes to the individual components, design morphology, and synthesis techniques. Unfortunately, these reports are limited to only describing and evaluating in a fairly general way the obtained positive results to clarify their potential for use for each different application. Up to now, no comprehensive and detailed evaluations of the hybridization between SFNs and other nanomaterials have been found, and the basis of the tight relationships between the structural parameters, morphology, and magnetic, physicochemical, and electrochemical properties has not been discussed. Notably, a fuller and better in-depth understanding of the innovative behaviors and characteristics of these hybrid designs will help not only to gain a complete overview of the development trend but it will also help to pave potential development pathways in the future. Therefore, in this review, we have tried to present the most exhaustive and logical picture of SFN-based hybrid designs for LIB applications, environmental monitoring, and biomedical applications. For each design, the addition interactions, synergistic effects, and important changes due to the presence of other nanomaterials in the spinel ferrite structure were discussed. More interestingly, from these assessments, a few promising approaches have also been proposed for taking maximum advantage of the potential of SFNs and further developing them for practical applications.

2. Spinel ferrite (AFe_2O_4) nanomaterials

2.1. The structural characteristics of spinel ferrite (AFe_2O_4) nanomaterials

Like other spinel crystal structures, the most interesting point about most SFNs is their chemical composition and structure. A spinel ferrite is a complex oxide crystal structure with a face-centered cubic core and a unit formula of AFe_2O_4. This can be formed from the combination of a trivalent cation (Fe^{3+}) and another divalent metallic cation, such as either a transition or post-transition metallic cation (A = Mn, Mg, Co, Ni, Zn).[8,13] With differences in both chemical nature and charge state, as well as stabilization energy, these cations may be arranged according to

two different crystallographic sites (tetrahedral sites and octahedral sites) situated between the cations and surrounding oxygen ions.[14] More specifically, one AFe_2O_4 unit consists of 32 closely packed oxygen atoms with 64 divalent tetrahedral sites and 32 trivalent octahedral sites; in particular, to maintain an electrically balanced state between the anions in the structure, A^{2+} and Fe^{3+} usually occupy 8 tetrahedral and 16 octahedral sites, respectively.[15–17] Also, based on the positions of these cations, a spinel ferrite structure can be classified into 3 groups: normal, inverse, and mixed. In fact, the site occupation mainly depends on the electrostatic contribution to the lattice energy, the cation radii, cation charges, and crystal field effects. In a typical spinel ferrite structure, the A^{2+} cations are located at tetrahedral sites, while Fe^{3+} cations are found at octahedral sites, for example in $ZnFe_2O_4$, which is similar to some other spinel crystalline structures such as $CoAl_2O_4$,[18] $MgAl_2O_4$, and Mn_3O_4.[19] For the inverse spinel structure, Fe^{3+} cations are equally distributed between tetrahedral and octahedral sites while A^{2+} cations only occupy octahedral sites, for example in $NiFe_2O_4$, $CoFe_2O_4$,[20,21] Fe_3O_4, *etc.* In a mixed spinel structure, A^{2+} and Fe^{3+} cations randomly occupy both sites, as in $MgFe_2O_4$ (ref. 13) and $MnFe_2O_4$.

In 1945, L. Néel *et al.*[16] investigated the exchange interactions and cationic distributions in spinel ferrite nanostructures to evaluate their magnetic properties. Most recent reports have also illustrated that the unique features of the spinel ferrite structure are remarkably affected by their chemical composition, particularly the divalent cations rather than Fe^{3+} cations. To explain this more clearly, we can observe the following simple equation for determining the lattice parameter (α) according to the positions of the A^{2+} and Fe^{3+} cations:

$$a_{th} = \frac{8}{3\sqrt{3}}\left[(r_a + r_o) + \sqrt{3}\,(r_b + r_o)\right]$$

where r_o is the ionic radius of an oxygen anion, and r_a and r_b are the ionic radii of the A^{2+} and Fe^{3+} sites. As described, the arrangement of A^{2+} and Fe^{3+} cations, the charge state, and the chemical composition of the lattice crystal structure not only directly affect the lattice structural parameters but also change the geometry and ion bonding energy between the cations and surrounding oxygen ions, leading to alterations of the physicochemical properties.[22] According to this, each spinel ferrite classification should possess an individual electronic configuration and special physicochemical properties, such as optical, electrical, catalytic, and intrinsic magnetic properties.

2.2. Synthetic methods for obtaining various spinel ferrite (AFe_2O_4) nanomaterials

More than for other synthetic nanomaterials, the choice of synthetic methodology used for spinel ferrites is in particular considered to be one of the most crucial factors for creating various nanostructures with many unique features in terms of size, shape, orientation, aspect ratio, surface area, purity, and stability. In previous reports, some potential synthetic techniques for the preparation of SFNs based on top-down and bottom-up approaches have been mentioned, for instance, co-precipitation, hydrothermal methods, sol–gel methods, microwave methods, electrochemical deposition processes, and microemulsion methods as bottom-up approaches,[2,6,23–26] and milling and pulsed laser ablation methods as top-down approaches.[27,28] Firstly, it should be stressed that a co-precipitation strategy is the most effective simple method for synthesizing SFNs because it involves the physical mixing of metallic salts containing divalent and trivalent cations at a molar ratio of 1 : 2. After mixing, the above mixture is heated up and some precipitating agents are added (KOH, NaOH, NH_3) until a condensation reaction occurs between the two metallic salts in parallel. During the reaction process, an increase in the concentration of hydroxyl groups in the mixture leads to the formation of oxygenated bridges between species, which are a source of oxygen bonds in SFNs after conversion.

Secondly, hydrothermal and solvothermal processes are also facile and effective strategies leading to high purity and controllable morphology. In these methodologies, a large amount of heat energy is provided to form the crystalline ferrite phases. There is a clear difference between the hydrothermal and solvothermal methods. Instead of using water as a solvent to dissolve the metal precursors under high pressure and at moderate temperature, as in a hydrothermal process, a solvothermal process uses other chemicals as solvents, such as methanol, ethanol, and ethylene glycol. Similarly, by using heat energy, microwave methods can be used to obtain more uniform spinel nanostructures and nucleation, together with showing shorter reaction times, better selectivity, and higher reaction rates compared with standard heating processes (conduction, irradiation, and convection). However, this approach, in fact, faces some problems arising from poor solvent penetration.

Thirdly, sol–gel methods have also assessed as an important way to prepare SFNs with high purity and homogeneity, and large porosity. In this approach, after sol formation occurs, the obtained product can be converted to gel form and then calcinated under suitable conditions to get the desired structures. Another method employed in this field is a microemulsion approach, which is based on the formation of a micelle structure stemming from the combination of a polar solvent and a nonpolar solvent. Each micelle plays a role as a microreactor to create SFNs. As can be seen, in recent years, much great effort has been devoted to the research and development of new synthetic methods that are more environmentally friendly to enhance synthetic efficiency and crystalline growth, as well as to create many varied SFNs with more abundant morphologies, compositions, and sizes. This trend seems to be very promising, as the requirements of the nanotechnology field are becoming more and more complicated and difficult to meet.

2.2.1. 0D spinel ferrite (AFe_2O_4) nanomaterials. As is known, zero-dimensional nanomaterials (0D-NMs) are some of the most popular synthetic materials used for many applications because of their ease of synthesis and many unique morphology, size, and structural features. More interestingly, the development of 0D NMs has been found in the SFN area. As mentioned, simple techniques have been employed to fabricate uniform 0D spinel ferrite nanomaterials (0D-SFNs), including

co-precipitation, hydrothermal,[29] solvothermal, microwave, sol–gel,[30,31] and microemulsion[32] methods. Most of these techniques can be used to create spinel ferrite NPs meeting all requirements in terms of size and shape, but they are not practical enough when applied on a large scale because of high costs, complicated procedures, large energy demands, long reaction times, and environmental unfriendliness. To overcome these limitations, some innovations for preparing 0D-SFNs have been proposed and investigated, and some precursors and reagents used in the synthetic reaction have been replaced with more eco-friendly materials, such as egg white[33] and *Limonia acidissima* juice,[34] instead of utilizing toxic chemicals. With natural reducing agents, the obtained 0D-SFNs still exhibit the formation of a cubic spinel crystal structure with a size range from 20 nm to 60 nm and many inherent characteristics (ferromagnetic behavior, and photodegradation and antibacterial activities). Also, new synthetic techniques have been created using a thermal treatment process in a solution containing polyvinyl pyrrolidone (PVP), metal salts, surfactant, and deionized water[35,36] to replace water and ethanol in previous standard approaches. In this case, PVP and the surfactant play stabilizing and protecting roles during 0D-SFN formation, avoiding aggregation. Such methods have shown remarkable advantages, such as simplicity, low cost, the use of low reaction temperatures, and a lack of toxic by-products. Along with using new solutions, some post-treatment strategies, for example, grinding and calcination, have also demonstrated efficiency for improving synthetic performance when combined with other methods.[35]

2.2.2. 1D spinel ferrite (AFe_2O_4) nanomaterials. One-dimensional SFN nanostructures (nanowires, nanotubes, nanorods, and nanobelts) have attracted tremendous attention because of their orientation abilities, size, and many shape-dependent properties, for instance, magnetism, mechanical hardness, biocompatibility, and high stability. They have been widely used for many potential applications, such as in selective catalysis, chemical and biological sensors, photocatalysts, environment treatment, energy storage, and biotechnology. In some reports, traditional methods, such as hydrothermal,[37,38] solvothermal,[39] co-precipitation, electrospinning,[40–42] and microemulsion methods,[43] have been chosen to manufacture 1D-SFNs. However, these methods must overcome challenges because the high symmetry of the spinel structure remarkably prevents 1D-NM growth. To address this problem, many researchers have examined ways to innovate traditional methods. Namely, in reports by X. Hou and N. Wang, a common hydrothermal method was combined with a seed growth method to create 1D-SFNs with more uniform size and morphology.[44,45] Template-assisted methods were used in another case to fabricate high-quality 1D-SFNs. The presence of hollow 1D structures in the limited template space within the pores facilitated the formation of 1D-SFNs when combined with some different post-treatment processes, such as oxidation, sol–gel, thermal decomposition, chemical vapor deposition, and liquid phase deposition methods. Herein, anodic aluminum oxide (AAO),[46–49] CNTs,[50,51] and ordered mesoporous SiO_2 (SBA-15)[52] were used as promising templates for this approach. More particularly, Menchaca-Nal *et al.*[53] also chose bacterial cellulose nanoribbons as templates for the manufacture of cobalt ferrite nanotubes with a size of 217 nm at low temperature (90 °C). It needs to be stressed that the obtained 1D-SFNs showed higher surface area, larger porosity, more excellent flexibility and conductivity, and controllable morphology and size. In the most recent report, a green synthesis technique using rosemary extract was introduced for first time by Alijani *et al.*[54] It has been shown to be a fast, simple, industrially viable, and versatile approach, being non-toxic with low fabrication costs.

2.2.3. 2D spinel ferrite (AFe_2O_4) nanomaterials. 2D-SFNs offer exciting opportunities and challenges for many varied practical applications due to their fascinating physicochemical properties. However, up to now, studies and reports about SFN applications have mainly focused on 0D, 1D, and 3D nanostructures. In contrast, there are only a few reports related to 2D nanostructures. To explain this, it can be noted that SFNs are not, in fact, materials with an intrinsically layered structure, and they cannot be mechanically or chemically exfoliated to create 2D nanostructures as with other 2D NMs. Therefore, it is very complicated and difficult to fabricate 2D-SFNs, and this demands the further development of bottom-up strategies. Like the development trend relating to the preparation of 1D-SFNs, some enhancements of fabrication processes based on inherently basic methods have been proposed and investigated. Particularly, in research by Cao's group[55] and Sivakumar's group,[56] with the assistance of a polymer, urea, and oleic acid, co-precipitation techniques demonstrated positive merits in terms of effectiveness and controllable crystallinity without any aggregation of 2D-SFNs. In this approach, the support substances had roles as mineralizers and morphology controlling agents during the fabrication process. A similar strategy was found by Sivakumar *et al.*,[57] utilizing ethylene glycol, citric acid, and PVP to assist a sol–gel auto-combustion technique. Interestingly, a hydrothermal approach was also developed *via* a series of carboxylic-acid-, polymer-, and urea-assisted reactions, followed by some post-heating processes. As a result, these support substances could significantly affect the specific surface areas and crystallinities of spinel ferrite nanosheets and nanoplates.[58–60] Also, some new techniques relating to molten-salt systems[61] and hard templates have been reported. Peng *et al.* and Gao *et al.*[60,62] explored general strategies for the versatile synthesis of holey $CoFe_2O_4$ nanosheets and porous $ZnFe_2O_4$ nanosheets with tunable pore sizes using GO and graphene sheets as sacrificial hard-templates, respectively. Obtaining 2D structures, they opened up many opportunities for energy storage and conversion applications, as well as gas sensor designs with high sensitivity, good selectivity, and low operating temperatures due to synergistic effects assisting inherent long-term chemical/mechanical stability and enhanced charge transport properties.

2.2.4. 3D spinel ferrite (AFe_2O_4) nanomaterials. Recently, 3D-SFNs have been studied and fabricated more widely *via* a variety of routes, as demonstrated by the large number of reports in the literature. 3D-SFNs, but also other 3D NMs, attract much attention because of the unique features arising from the successful combination of all the merits of nanoscale building

blocks into one unit. In fact, among the available synthesis methods for 3D-SFNs, template routes, including hard-template and soft-template methods, are some of the most popular methods found. For the hard-template method, a coating of spinel ferrite is created first on a hard template, such as polystyrene spheres[63] or carbon spheres,[64,65] *via* controlled surface precipitation, and then the template can be removed *via* thermal or chemical means to form hollow spheres. In contrast, for soft-template technology, vesicles, micelles, and emulsions are often chosen as templates. The use of some basic approaches (solvothermal and hydrothermal methods) combined with innovative processes arising from ionic liquid and polymer support in the reaction mixture (chitosan (CS) and ethylene glycol) can also provide many promising results.[66–68] Indeed, these polymers act as substances that can limit the core growth of SFNs during preparation and help stabilize SFNs *via* steric repulsion when NPs are dispersed in aqueous media. S. Briceño *et al.*[69] reported that the solvothermal synthesis of cobalt ferrite with the support of CS resulted in the best yield of hollow spheres with a narrow size distribution. Also, other reports have exhibited more facile and efficient new methods utilizing vapor diffusion synthesis or vapor-phase polymerization methods to generate spinel ferrites.[70,71]

2.3. Advanced properties of spinel ferrite (AFe_2O_4) nanomaterials

2.3.1. Magnetic properties. As mentioned, one of the most important properties of SFNs is their strong magnetic features. In common SFNs, these magnetic properties are drastically influenced not only by the distribution and valence of cations, but also by the electronic configuration between tetrahedral and octahedral sites within the crystalline structure. Besides the synthesis process, particle size, crystal domain structure, and surface/interface effects have all been evaluated as other important factors that can affect the magnetic properties, including coercivity (H_c), remanent magnetization (M_r), and saturation magnetization (M_s). Namely, in some previous reports, the formation of spinel ferrite particles through solid-state reactions and/or deposition methods resulted in high inversion degrees, similar to bulk materials.[3,72] Meanwhile, the use of more complex methods like hydrothermal synthesis, thermal decomposition, or micelles led to non-equilibrium cationic distributions in the structures of SFNs. The relationships between particle size, crystalline properties, and magnetic properties were also reported in Liu's study where the critical size to obtain the maximum M_r and H_c values was found to be approximately 76 nm, which is consistent with the critical size of 76 nm estimated theoretically for the transition from single to multidomain behaviour. Furthermore, it was demonstrated that differences in the crystalline properties of cube- and sphere-like NPs resulted in their different magnetic performances; here, the recorded M_r and H_c values for sphere-like NPs were lower than those for cube-like NPs (Fig. 2).[73] Along with that, complex surface/interface interactions and size effects arising from the breaking of the symmetry of exchange bonds at the boundary of the particle surface are also crucial for

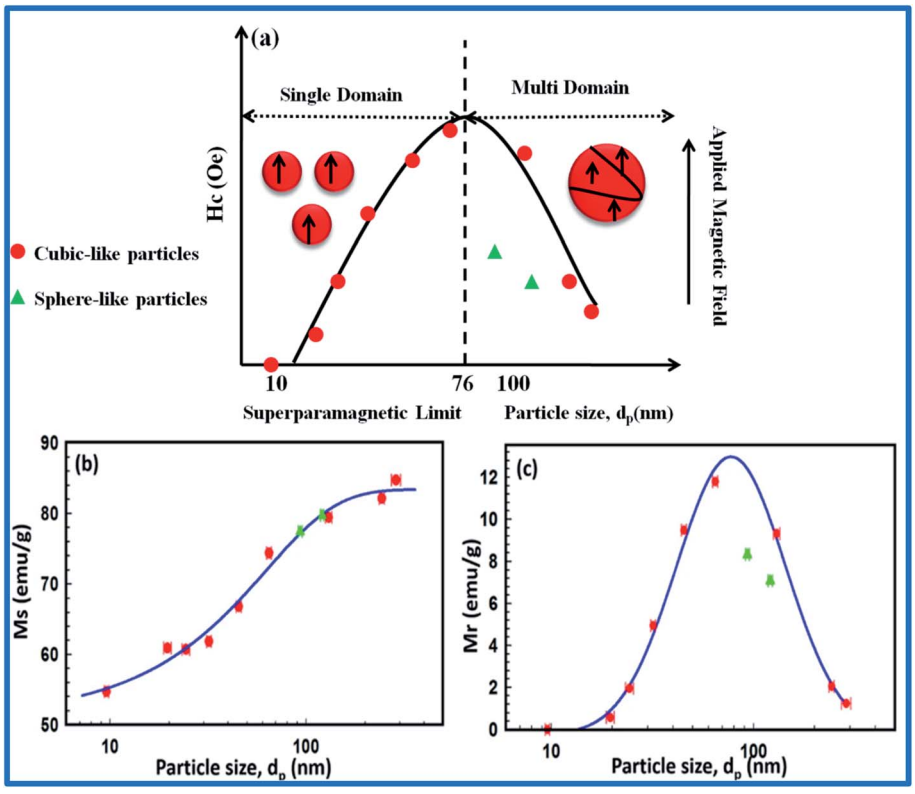

Fig. 2 The particle size dependence of (a) coercivity (H_c); (b) saturation magnetization (M_s); and (c) remanent magnetization (M_r) for cube-like and sphere-like morphologies of Fe_3O_4 nanoparticles (reprinted with permission from ref. 73; copyright: 2017, Springer Nature).

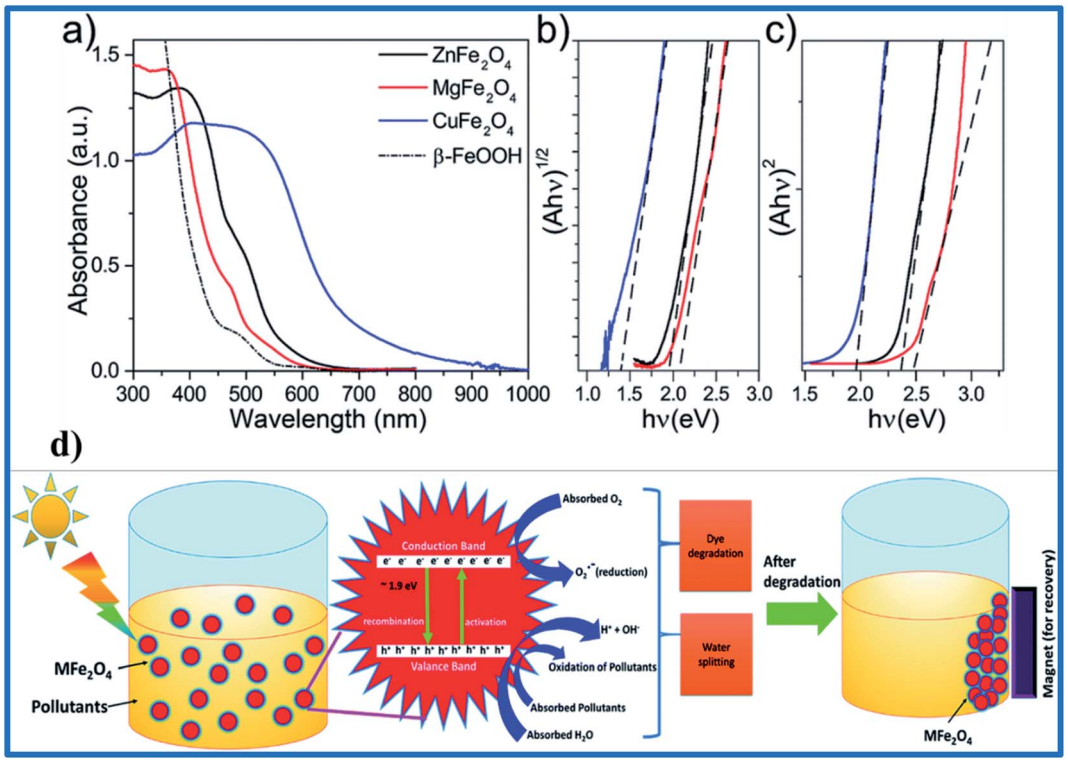

Fig. 3 Thin film UV-vis absorption spectra of β-FeOOH, $CuFe_2O_4$, $MgFe_2O_4$, and $ZnFe_2O_4$ (a) and corresponding Tauc plot analysis of the indirect optical band gap (b) and direct optical band gap (c) energies. A schematic diagram of pollutant degradation and water splitting using spinel ferrite based photocatalysts under solar light irradiation (d) (reprinted with permission from ref. 75 and 76; copyright: 2018, The Royal Society of Chemistry).

determining the magnetic behavior *via* the formation of spin canting at the particle surface. The simplest instance of surface/interface and size effects is the superparamagnetic behavior of SFNs. Instead of the presence of a multidomain phase in bulk materials, a reduction in size in the nano-range from 15 to 100 nm helps a SFN transform into a single-domain structure where the atomic spins of the SFN are aligned in the same direction. Each such single domain of particles can be considered as a "*superspin*" structure with superparamagnetic behavior.[74] Under an applied external magnetic field, all SFN single domains exhibit a strong and fast magnetic response, however, they do not exhibit any residual magnetic momentum when the magnetic field is removed, which is very different compared with conventional paramagnetic materials. With such unique properties, SFNs promise to be excellent contrast agents with high image contrast, high MRI sensitivity, and good specificity, as well as being potential targeting drug-loaded nanocarriers for biomedical and industrial applications. Magnetic anisotropy is also an interesting property of SFNs; this depends on the anisotropy of the cations, the symmetry of the interstitial sites, and also the chemical composition and cationic distribution. Besides, in a single domain structure, the shape anisotropy, surface anisotropy, and cationic interactions all contribute to enhancing the total magnetic anisotropy.[72] Understanding the intercorrelation between these factors can allow the magnetic structure and magnetic properties to be tailored effectively.

2.3.2. Adsorption properties. The great adsorption properties of spinel ferrite nanostructures are attributed to their unique physicochemical features and nanoscale effects. By varying the synthetic method used, SFNs of different sizes and shapes can be fabricated successfully, also generating high aspect ratios, versatile surface functionalities, and tunable magnetic properties. Although SFNs have rather low specific surface areas compared with those of other adsorbents (graphene and active carbon), nano-sized spinel ferrite materials exhibit greater advantages related to a rise in the percentage of atoms and number of reactive sites on the surface through corners, edges, and defects, leading to enhanced SFN adsorption capacities and sorption kinetics.[7] More interestingly, the size, morphology, and chemical composition of a SFN remarkably affect the specific surface area, stability, and, particularly, adsorption efficiency. As described in Reddy's report, an SFN adsorption mechanism was proposed based on the formation of new chemical bonds, like hydrogen bonding, and/or the weak interactions, like π–π interactions, electrostatic interactions, and even chemisorption processes, ion-exchange, and surface complexion.[3] The surface also contains many hydroxyl groups (M–OH and Fe–OH), which are determined to be major binding sites for adsorbates. According to this, the size, morphology, and chemical composition of a SFN can change the number of hydroxyl groups and their exposure to adsorbates, affecting directly the physicochemical interactions between adsorbate and adsorbent, and then, of course, the adsorption efficiency.

2.3.3. Optoelectronic tunability. SFNs are seen as an emerging semiconductor family that has recently attracted increasing attention for photocatalytic applications and sensor technologies because of their great optoelectronic tunability, high energy density, remarkable thermal and chemical stabilities, natural abundance, and cost effectiveness. From a structural point of view, it can be seen that variation of the cation type leads to a slight change in bandgap energy, approximately from 1.4 to 2.7 eV, suggesting a promising pathway to develop new semiconductors that are appropriate for absorbing visible light, especially for photocatalytic applications (Fig. 3).[75,76] Similar to other photocatalysts, the basic photocatalytic mechanism relating to SFNs has been proposed, based on the following equations:

$$AFe_2O_4 + h\nu \rightarrow h^+ + e^-$$

$$h^+ + OH^- \rightarrow OH^{\bullet}\ \text{(hydroxyl radicals)}$$

$$OH^{\bullet} + O^{2-}\ \text{(active oxygen species)} + \text{organic matter or pollutants} \rightarrow CO_2 + H_2O$$

Under excitation by the sun or another light source, negative electron (e^-) and positive hole (h^+) pairs are created on the SFN surface. These e^-/h^+ pairs directly join in the formation process of hydroxyl radicals or superoxide anions, which play key roles in removing organic matter or pollutants. Despite this, overall evaluations of the optoelectronic properties of SFNs themselves are still limited. The utilization of SFNs is restricted by their poor electron transfer activities, difficult dispersibility, and low surface areas, as well as the fast surface and bulk recombination of e^-/h^+ pairs.[77,78] Herein, reducing the size and controlling the morphology and chemical composition, along with enhancing and modifying the SFN surface and selecting suitable hybrid materials, are considered as crucial key strategies to increase the number of active sites for catalysis and shorten the diffusion lengths for e^-/h^+ pairs, making it easier for charge carriers to transfer to the surface rather than recombine in the bulk.

2.3.4. Targeted delivery properties. One of the most interesting innovative properties of SFNs is targeted delivery using their superparamagnetic properties for biomedical applications. As described above, all the domains within the spinel ferrite nanostructure are aligned in the direction of an applied external magnetic field, creating a large magnetic momentum, which allows for control of the orientation and location of smart spinel ferrite nanocarriers without the appearance of self-aggregation phenomena when the external magnetic field is removed. *Via* applying an external stimulus, such as a magnetic field, ultrasound, temperature, or light, and/or changing some internal triggers, like the presence of enzymes or pH, an efficient release process can be carried out (Fig. 4a).[9] Due to this tightly controlled process, magnetic nanocarriers offer significant positive impacts, improving pharmacokinetics, increasing dispersion, increasing the stability of the loaded contents, enhancing the retention time of delivery systems in the circulatory systems, and reducing the concentration of the loaded contents and toxic side effects.

2.3.5. Hyperthermia properties. Along with impressive targeted delivery, the magnetic hyperthermia properties of SFNs based on the conversion of electromagnetic energy into heat in the presence of an external alternating current magnetic field are also very attractive. As we know, cancerous tumors are susceptible to increasing temperature; unfortunately, during conventional hyperthermia treatments, such as regional hyperthermia and whole-body hyperthermia, besides destroying cancer cells, some clinical side effects are felt by surrounding healthy tissues.[79,80] However, one of the most outstanding characteristics of using SFNs inside tumors is the

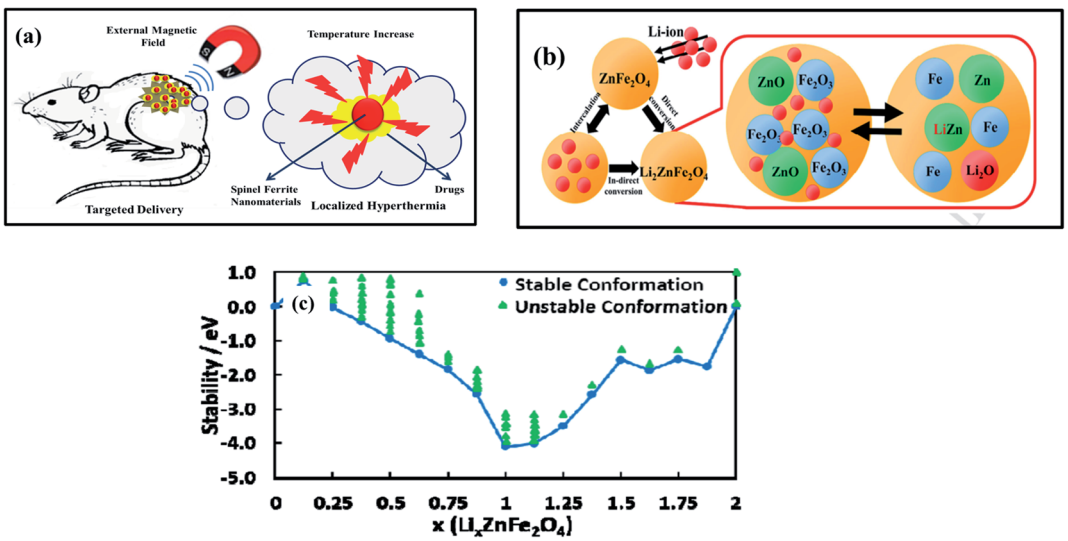

Fig. 4 (a) A schematic illustration of the magnetic behavior according to the SFN particle size and applications in targeted delivery and localized hyperthermia treatment. (b) The intercalation of lithium ions in $ZnFe_2O_4$. (c) The relative stability of $Li_xZnFe_2O_4$ configurations relative to $ZnFe_2O_4$ and $Li_2ZnFe_2O_4$ (reprinted with permission from ref. 84 and 85; copyright: 2019, Elsevier Ltd, and copyright: 2017, The Royal Society of Chemistry, respectively).

good and fast focusing of heating in the tumor zone (localized hyperthermia). More interesting, the perfect combination of targeted delivery and magnetic hyperthermia can improve the vascular permeability of SFNs and lead to the more efficient accumulation of SFNs. Also, magnetic hyperthermia can significantly affect the release efficiency of loaded contents from smart nanocarriers at the tumor site.[9] Interestingly, the utilization of SFNs with localized heating effects that do not harm the surrounding tissues promises to be a fascinating therapeutic procedure for cancer therapy.

3. The development of heterostructured designs for lithium-ion battery, environmental monitoring, and biomedical applications

3.1. Challenging aspects of spinel ferrite (AFe_2O_4) nanomaterials for technological applications

3.1.1. Spinel ferrites (AFe_2O_4) for lithium-ion battery applications. As is known, the performance of LIBs depends remarkably on the electrode material components and structural characteristics. Of these, the anode material components are attributed as one of the most important factors affecting the energy storage efficiency. Normally, there are three popular anode material types, carbonaceous materials (graphite, graphene, and GO), conducting polymers, and transition metal oxides (TMOs), however, their use has been limited by low theoretical capacities and instability during cycling. Recently, the development of novel anode materials that could fulfil the demands of LIBs in terms of having high power and energy densities and electrochemical stability has been recorded based on the use of binary metal oxides (spinel materials), especially spinel ferrites (AFe_2O_4, where A can be Zn, Ni, Co, Mg, Mn, *etc.*) and their heterostructured designs, in the electrode structure.

Among all SFNs, $ZnFe_2O_4$, $CoFe_2O_4$, $NiFe_2O_4$, and $MnFe_2O_4$ have been more popularly investigated and used as prospective anode materials for LIB applications. To explain this from an electrochemical mechanism perspective, one of the main things making them a perfect substitute for traditional anode materials is the coexistence of several oxidation states, which is favourable for rapid redox reactions, leading to enhancements in the efficiency and quality of both energy storage and conversion systems. More interestingly, benefiting from varying the transition metal element components in the electrode structure, the energy density and working voltage can be tuned.[81] For example, a great theoretical capacity of over 1000 mA h g^{-1} was reported in LIBs using a $ZnFe_2O_4$-based anode material owing to its Li^+ storability, not only through the redox reaction between Zn^{2+} and Fe^{3+} (eqn (1)–(3)) but also during the alloying reaction between Zn and Li to form a $Li_{4.4}Sn$ alloy during the lithium insertion and extraction process (eqn (4)) (Fig. 4b)[82–84]. Some SFNs based on Mn, Ni, Co, and Cu, although they do not possess free interstitial sites to host Li^+, like in the graphite structure, and do not form alloys with lithium like Sn and Zn, instead only react reversibly with lithium *via* conversion reactions, similarly to Fe; however, their capacities still reach higher values compared with normal TMOs.

$$ZnFe_2O_4 + 8Li^+ + 8e^- \rightarrow Zn + 2Fe + 4Li_2O \quad (1)$$

$$2Fe + 2Li_2O \rightarrow 2FeO + 4Li^+ + 4e^- \quad (2)$$

$$Zn + Li_2O \rightarrow ZnO + 2Li^+ + 2e^- \quad (3)$$

$$Zn + 4.4Li^+ + 4.4e^- \rightarrow Li_{4.4}Zn \quad (4)$$

More specifically, Guo *et al.*[85] pointed out the deep origins of the enhancement in the electrochemical performance of $ZnFe_2O_4$ electrodes *via* studies of the discharge mechanism, structural dynamics, active sites, and the roles of Li, O^{2-}, Fe^{3+}, and Zn^{2+} in the early stage of the lithiation process, from $ZnFe_2O_4$ up to $Li_2ZnFe_2O_4$. It was observed that the intercalation of Li^+ will focus on octahedral 16c sites if x gradually increases to 1, and the displacement of Zn^{2+} sites from tetrahedral 8a sites to 16c sites started at $x = 0.25$. High stability was reached when $x = 1$ and stability decreased for $1 < x \leq 2$ (Fig. 4c). Other advantages of SFNs are that they possess the inherent characteristics of having natural abundance, being environmental benign, and showing a widened potential window. The existence of multiple metals in one crystal lattice and the tight bonds between them induce higher electrical conductivity because of the lower activation energy of electron transfer between cations compared with a single-metal oxide structure.[84,86]

Unfortunately, like most other TMOs, none of them can overcome the important obstacles of poor electron conductivity, high interparticle resistance, rapid capacity fading, and structural instability due to huge volume expansion and the self-aggregation of monodispersed NPs during the charge/discharge process. For instance, in 2003, Alcántara *et al.*[87] reported a $NiFe_2O_4$-based electrode as an anode material for use in LIBs for the first time; it delivered an initial reversible capacity of about 900 mA h g^{-1} but, nevertheless, the cycling performance was rather low, with a capacity of approximately 400 mA h g^{-1} after 10 cycles. Four years later, in order to enhance the electrochemical performance of $NiFe_2O_4$ materials, a new sol–gel synthetic method for obtaining $NiFe_2O_4$ NPs from a citrate precursor was proposed to create more uniform and smaller $NiFe_2O_4$ NPs. As a result, the maintained capacity value of this $NiFe_2O_4$-based electrode was increased up to 600 mA h g^{-1} after 80 cycles.[88] More particularly, progress involving heterostructured designs based on $NiFe_2O_4$ NPs to improve specific capacities, cycle life, and rate capabilities has been recorded *via* the uniform distribution of $NiFe_2O_4$ NPs on the surface of CNTs[89] and/or graphene,[81] and even *via* core–shell architecture using TiO_2 (ref. 90) and polypyrrole (Ppy).[91] In another instance, $CoFe_2O_4$ thin films with an average size of 80 nm were reported to possess an initial irreversible capacity of 1280 mA h g^{-1} in LIBs, which is three times higher than the theoretical specific capacity of graphite.[92] However, after 20 cycles, the capacity of these thin films gradually decreased and was maintained at about 610 mA h g^{-1}. Through varying the

morphology from thin films to three-dimensional nanofibers to better accommodate volume changes and maintain the structural integrity, the initial capacity of a $CoFe_2O_4$ material achieved a better level of 1888 mA h g^{-1} and maintained a reversible capacity as high as 942 mA h g^{-1} after 80 cycles.[93] In fact, it was demonstrated that the use of a one-dimensional mesoporous structure of $CoFe_2O_4$ nanofibers, possessing a high specific surface, large additional space and high crystallinity, could accommodate well the issue of volume expansion, facilitate a fast Li^+ diffusion pathway and effective electron transfer, and create good contact between the electrolyte and electrode and more active sites. A similar trend was also found for $ZnFe_2O_4$ anode materials. NuLi *et al.*[94] pointed that upon using thin films with a size range of less than 100 nm, a $ZnFe_2O_4$ anode material obtained *via* a reactive pulsed laser deposition method provided an initial reversible capacity of 556 mA h g^{-1}, and just 78% of this capacity can be maintained over 100 cycles; meanwhile, when using $ZnFe_2O_4$ nanofibers with a better-controlled diameter in the range from 200 to 300 nm and a uniform distribution of pores on the surface of the $ZnFe_2O_4$ nanofibers owing to an effective electrospinning and annealing process, a higher initial discharge capacity of 1212 mA h g^{-1} was exhibited, and a promising reversible capacity of 753 mA h g^{-1} was still retained after 200 cycles at a high current density of 5 A g^{-1}.[86] Clearly, *via* changes in the morphological characteristics, hybrid engineering, and the suitable selection of electrode materials, the electrochemical performance of SFN-based electrodes for use in LIBs can be enhanced remarkably. This is why there has been a sharp rise in the number of studies based on binary metal oxides-SFNs with novel heterostructured designs for LIB applications. Of course, to further clarify these aspects, the content discussed below will give the reader a more detailed and in-depth view.

3.1.2. Spinel ferrites (AFe_2O_4) for environmental applications. For environmental prospects, the two important technology fields that have attracted the most attention are (i) the treatment of toxic gases, organic compounds, and heavy metals *via* adsorption and photocatalytic degradation methods; and (ii) the sensing and monitoring of toxic pollutants in the environment.

In the treatment field, some traditional strategies, such as coagulation, filtration and ion exchange *via* membranes, advanced oxidation process, electrolysis, and non-magnetic NP-based adsorption techniques, have been applied to resolve pollution problems for a long time. However, they, in fact, are limited by the incomplete removal of pollutants, adsorbent recovery difficulties, and high production costs. NPs have been investigated and fabricated for combination with these techniques, aimed at enhancing removal efficiencies. The positive effects when NPs are applied to these approaches cannot be denied, but their toxicity has become another large issue. NPs may be new secondary pollutants, hazardous to public health and the environment. Meanwhile, SFNs, like semiconductors, have many extraordinary physicochemical properties in terms of optical, electrical, and catalytic activities that can provide promise for adsorption- and photocatalytic-based pollutant removal. As mentioned above, SFNs possess high adsorption capacities due to the large number of reactive sites and metal ions that can directly interact with contaminants to promote removal efficiencies. More interestingly, compared with other strategies applied in the adsorption field, the utilization of non-toxic SFNs can help the catalyst recycling process to become easier, because they can be recovered *via* an external magnetic field owing to them being magnetically separable. Of course, SFNs can support the separation of used adsorbents to some degree, but they are still not practical enough to meet all the demands of industrial applications due to production being only on a small-scale. Besides, unfortunately from a photocatalytic aspect, the rapid recombination of photogenerated e^-/h^+ pairs can also lead to critical limitations. Thus, it is imperative to maximize the potential photocatalytic activity further and take advantage of other light sources in these processes. Notably, a better approach is to use SFNs as an important sensitizer for wide-bandgap semiconductors or to combine SFNs with other functional materials to increase the survival time of e^-/h^+ pairs. This has become an inexorable trend, in pursuit of lower cost, easier fabrication techniques, and higher efficiency.

In the sensing and monitoring areas, the development of new sensors based on SFNs to replace old sensor types with large production costs, high operating temperatures, short lifetimes, and difficult fabrication techniques has attracted a lot of attention, with the aim of detecting toxic pollutants at low concentrations (few ppm) in an early fashion with fast response times *via* both oxidizing and reducing gas, which old sensors cannot do.[8,95] A rise in the number of reports on the use of $MgFe_2O_4$, $ZnFe_2O_4$, $CuFe_2O_4$, $NiFe_2O_4$, and $CoFe_2O_4$ for the detection of CH_4, H_2S, Cl_2, liquified petroleum gas (LPG), ethanol gas, and even heavy metals can be found in the literature.[96,97] Using SFNs with semiconducting behavior results in outstanding chemical reactivity owing to the substitution of cations, the high aspect ratio, and the large number of reactive surface sites. However, to be frank, pure SFNs still face serious challenges; furthermore, the sensing efficiency depends remarkably on microstructural properties, such as morphology, size, and crystal structure. Recent reports have revealed that the modification and redesign of spinel ferrite structures with suitable support materials is considered to be a potential approach to further improve the sensitivity, selectivity, response time, and long-term stability (Fig. 5).

3.1.3. Spinel ferrites (AFe_2O_4) for biomedical applications. The most important characteristics of SFNs that have attracted researchers for biomedical purposes are their low inherent toxicity, ease of fabrication, tunable size, and shape, great superparamagnetic behavior (high magnetocrystalline anisotropy and high coercivity), and high M_s values, without any loss of the inherent advantages of nanomaterials.[1] With such characteristics, SFNs can be effectively controlled *via* using an external magnetic field; however, they do not show any agglomeration after the removal of the magnetic field, creating a clear advantage over other NPs like silica, TMOs, and carbonaceous materials. Besides, their unique physiochemical properties, like a high surface area to volume ratio, stable mechanical hardness, and flexible surface functionalization,

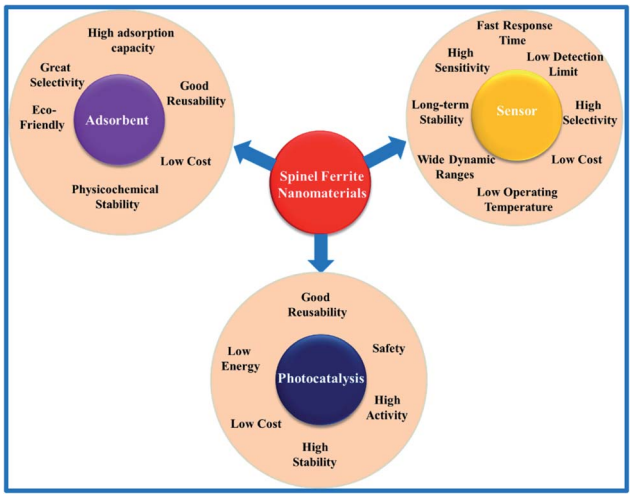

Fig. 5 The environmental monitoring applications of spinel ferrite nanomaterials.

make SFNs more particularly attractive. Several groups have investigated the use of SFNs for various biomedical applications, such as targeted drug delivery, magnetic hyperthermia, magnetic resonance imaging, and magnetic separation.[1,9,98,99] In all cases, however, it is important to note that bare SFNs face large challenges regarding their poor magnetic properties at small sizes and under physiological conditions. Moreover, issues of biocompatibility and toxicity are serious limitations to the development of SFNs because the presence of iron atoms in a structure can create interactions with hemoglobin, leading to undesirable side effects. As a result, the modification of bare SFNs *via* the formation of SFN-based hybrid designs has emerged so far as a crucial step in order to improve biocompatibility and safety, reduce side effects, prevent aggregation, and impart multifunctional abilities. A promising hybrid design will show strong magnetization at a small size and low concentration, and under physiological conditions. In this article, a thorough review of current development aspects relating to SFN-based hybrid designs for use in the biomedical field and future prospects will be made in detail below.

3.2. Hybrid designs between spinel ferrites (AFe_2O_4) and carbonaceous nanomaterials

3.2.1. Carbon-coated spinel ferrites (AFe_2O_4). Among the many varied strategies to circumvent LIB issues, one of the most promising ways is to disperse and construct hybrid carbonaceous matrix designs possessing high electronic/ionic conductivity and excellent stability (*e.g.*, the use of carbon coatings, CNTs, CNFs, graphene, and rGO). Coating carbon onto the surfaces of electrode materials like TMOs to overcome challenges relating to LIB electrochemical performance deriving from low conductivity, huge volume changes, and aggregation has been studied for a long time. Of course, SFNs are not removed from that development trend. The most typical evidence is contained in a series of reports, and recent efforts have also investigated and evaluated the efficiency and attraction of this method. Normally, a carbon-coating approach is chosen for SFNs with many varied shapes, for example, with 0D morphology (NPs and nanospheres) and 1D morphology (nanotubes, nanowires, nanorods, and nanofibers), corresponding to core/shell and/or yolk/shell designs (Fig. 6a and b). According to research, a nanostructured milled $MgFe_2O_4$ sample with a grain size of 19 nm was employed for the first time as an active electrode *vs.* lithium metal, where it delivered an initial discharge capacity of around 850 mA h g^{-1}.[100] However, the capacity was unstable and tended to gradually decline during the charge/discharge process during subsequent cycling. *Via* using pyrrole as a conductive carbon source to modify the surface of a $MgFe_2O_4$ material through a decomposition approach at 550 °C, a carbon-coated $MgFe_2O_4$ (MFO/C) material with a smaller grain size showed improvements in electrical conductivity and shortened Li^+ and electron transport paths; also, the presence of a MgO phase as a dispersant during the charge/discharge process aimed to prevent Fe and its oxide from aggregating and to accommodate volume expansion, which could remarkably improve the electrochemical performance. The synthetic anode material exhibited a reversible capacity of 744.0 mA h g^{-1} after 160 cycles at 100 mA g^{-1}, which was higher than both pure $MgFe_2O_4$ and a carbon-coated Fe_3O_4 (FO/C) electrode that was prepared and tested under the same conditions (476.7 mA h g^{-1} after 95 cycles) (Fig. 6c and d).[101] Similarly, using a one-dimensional $MgFe_2O_4$ material, Luo *et al.*[102] demonstrated significant electrochemical efficiency improvements in terms of cycling stability and rate capability using uniform 6 nm-thick carbon shells on $MgFe_2O_4$ nanofibers. Electrochemical results showed that, benefiting from its appropriate carbon coating, a reversible capacity of 743 mA h g^{-1} after 200 cycles was obtained and a stable capacity of 451 mA h g^{-1} at 2 A g^{-1} was maintained. The coating carbon approach was widely applied to almost all other SFNs, not just $MgFe_2O_4$ materials. Indeed, carbon-coated $ZnFe_2O_4$ and $CoFe_2O_4$ NPs,[103,104] $MnFe_2O_4$ nanospheres,[105] $ZnFe_2O_4$ nanorods,[106] $ZnFe_2O_4$ nanofibers,[107] and even 3D-$ZnFe_2O_4$ nanoflakes[108] and $NiFe_2O_4$ mesoporous hollow spheres[109] were successfully fabricated and presented excellent electrochemical storage performance in terms of reversible capacities, cycle lives, and rate capabilities compared with pure SFNs. Herein, to explain the positive changes in electrochemical performance, it is assumed that the unique carbon-coated electrode structure provides a higher surface area along with numerous reactive sites and short transport pathways for both electrons and Li^+. Indeed, the uniform carbon shells not only act as a beneficial buffer to protect metal elements in the spinel ferrite structure and to protect oxides from self-aggregation and pulverization arising from large surface interaction forces, subsequent conversion reactions in electrochemical processes, and huge volume expansion, but they also ensure good intrinsic electronic conductivity in the synthetic electrode. Furthermore, the synergistic effect of the core/shell or yolk/shell morphology could improve the contact between the electrode and electrolyte, while increasing to a sufficient degree the electrical connections between the current collector and active material. Also, direct interactions between the inner active material and

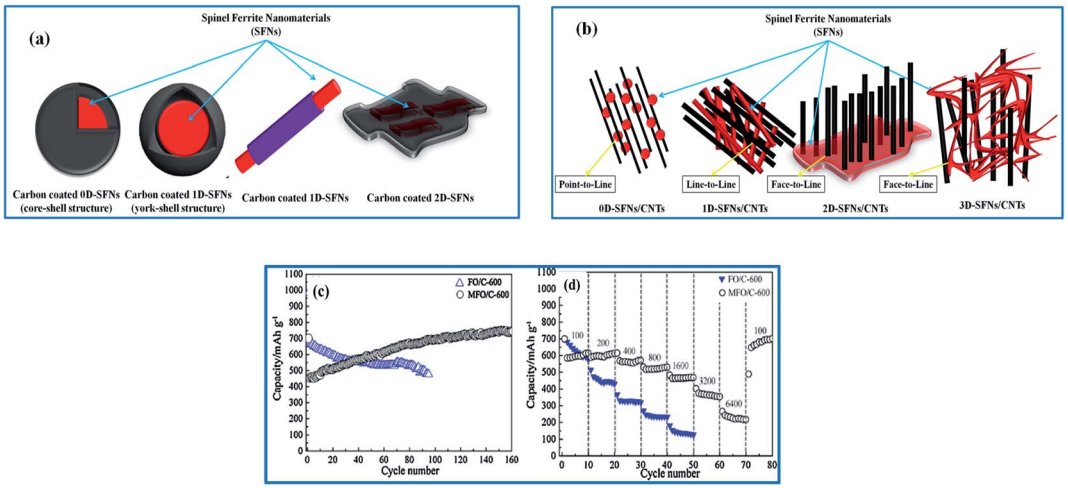

Fig. 6 The various hybrid designs of (a) carbon-coated SFNs and (b) CNTs/SFNs. (c and d) The cycling performances at a current density of 100 mA g^{-1} and rate capabilities of MFO/C and FO/C (reprinted with permission from ref. 101; copyright: 2013, Elsevier Ltd).

electrolyte are avoided, leading to decreased interfacial resistance and charge-transfer resistance (R_{ct}).

Similarly, in the environmental case, a carbon-coating approach has been chosen to modify and further develop SFNs to more effectively enhance the removal efficiencies of contaminants and reusability. As can be seen, carbonaceous materials are known as typical nanomaterials for adsorption and photocatalysis processes due to their high adsorption capacities, rich surface functionalities, low bandgaps arising from large external surface areas, great mechanical strengths, and chemical and structural stabilities. The morphology and size of a catalyst material can decide its catalytic performance. The stable support of a carbon coating on SFN surfaces inhibits the self-aggregation of SFNs effectively without the detachment of NPs from the substrate matrix. Also, it provides adsorptive domains for the enrichment of the exposure area between pollutants and catalytic sites, and it creates abundant transport pathways for reactive molecules, leading to both adsorption and photocatalytic performance enhancements. More importantly, as described, carbon-coated SFNs can be easily recovered and reused *via* using an external magnetic field to separate them from the reaction mixture. T. Zeng and co-workers demonstrated that *via* constructing a unique mesoporous hybrid structure between N-doped carbon microspheres (NC) and $CoFe_2O_4$ nanocrystals, the catalytic efficiency and reusability could be improved; namely, 100% methylene blue (MB) removal was achieved in 20 min during the first cycle and 95% was achieved even after 4 cycles.[110] Both NC and $CoFe_2O_4$ NPs had roles as active sites, directly supporting the oxidation reactions of MB molecules in the presence of peroxymonosulfate (PMS); together, they created a large surface area of 334.39 m^2 g^{-1}, with a total pore volume of approximately 0.56 cm^3 g^{-1}. Porous coating layers with high electronic conductivity supported the promotion of electron transfer between components, and regenerated catalytic sites, therefore showing interesting synergetic effects. Moreover, the formation of a hollow structure facilitated an increase in the positive contact between both internal and external active sites; a possible mechanism explaining the high catalytic performance is proposed in Fig. 7b. The initial adsorption of MB on the surface of the catalyst occurred *via* π–π interactions between the graphitic-like structure of NC and the aromatic rings of MB, then the active sites of Co^{2+} and Fe^{3+} on the $CoFe_2O_4$ surface activated PMS *via* $HSO_5^{\bullet-}$ group catalysis to create more radicals, such as $SO_4^{\bullet-}$, $SO_5^{\bullet-}$, and $OH^{\bullet}$, which directly degraded MB in solution. Similarly, reports by Zhang[111] and Song[112] also mentioned the utilization of $CoFe_2O_4$ for the construction of core–shell designs with CNTs and rGO, respectively. Most of the obtained results showed the uniform formation of an outer carbon shell on $CoFe_2O_4$ NPs; as a result, $CoFe_2O_4$–rGO offered a great absorption capacity of about 263 mg g^{-1} at 298 K for methyl orange and, more specially, it showed a specific saturation magnetization (M_s) value of 32.8 emu g^{-1}, which may support its separation after adsorption more easily. In addition to $CoFe_2O_4$, $ZnFe_2O_4$ (ref. 113) and $CuFe_2O_4$ were proposed and studied as reusable magnetic catalysts in combination with carbonaceous materials with the aim of toxic pollutant removal from the environment. Although there are many positive signs about its ability to remove toxic pollutants, this hybrid design has not received much attention to date for sensor applications for the early detection of hazardous substances in the environment. This is clearly shown by the number of related reports being limited. This direction could have promise and attract scientists in the future but, of course, more research and detailed reports are needed to assess the application potential properly.

In fact, up to now, none of the introduced hybrid designs based on carbon-coated AFe_2O_4 have been approved for biomedical applications, especially hyperthermia, MRI, magnetic separation, drug delivery, biosensing, and magnetoreception, except for Gorgizadeh's report.[114] In this, a $NiFe_2O_4$/C nanocomposite was introduced, fabricated successfully, and used as an effective photoabsorbing agent in a promising photothermal therapy approach towards the C540 (B16/F10) cell line and a melanoma cancer mouse model. Due to the high

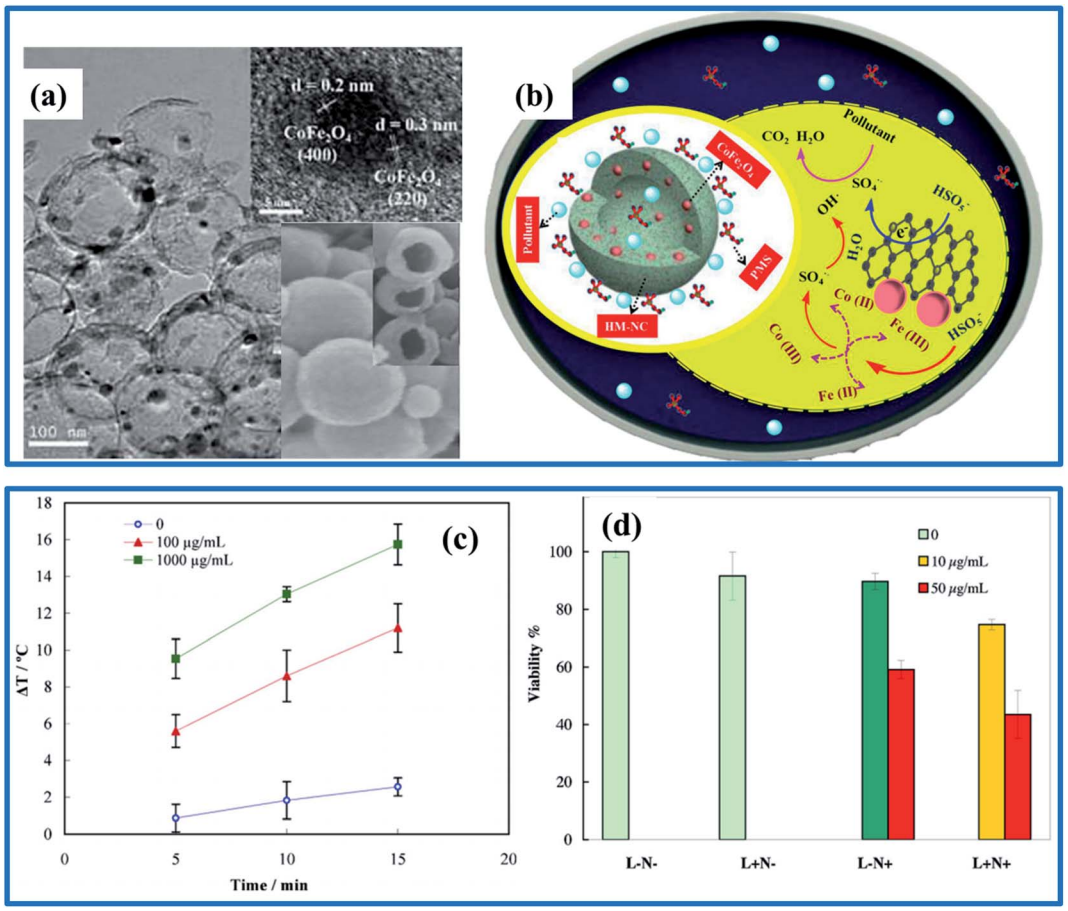

Fig. 7 (a and b) TEM images of HM-NC/$CoFe_2O_4$ and the proposed mechanism for pollutant degradation. (c) The temperature increase of $NiFe_2O_4$/C at concentrations of 100 and 1000 μg mL^{-1}, and that of a control sample upon exposure to an 808 nm diode laser at 1.0 W cm^{-2} over 15 min. (d) The C540 (B16/F10) percentage cell viabilities after exposure to irradiation for 10 min from a diode laser following 4 h of incubation with two concentrations of $NiFe_2O_4$/C (1 or 50 μg mL^{-1}) (L^+N^+), after irradiation for 10 min without $NiFe_2O_4$/C (L^+N^-), after exposure to $NiFe_2O_4$/C (10 or 0 μg mL^{-1}) without irradiation (L^-N^+), and without laser irradiation or $NiFe_2O_4$/C (L^-N^-) (reprinted with permission from ref. 110 and 114; copyright: 2017 and 2018, Elsevier Ltd, respectively).

thermal and electrical conductivities and the effective conversion of light to heat by the carbon coating, a more rapid increase in temperature was facilitated during photothermal therapy. Besides, this hybrid design helped to create a more specific and definitive treatment process, leading to a reduction in side effects and inducing lesser toxicity in normal tissues (Fig. 7c and d). Interestingly, using the hybrid design of a carbon coating and SFN is very promising for cancer therapy; however, the main problems resulting in the limited biomedical applications are probably owing to potential toxicological implications arising from short- and long-term exposure, and low loading capacities and poor dispersibilities under physiological conditions. Furthermore, as can be seen, instead of using a carbon coating, a number of reports have found success when using other coatings, like polymers (CS, polyethylene, and phospholipids)[115–117] or even silica materials. With a polymer coating, the control of SFN particle size, shape, quality, dispersion, and hemocompatibility become probably better because of the unique multifunctional properties arising from the large diversity of functional groups within the polymer structure. This coating layer also can protect the surfaces of SFNs from proteins, cell adsorption, and tissue penetration, thus increasing the particle circulation time for *in vivo* applications.

3.2.2. Spinel ferrite (AFe_2O_4)/carbon nanotubes and carbon fibers. From another point of view, random self-aggregation phenomena between SFNs and carbonaceous nanomaterials with 1D morphology, such as CNTs and carbon nanofibers (CNFs), have been further studied in recent decades. Noticeably, it is stressed that the decoration of SFNs on the surface of CNTs and CNFs is similar to carbon-coated SFNs, shortening the electron/ion path lengths and preventing active materials from aggregation and pulverization during repeated cycling. However, with the presence of a conductive structural framework (CNTs/CNFs), the contact between these active materials becomes point-to-line, line-to-line, or face-to-line, instead of point-to-point as in carbon-coated SFN designs (Fig. 6b). Also, the inherent flexibility, high surface to volume ratio, and better strain relaxation of 1D NMs, as reported above, may result in continuous electron transfer efficiency enhancement, the

accommodation of the influence of huge volume changes, and the growth inhibition of SFNs during the charge/discharge process. Very interestingly, the interconnection and direct growth of SFNs on CNTs/CNFs can help to create stable structures possessing large surface areas with the existence of a large amount of micro/mesopores.[118,119] This indicates the important role played in facilitating effective contact between the electrode material and electrolyte, as well as forming a lot of void space to accommodate volume expansion, stress, and strain generated during the charge/discharge process. Namely, in 2013, Fu *et al.*[120] reported a facile anode material fabrication method for LIBs from $CoFe_2O_4$ and CNTs *via* a calcining process involving the precursors. *Via* the formation of strongly coupling oxygen bridges (metal–O–C) between the CNTs and $CoFe_2O_4$ NPs, R_{ct} was reduced approximately 2-fold; meanwhile, the value of interfacial resistance between the SEI layer and electrolyte was maintained both before and after Li ion insertion, not only demonstrating the better kinetics of the process and the great state stability of the SEI film, but also the high specific capacity retention. In a similar report, $CoFe_2O_4$ NPs were utilized in combination with CNFs with the aim of helping to form a self-organized architecture as a conversion anode without using any other templates or additives.[121] This report also evaluated the role of the intimate interconnections between active materials in the anode electrode based on the formed synergistic effects and the supported electrochemical performance. Owing to these synergistic effects, the synthetic anode delivered a high specific capacity of 705 mA h g^{-1} after 250 cycles, which was higher than that of a bare $CoFe_2O_4$ electrode (914 mA h g^{-1} in the first cycle and only 80 mA h g^{-1} after 50 cycles).[122] Most recently, *via* changing the fabrication method through solvothermal and calcination processes, a coralline structure of $CoFe_2O_4$ and CNTs was created.[123] It offered an outstanding reversible capacity value of 747.5 mA h g^{-1} after 220 cycles at 200 mA g^{-1}, corresponding to a coulombic efficiency (CE) of 74%, which was higher than the value of 64.4% obtained from pure $CoFe_2O_4$ NPs. Apart from $CoFe_2O_4$, $CuFe_2O_4$, $MnFe_2O_4$, $MgFe_2O_4$, and $NiFe_2O_4$ were also investigated and fabricated with hybrid architectures based on CNTs and CNFs (Table 1). It can be seen that in most of the mentioned hybrid designs, significant enhancements in the capacity and cycle life are clear. In particular, the capacity retention always reached a high level compared with the pure SFN when tested under the same conditions. These results once again demonstrate the successful hybridization between SFNs and 1D carbonaceous materials and highlight the important role of 1D carbonaceous materials for obtaining promising electrodes with many unique properties for LIB use.

In the literature, some investigations related to the combination of 1D carbonaceous nanomaterials and SFNs for environmental purification applications have been discussed in detail. Gabal *et al.*[12] prepared MWCNT/$CoFe_2O_4$ *via* a gelatin auto-combustion method and used it as an efficient adsorbent for acid red (AR) dye. Luan *et al.*[127] used $CuFe_2O_4$ NPs incorporated into CNTs as an effective composite membrane for arsenite (As) filtration. Oyetade *et al.*[128] evaluated the adsorption abilities of MWCNTs/$CoFe_2O_4$ for rhodamine B (RhB), as well as the effects of the MWCNT content on enhancing the adsorption capacity. Li *et al.*[129] demonstrated the efficient removal abilities and reusability of Ppy/CNTs–$CoFe_2O_4$ nanocomposites toward MB, methyl orange (MO), and acid fuchsin (AF). According to research by Bahgat and Zhu, $NiFe_2O_4$ NPs could be homogenously decorated on MWCNTs to remove toluidine blue and Congo red (CR) *via* adsorption and photocatalytic decolorization processes. Some important factors that can affect these processes, including pollutant concentration, temperature, and exposure time, were tested.[130,131] Overall, these hybrid designs showed high adsorption capabilities, great selectivity, good structural and chemical stability, and, more interestingly, high magnetic responses, which helped improve reusability. In this case, the remarkable increase in adsorption quality is due to the inherently powerful adsorption abilities of 1D carbon materials, along with the presence of many high energy adsorption sites, such as defects and functional groups. Besides, the presence of an open porous structure, created from random combinations between components, and a large surface area is considered to be another key factor explaining this achievement. Also, SFNs play an important role, acting as magnetic adsorbents assisting the aim of reusability. In recent reports, to optimize the performance of hybrid designs containing 1D carbon materials and SFNs as superior absorbents, a method of SFN and 1D CNT surface chemical modification is essential to avoid agglomeration on surfaces and weak interactions between components (Fig. 8a and b). Zhou *et al.*[132] illustrated a promising approach to change the surface of $CoFe_2O_4$ NPs using the amino functional groups of CS. The obtained hybrid material had maximum

Table 1 A comparison of LIB electrodes based on hybrid designs containing SFNs and 1D carbonaceous nanomaterials

Electrode material	Current density (mA g^{-1})	Discharge capacity (mA h g^{-1})	Capacity retention (mA h g^{-1})/cycles	Coulombic efficiency (%)	Ref.
$MgFe_2O_4$ NPs/CNFs	100	1100	575/20	60.52	124
$CuFe_2O_4$ nanowires/CNTs	200	2500	853/50	87	125
$MnFe_2O_4$ NPs/MWCNTs	0.1C	1356	600/350	57.4	119
$MnFe_2O_4$ NPs	0.1C	1405	295/80	70.1	
$NiFe_2O_4$ NPs/CNTs	100	1030	624.6/100	76.4	89
$NiFe_2O_4$ NPs	100	1101	200/100	74.8	
$NiFe_2O_4$ NPs/MWCNTs	372	1305	871/25	79	126
$NiFe_2O_4$ NPs	372	1150	828/25	71	

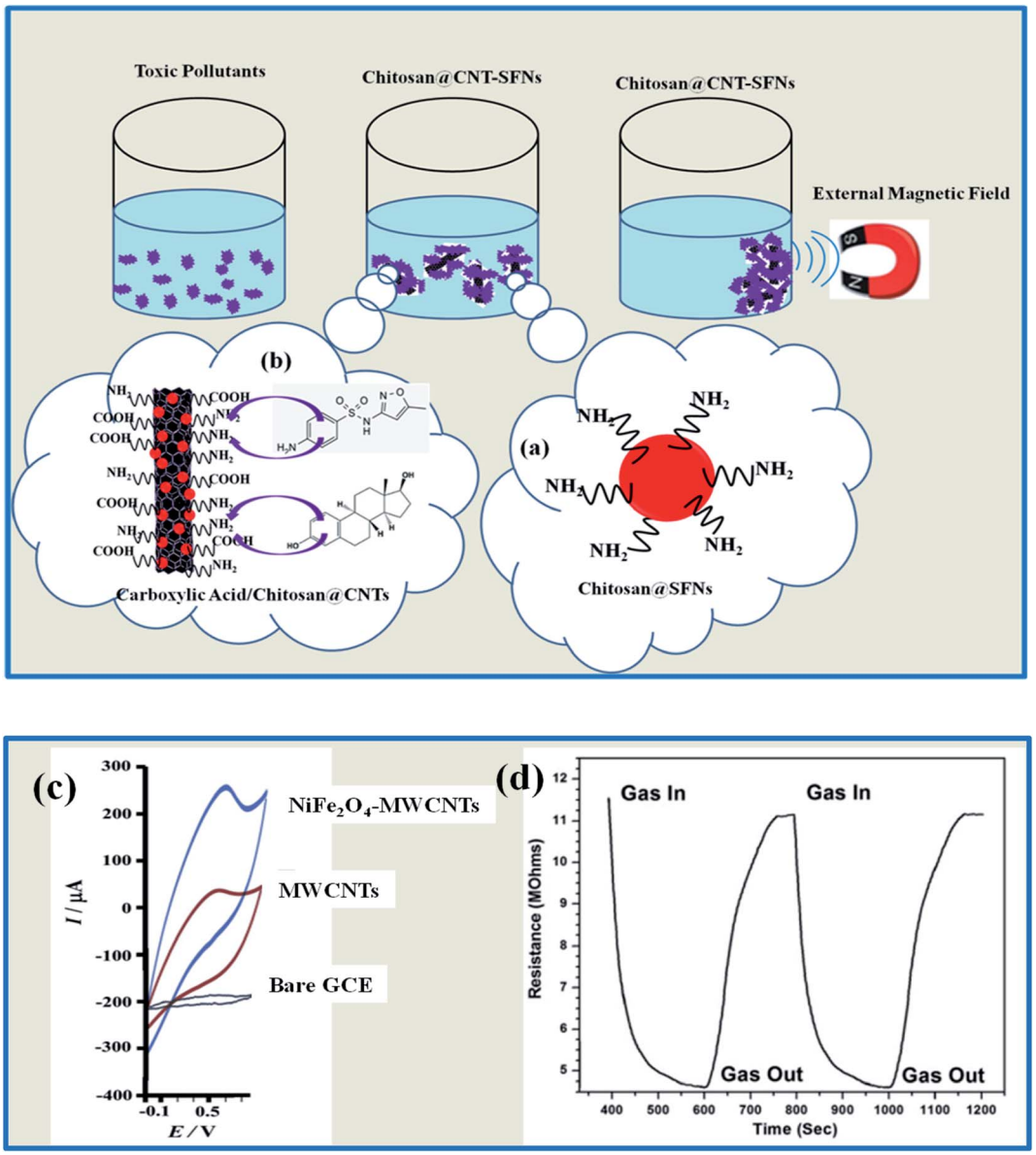

Fig. 8 (a and b) The surface modifications of SFNs and CNTs for pollutant removal applications. (c) The voltammetric responses of various sensor electrodes to sotalol. (d) The response of a $NiFe_2O_4$–MWCNT thin film towards 100 ppm H_2S at 300 °C (reprinted with permission from ref. 136 and 138; copyright: 2013 and 2014, Elsevier Ltd, respectively).

adsorption capacities of 42.48 and 140.1 mg g^{-1} for tetrabromobisphenol A and Pb(II), respectively, higher than when using $CoFe_2O_4$ without amino groups. These amino functional groups reacted with the target pollutants through strong chemical forces instead of a normal physical adsorption process. Furthermore, the $CoFe_2O_4$–NH_2 NPs showed ferromagnetic behavior, with coercivity (H_c) of 285 Oe, which was higher than that of bare $CoFe_2O_4$ NPs. In another report, Wang *et al.*[133] changed the surface of CNTs using carboxylic and amino groups (CNTs–C and CNTs–N, respectively). As a result, they exhibited significant adsorption potential (ε) enhancement towards pollutants owing to the stronger interactions between them and promised to be a potential adsorbent for organic pollutants (Fig. 8b). In terms of photocatalytic activity, the enhanced photocatalytic efficiency stems from synergistic contributions related to the good light absorption abilities of the 1D carbonaceous photosensitizer, the strong interactions, the efficient electron transportation between components because of the open electronically conductive skeletons, and the diversity of oxidizing species (h^+, e^-, $^{\bullet}OH$, and $O^{2\bullet-}$ radicals) arising from the high photocatalytic activity of SFNs. More importantly, the more efficient charge carrier separation of e^-/h^+ pairs in this design is also another factor explaining the high photocatalytic degradation.[131,134,135] Unlike in the above cases, to validate the possibility of the utilization of this design for sensor applications, Ensafi *et al.*[136] carried out an interesting study involving the combination of $NiFe_2O_4$ NPs and MWCNTs *via* a simple sol–gel synthetic method. The synthetic composite

was able to act as a convenient and useful electrochemical sensor to detect sotalol with a wide linear dynamic range of 0.5–1000 μmol L^{-1} and a low detection limit of 0.09 μmol L^{-1}. The great results were verified as being due to the strong adsorption of targets on the surface of the modified electrode because of the huge electrode surface areas (six times greater than that of a glassy carbon electrode (GCE)). Also, the useful electronic properties, owing to strong synergic effects on the target redox process, and high levels of electron transfer contributed significantly to these results.[137] In addition, these reasons also caused an increase in conductance and meanwhile reduced the electrical resistance, leading to an enhanced gas sensor response and sensitivity. In comparison with a bare GCE and MWCNTs without modification, the voltammetric response of the $NiFe_2O_4$ NPs–MWCNTs electrode to sotalol involved a rise in sharp peak current, while GCE and MWCNT electrodes had weaker peak currents (Fig. 8c). Similarly, Hajihashemi *et al.*[138] also chose $NiFe_2O_4$ NP–MWCNT composites to detect the existence of H_2S. The obtained results showed a better response than both pure $NiFe_2O_4$ and MWCNT-based sensors. At a concentration of 100 ppm, this electrode could detect H_2S within 110 s *via* a rapid change in resistance from 11.5 to 4.5 MΩ (Fig. 8d); meanwhile, the pure $NiFe_2O_4$ electrode detected only at a higher detection limit of 200 ppm, and the gas response was only about 30% (ref. 139) (Table 2).

It seems that 1D carbonaceous materials have gained more attention for almost all types of bio-application, including biosensors,[144,145] drug delivery,[146,147] imaging, and therapy.[148,149] As mentioned above, $CoFe_2O_4$ and $ZnFe_2O_4$ NPs have been widely studied for sensor applications, mainly due to their self-interaction properties and versatile responses to an external magnetic field. MWCNTs show high adsorption because of their large surface area, high electrical conductivity, and structural and chemical stability. In this case, the synergistic effects stemming from incorporating these sets of characteristics once again can be taken advantage of in an optimal way *via* combining the two components together through the uniform distribution of SFNs on MWCNTs; this arrangement can then be used to determine the existence of ofloxacin, metoclopramide (MCP), and indomethacin (IND) in pharmaceutical and biological samples.[144,145] The results exhibited that $ZnFe_2O_4$/MWCNTs showed better electron transfer kinetics, with a low R_{ct} value of 42 Ω and a large electroactive surface area of 0.10 cm^2, 3 times higher than a carbon-paste electrode (CPE). As a result, the determination of MCP in human blood serum, pharmaceutical, and urine samples *via* DPV showed higher sensitivity and selectivity (Table 3). Besides, the synthetic $CoFe_2O_4$–MWCNT adsorbent showed a wide detection range of 100–750 ng mL^{-1} with a detection limit of 23 ng mL^{-1}.

Also, $ZnFe_2O_4$ and $CoFe_2O_4$ were assessed as showing high potential for use in drug delivery systems; their composites with MWCNTs possessed high M_s values of 132/49 emu g^{-1}, M_r values of 12/37 emu g^{-1}, and H_c values of 48/35 Oe, respectively[147]. More specifically, Fan *et al.*[146] fabricated a triple composite consisting of SiO_2, $CoFe_2O_4$ NPs, and MWCNTs and used it for anti-cancer drug delivery. It needs to be noted that, like carbon-coated designs, in essence, the poor dispersion, low loading capacity, and poor biocompatibility of CNTs and MWCNTs lead to limitations in their biological application. To address these issues, a coating layer of mesoporous silica ($mSiO_2$) was formed on the surface of $CoFe_2O_4$/MWCNTs without the loss of superparamagnetic properties. Then, the drug doxorubicin (DOX) was loaded successfully *via* numerous mesoporous nanocarriers and hydrogen bonds between the carboxyl groups of the drug molecules and the SiO_2 surface with the aim of targeted cancer therapy. The synthetic carrier showed excellent drug release abilities within 48 h according to a diffusion-controlled mechanism under pH control and following the degradation of the weak hydrogen bonds. Also, this hybrid design demonstrated great biocompatibility, with cytotoxicity remaining at a low level even at a high concentration.

3.2.3. Spinel ferrite (AFe_2O_4)/graphene and graphene oxide. Like the mentioned strategies, hybrid designs involving SFNs and graphene have also been explored to overcome obstacles relating to LIB applications and to obtain improved electrochemical properties. In recent reports, most SFNs have been decorated on the surface of the graphene substrate in the form of NPs. This is an inevitable trend, owing to the availability of simple and fast NP fabrication methods, while the obtained efficiency is stable and promising compared with other forms of fabrication. The fabrication engineering used for this hybrid design may be pure mechanical blending between graphene and pre-prepared SFNs[150] or the direct growth of SFNs atop graphene sheets *via* a co-precipitation reaction,[151–154] an electrostatic spray deposition (ESD) method,[84] or electrophoretic deposition (EPD) techniques[155,156] (Fig. 9) from metal salt precursors. This hybrid design not only ensures a homogeneous distribution of NPs and good interaction between components, aiming to create stable architecture with a higher contact interface area and more lithium insertion/extraction sites, but it

Table 2 A comparison of the performances of different modified electrochemical sensors using the reported voltammetry methods[a]

Technique	Electrode material	Detection limit (μmol L^{-1})	Linear range (μmol L^{-1})	RSD (%)	Ref.
Cyclic voltammetry	Gold microelectrode	3.49	1.1–50	3.6	140
Cyclic voltammetry	$NiFe_2O_4$–MWCNTs/GCE	0.09	0.5–1000	2.3	136
DPV	MWCNTs/CFE	0.9	>100	8.3	141
DPV	$NiFe_2O_4$–MWCNTs/GCE	0.09	0.1–1000	0.9	142
DPV	G/Au/GCE	0.07	0.5–8	—	143

[a] DPV: differential pulse voltammetry; G: graphene; RSD: relative standard deviation.

Table 3 The determination of MCP in human blood serum and urine samples *via* DPV ($n = 4$)[145]

Recovery (%)	RSD (%)	MCP found (μM)	MCP added (μM)	Sample
92.0	2.17	1.84 ± 0.04	2.0	Human blood serum
102.3	0.85	15.35 ± 0.13	15.0	Human blood serum
103.0	1.46	2.06 ± 0.03	2.0	Urine
97.8	0.20	14.67 ± 0.03	15.0	Urine

also avoids self-aggregation, volume changes, and the detachment of active materials. Of course, graphene still plays a major role as an effective stress buffer for SFNs because of its many unique features, such as a large surface area, excellent conductivity, mechanical strength, and chemical stability, and a high theoretical capacity. On the other hand, SFNs help to protect the graphene nanosheets from restacking and agglomeration due to the strong stacking, hydrophobic interactions, and weak van der Waals forces. Indeed, Heidari *et al.*[157] successfully fabricated a sandwich-like nanoarchitecture of $NiFe_2O_4$ NPs, a carbon layer, and a graphene matrix. Owing to the direct hydrothermal growth of $NiFe_2O_4$ NPs on the graphene, the synthetic anode offered great cycling stability, maintaining 1195 mA h g^{-1} after 200 cycles, which was much higher than pure $NiFe_2O_4$ NP-based anodes and hybrid designs involving $NiFe_2O_4$ NPs and CNTs. These positive results were attributed to differences in the unique heteroarchitectures leading to changes in the charge/discharge behavior, with the higher utilization of active material, better structural stability, and faster charge transport. More specifically, to easily construct effective hybrid designs, the optimal proportions of $NiFe_2O_4$ NPs and graphene, and special strategies for the utilization of various binders were investigated by Li *et al.*[158] The report pointed out the synergistic effects of using a carboxymethyl cellulose (CMC) binder combined with a suitable graphene content (100 mg), which provided good storage performance and outstanding battery characteristics. It is assumed that well-designed morphology is one of the most critical strategies for promoting electrochemical performance;

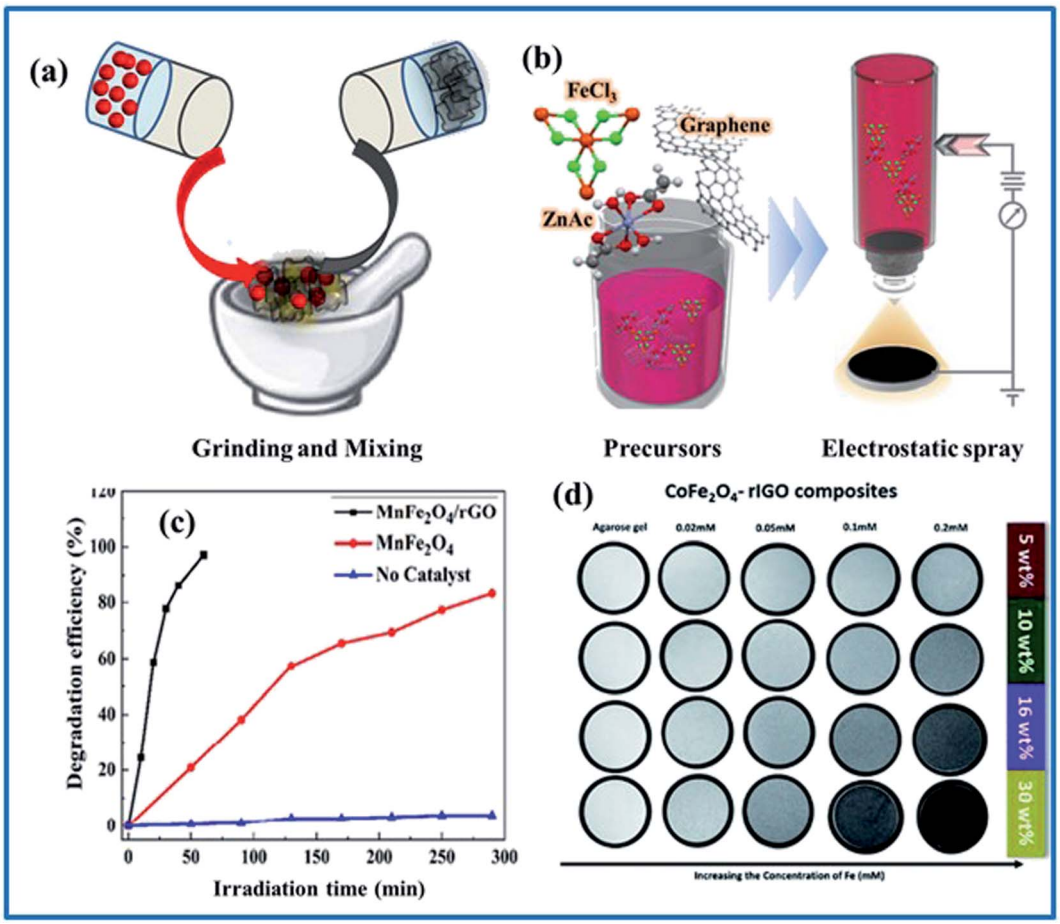

Fig. 9 (a and b) Schematic diagrams of mixing with pre-prepared SFNs and electrospray deposition with synthesized precursors for SFN/graphene fabrication. (c) The photocatalytic MB degradation efficiencies using $MnFe_2O_4$ NPs and $MnFe_2O_4$ NPs–rGO. (d) T_2-Weighted MRI images using $CoFe_2O_4$–rGO composites with different Fe concentrations (reprinted with permission from ref. 84, 161 and 162; copyright: 2019, 2020, Elsevier Ltd, and copyright: 2019, The Royal Society of Chemistry, respectively).

as a result, SFNs with nanosheet morphology were also used for hybridization with rGO for LIB applications.[159,160] However, the number of reports in this research field is still limited, owing to fabrication difficulties and harsh experimental conditions. Luckily, the obtained positive results still exhibit a promising pathway for the development of electrodes in the future.

In the environmental field, the combination of SFNs and graphene is known more widely for both environmental treatment and sensor applications. The expected photodegradation and absorption properties of this hybrid design are still associated with synergistic behaviors between the constituent composite materials, as described in the LIB case. A high surface area and good conductivity enable effective synergistic electronic interactions over the entire surface of an electrode; furthermore, electron transportation between SFNs and graphene can facilitate a high amount of adsorption and many reactive oxygen species. More importantly, this helps to significantly reduce the e^-/h^+ recombination rate, increasing the photodegradation efficiency.[163,164] Yao *et al.*,[165] Mandal *et al.*,[161] and Yamaguchi *et al.*[166] used $MnFe_2O_4$ NPs decorated on rGO and graphene to form unique heterostructures for the effective removal of toxic pollutants from water *via* photodegradation and adsorption. Almost all of the obtained results exhibited the excellent photocatalytic activity and adsorption properties, along with good magnetic properties to increase the reusability and physical durability, with high activities maintained after long-term use. It should be noted that compared with bare $MnFe_2O_4$, this hybrid design had a higher specific surface area of 196 $m^2\ g^{-1}$ and a larger pore volume of 0.367 $cm^3\ g^{-1}$; meanwhile, pure $MnFe_2O_4$ only achieved values of 90.6 $m^2\ g^{-1}$ and 0.31 $cm^3\ g^{-1}$, respectively. The $MnFe_2O_4$-based design also demonstrated high performance with easy recycling and good stability; more importantly, it photodegraded over 97% of MB within 60 min, which was higher than 84% after 290 min achieved using pure $MnFe_2O_4$ (Fig. 9c). In another experiment, *via* optimizing the graphene content in the hybrid design, the magnetic characteristics of the design could be tuned; at 15% graphene, it exhibited not only magnetic properties similar to pure $ZnFe_2O_4$ NPs but also provided much larger physical and chemical interaction areas, separating almost all (99%) dye from solution after a short time of 6 min compared with 96% after 16 min when using pure $ZnFe_2O_4$ NPs.[167]

The development of unique sensors for the fast detection of pollutants has also been studied *via* combinations between SFNs and rGO. However, from another point of view, the fact is that not much research about such sensor designs has been reported so far, although they seem to show great sensitivity, fine selectivity at low concentrations, long-term stability, and reproducibility in terms of response time and recovery time.[168] These enhanced sensing behaviors were attributed to the presence of rGO with high conductivity and large surface accessibility, leading to fast mass transfer and the efficient adsorption of pollutants at a wide range of concentrations, and the positive motion of charge carriers at a high rate allowing easy diffusion across the whole sensor. Indeed, this is a potential finding that shows the advantages of this hybrid design for practical sensing applications. Of course, more effort is still needed to research and fabricate exceptional architectures that can suitably meet the requirements of an ideal sensor.

For biomedical applications, the incorporation of SFNs with graphene and GO to form magnetic composites has been developed more commonly when compared with other designs based on carbonaceous materials such as carbon dots, CNTs, *etc.* Both Yang and Wang employed $MnFe_2O_4$ NPs to decorate a GO surface and considered these to be effective carrier systems for the anti-cancer drug DOX owing to the superparamagnetic behavior.[169,170] In comparison with common carbonaceous materials, GO can be better dispersed in aqueous solutions, even under physiological conditions, through the large number of oxygen-containing functional groups, like carboxyl, hydroxyl and epoxide groups, on its large surface. Such groups help GO to directly connect with drug molecules *via* strong hydrophobic interactions and the π–π conjugate effect between GO and DOX, instead of using a surface activation approach based on some oxides or polymers with special functional groups to form new bonds to drug molecules.[169] Hence, the loading capacity on the surface is significantly enhanced, as is the sensitivity of direct interactions, making it a promising potential candidate for controlled drug delivery. Besides, in order to validate the potential of this hybrid design for MRI applications, $MnFe_2O_4$ and $CoFe_2O_4$ were used as promising solid-state contrast agents because of their superparamagnetic properties, large Curie temperatures, moderate saturation magnetization values, and magneto-crystalline anisotropy.[170–172] However, SFNs must have a small range of sizes to achieve the maximal magnetic moment, and some unintended phenomena can occur, such as colloidal instability and the self-aggregation or sedimentation of NPs, under physiological conditions. To overcome this problem, GO has been used as an ideal support for the uniform dispersion of NPs, leading to remarkable outcomes, not just for both T_1- and T_2-weighted imaging, but also for controlling the average size, dispersion, and magnetic characteristics of the composite, according to the results obtained from *in vitro* and *in vivo* MRI studies. More interestingly, as indicated by the most recent observations of Alazmi *et al.*,[162] GO is assumed to probably undergo some negative reactions under physiological conditions due to the abundant functional groups on its surface. Hence, replacing GO with rGO, which has a more inert surface, was considered a useful strategy to retain biocompatibility and to enhance the contrast and proton relaxivity coefficient for MRI applications. Namely, with various loading concentrations of $CoFe_2O_4$ NPs from 5 to 30 wt% in a hybrid design with rGO, T_2-weighted MR images at different concentrations of iron were taken using these samples along with agarose gel; they showed that the MRI signal intensity depended on the iron concentration and, furthermore, this hybrid design also exhibited a contrast enhancement effect in comparison with pure $CoFe_2O_4$ NPs. A highest proton relaxivity value of 102.1 $mM^{-1}\ S^{-1}$ at 30 wt% was obtained compared with previous reports (Fig. 9d). The detection of ledipasvir (LEDV) was reported for the first time by El-Wekil *et al.*[11] using a novel electrochemical sensing substrate made of $NiFe_2O_4$/rGO with the support of morpholinium acid sulfate (MHS). The large surface area and

layered structure of rGO helped to successfully prevent the aggregation of $NiFe_2O_4$ nanospheres, and to enhance the active surface area and electrocatalytic oxidation response to LEDV. As a result, the sensor exhibited a wide linear range from 0.4 to 350 ng mL^{-1} with a low detection limit of 0.133 ng mL^{-1}. Additionally, the results demonstrated that this hybrid design could be effectively employed in the quantitative detection of LEDV in human plasma and in pharmacokinetic studies, showing high sensitivity and selectivity, a low limit of detection (LOD), and good stability and reproducibility. Also, many other reports used SFNs in combination with GO and rGO with the aim of detecting alpha-fetoprotein,[173] DNA,[174] nicotinamide adenine dinucleotide (NADH), and H_2O_2.[175] Almost all of the obtained results exhibited promise for obtaining high-performance electrochemical sensors.

3.3. Hybrid designs between spinel ferrites (AFe_2O_4) and metals/metal oxides

3.3.1 Heteroatom-doped designs of spinel ferrite (AFe_2O_4) structures. To further understand the reason and purpose for choosing a doping route within SFN lattice structures, we know that the electrical and electrochemical properties, namely electronic conductivity, cycling performance, and rate capability, remarkably depend on the interaction and distribution of A^{2+} and Fe^{3+} spinel cation sites throughout the spinel crystal structure.[176–178] With the flexible ability of heteroatoms to replace and/or occupy the A^{2+} cation positions, critical changes can be created in the lattice parameters and crystallite sizes because of differences in the concentrations and radii of dopant cations, leading to the formation of defects and synergistic effects, delaying capacity loss.[179–181] A proper doping process provides many varied advantages for an electrode; among these is a significant increase in the number of transport channels and active sites within the unique porous nanosized structure arising from the stronger dopant-atom–oxide bonds with respect to the Fe–O ones, contributing to the promotion of lithium-ion diffusion and storage. Moreover, it seems to create a decrease in the interfacial resistance and facilitate the creation of a more compact and stable anode structure at a high C rate because the required energies for the formation of oxygen vacancies and for bond breakage between dopants and O_2 are lower compared with Fe^{3+} and O_2.[181,182] More particularly, the promotion of additional redox processes and the electrode chemical activity are some of the most important aspects, which need to be mentioned here. For example, in Tang's report,[177] *via* the redistribution of electric and spin densities between the dopant Mn and Zn^{2+} cations, and because of the density of the Li ions participating in the intercalation/deintercalation process and the diffusion coefficient (D_{Li}) of the SFN matrix, the electrochemical performance was remarkably increased, corresponding to a specific capacity of about 1547 mA h g^{-1} in the initial discharge process, which was maintained at 1214 mA h g^{-1} at 100 mA g^{-1} after 50 cycles, higher compared to a pure $ZnFe_2O_4$ electrode (Fig. 10a). Also, as can be seen, particle size and morphology, and the electrode kinetic parameters in terms of the resistance of the electrolyte (R_e), the resistance of SEI film (R_f), and R_{ct}, were evaluated and exhibited important positive changes after doping with Mn (Table 4). In the same vein, the use of Al and Ca as dopants to substitute for Zn^{2+} sites in $ZnFe_2O_4$ NPs was investigated to enhance the electrochemical effects.[179] On one hand, Al atoms exhibited beneficial results involving good reversibility at a high C rate with capacity values of about 80–100 mA h g^{-1}. Meanwhile, Ca ions showed low or almost no electrochemical effects after Ca doping due to slight lattice expansion resulting from its higher ionic radius compared with iron and zinc, leading to a breakdown effect from Ca on the spinel structure. Furthermore, its higher dimensionality and lower crystallinity degree prevented a suitable Li diffusion coefficient in the crystalline structure, thus, it did not seem to exhibit plain and useful electrochemical features. In another example, both Indhrajothi and Narsimulu chose La^{3+} and Sm^{3+} to dope $CoFe_2O_4$ NPs and used them as effective anode materials for LIB applications, respectively.[181,182] The great results in terms of rate performance and capacity retention over a large number of cycles also once again confirmed that the presence of La^{3+} and Sm^{3+} in $CoFe_2O_4$ NPs improved the capacity, structural stability, and metal oxidation reactions during the charge/discharge process through maintaining the number of Li ions involved compared with a pristine $CoFe_2O_4$ anode (Fig. 10b and c).

Not very surprisingly, the doping of SFNs has led to many outstanding results for both environmental purification and sensor applications. As is known, doping approaches using noble metals have been used popularly in many metal oxide semiconductors as an effective way of promoting sensitivity and selectivity for sensor applications. In fact, this approach has also been applied successfully to SFN semiconductors in a series of related reports.[183–189] On one hand, as already described in the LIB section, adjusting the lattice parameters, crystallite size, morphology, surface-to-volume ratio, and, especially in this case, the energy-band structure can contribute to creating more active centers and available reactants at the grain surface boundaries, leading to the promoted adsorption of target molecules on the sensor surface. On the other hand, kinetic competition between components and the electronic sensitization effects of noble metals have provided a critical natural route to enhancing the sensing properties: not only sensing performance but also the recovery/response times. Dopants can play the role as a catalyst, increasing the density of chemisorbed oxygen species on the sensor surface, reducing the activation energy of the reaction, and promoting reactions between chemically adsorbed oxygen species and the target molecules. A recent report by Lv revealed that the doping of Pd into the 3D structure of macroporous $ZnFe_2O_4$ resulted in a great improvement in the sensor response and selectivity, and excellent stability for acetone detection in comparison to lone macroporous $ZnFe_2O_4$ (ref. 183) (Fig. 10d). In addition to the mentioned "*catalytic effects*" and "*spill-over effects*", it was proposed that, due to the unique porous structure and abundant reaction sites both inside and outside the macroporous structure, accessibility of target molecules to the sensor surface was achieved at a high level. This was demonstrated through the high value of the specific surface area, approximately 38.2 m^2

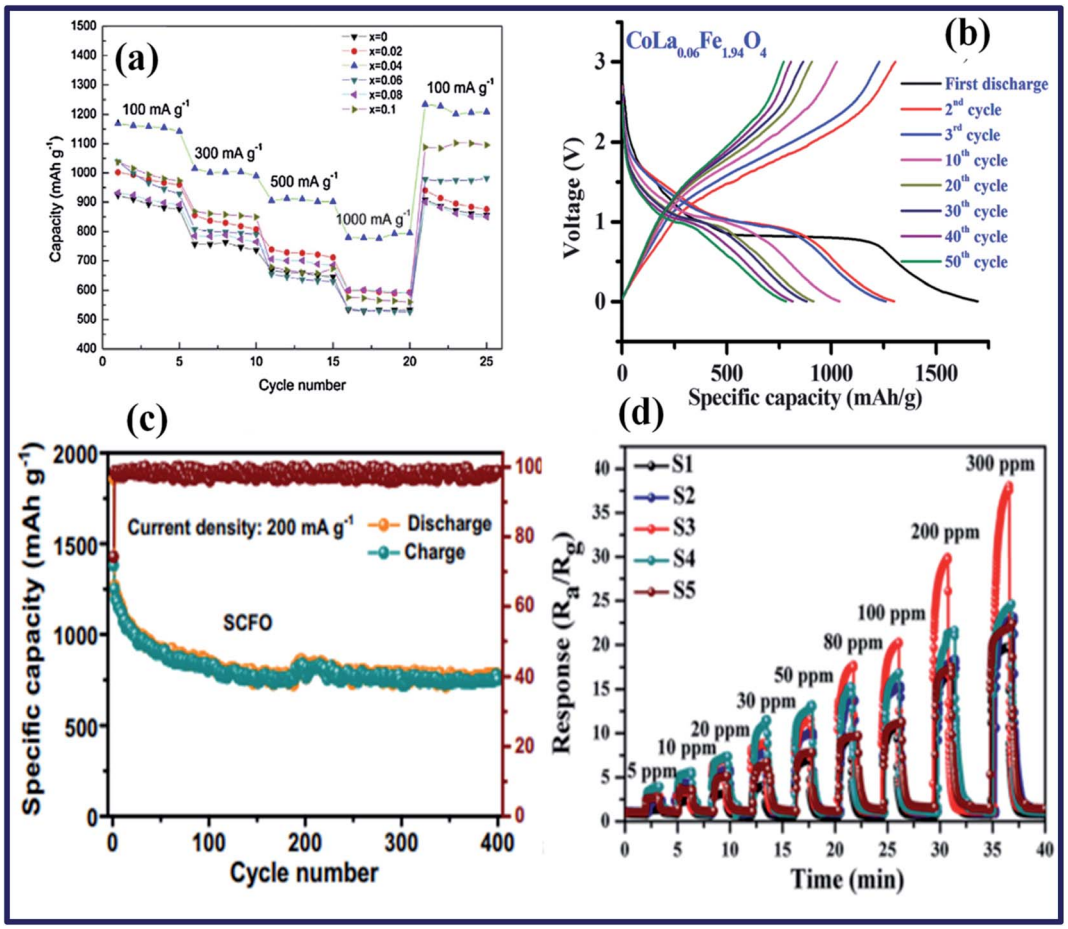

Fig. 10 (a) The rate capabilities of Mn–Zn ferrite powder with different Mn content. (b) Battery charge/discharge curves for a La-doped $CoFe_2O_4$ anode material. (c) The cycling performance of a Sm-doped $CoFe_2O_4$ electrode at a current density of 200 mA g^{-1}. (d) The dynamic gas-sensing response of Pd-doped $ZnFe_2O_4$ sensors with various Pd content levels to 5–300 ppm acetone (reprinted with permission from ref. 177 and 181–183; copyright: 2014 and 2015, Elsevier Ltd, copyright: 2019, The Royal Society of Chemistry, and copyright: 2020, Springer Nature, respectively).

Table 4 Electrode kinetic parameters obtained from the equivalent circuit fitting of experimental data from $Zn_{1-x}Mn_xFe_2O_4$ (x = 0, 0.02, 0.04, 0.06, 0.08, and 0.1)[177]

Mn content	R_e (Ω)	R_f (Ω)	R_{ct} (Ω)	I_o (mA cm^{-2})	D_{Li} (cm^2 s^{-1})
0.00	2.73	37.72	18.95	1.35	1.08×10^{-20}
0.02	2.12	20.53	7.04	3.64	1.96×10^{-19}
0.04	3.81	17.63	5.75	4.47	2.55×10^{-18}
0.06	2.73	35.81	9.63	2.67	1.37×10^{-19}
0.08	1.45	33.60	15.89	1.62	1.35×10^{-19}
0.10	4.28	27.71	11.19	2.29	2.47×10^{-18}

g^{-1}, which was two times higher than that of bare $ZnFe_2O_4$ NPs (16.2 m^2 g^{-1}). Similarly, for environmental applications, lanthanum (La^{3+}), manganese (Mg^{2+}), and cobalt (Co^{2+}) were doped successfully into spinel structures of $CoFe_2O_4$ and $MgFe_2O_4$ *via* various modified sol–gel methods.[187,190,191] The modification of the properties of $CoFe_2O_4$ when doped with La^{3+} ions were observed in detail, in which essential changes in coercivity and surface effects were considered to be mostly due to a decrease in the lattice parameters through a total reshuffling of the cationic arrangement of the spinel structure. Indeed, a remarkable increase in surface area of almost 70% was recorded following the addition of La^{3+} (from 74.3 to 109.3 m^2 g^{-1}). Besides, a lower optical band gap was observed, moving from 1.35 to 1.1 eV. These displayed properties showcase the promising potential for future advanced photocatalytic and adsorption material applications; moreover, real applications are possible because of the good reproducibility and stability, as described in Abraham's report with five cycles of reuse without any evident loss of catalytic activity.

The development of heteroatom-doped spinel ferrite structure designs that exhibit outstanding antibacterial properties has also been shown; this is desirable to meet the requirements for replacing some antibiotic medicines and for use as effective drug delivery systems. A perfect explanation of the antibacterial mechanism relating to these designs has not been given yet, but it has been proposed that the properties arise perhaps due to the penetration of NPs into the bacteria cell membrane, leading to morphology changes. Metal ions destroy the bacterial cell

wall, then the degradation of cytoplasm occurs, and, finally, cell death. The strong influences of the substitution or doping of various heteroatoms on the spinel lattice, particle size, shape, and antibacterial and magnetic properties, which are considered to be the most vital keys to the antibacterial activity, were investigated in detail.[192–195] Overall, the SFN crystal structure after doping shows a significant decrease in the growth of particle size, as well as an enhancement in the surface area and number of useful active sites. In almost all of the obtained results, the antibacterial efficiency of this hybrid design is better than other pure samples. Also, Apostolov *et al.*[196] demonstrated the possibility for using heteroatom-doped designs for magnetic hyperthermia applications. As is known, a suitable nanomaterial for magnetic hyperthermia applications must meet all the requirements, such as having a large M_s value, a large value of H_c, a NP size in the range of 20 nm, non-toxicity, and biocompatibility. The doping process causes a reduction in the particle size and phase transition temperature of spinel crystals. Also, an increase in the dopant concentration in SFNs leads to decreasing Curie temperature values, as demonstrated in many previous reports.[197–199] Based on this theory, M_s, H_c, effective anisotropy (K_{eff}), and specific absorption rate values as a function of concentration and size were determined in heteroatom-doped designs. For MRI applications, reports by both Alghamdi and Ghasemian showed the successful fabrication of hybrid designs of Cu–$ZnFe_2O_4$ and Co–$ZnFe_2O_4$ with important factors for enhancing the quality of images obtained *via* MRI with better image contrast.[200,201] At a suitable concentration of dopant, these hybrid structures promise MRI thermometry at near human body temperature.

3.3.2. Hybrid designs between spinel ferrites (AFe_2O_4) and metal oxides. Instead of using heteroatoms for insertion/replacement in spinel ferrite crystalline structures, metal oxides have also been investigated and utilized as potential candidates for hybrid designs, aiming to enhance electrochemical performance, because they have a high theoretical capacity, can be easily fabricated, are non-toxic, and have natural abundance. Herein, unique hierarchical hybrid designs involving SFNs and metal oxides can be divided into two major types: core–shell designs, and composite designs from random arrangements (Fig. 11a and b). Firstly, motivated by the unique characteristics resulting from rational integration and the inherent diverse properties of the individual constituents, as well as taking advantage of the secondary building blocks, smart coatings of metal oxides on the surfaces of nanorods, nanospheres, and even nanosheet arrays are evaluated as being capable of promoting electrochemical kinetics more effectively *via* endowing materials with larger surface areas, a more effective electrode–electrolyte exposure area, and more lithium storage sites, similar to the carbon-coated designs mentioned above. In fact, this can facilitate transport pathways for Li ions and electrolyte molecules, shorten the diffusion distance and resistance of the electrode material, and accommodate huge volume expansion during repeated insertion/extraction processes. It is worth noting that with the high stability and rich redox chemistry of the outside coating layers, these materials can not only play a role as a great protective buffer to support the mechanical integrity and structural stability, preventing the dissolution of active material into the electrolyte, but they can also contribute to offering additional specific capacity in the synthetic electrode. Thus, the electrochemical performances of these hybrid electrodes can be significantly improved. Indeed, Huang *et al.* firstly fabricated successfully hierarchical porous core–shell $NiFe_2O_4$@TiO_2 nanorods and $NiFe_2O_4$@Fe_2O_3 nanotubes with the help of diverse metal–organic frameworks (MOFs) as precursors followed by calcination treatment[90,202] (Fig. 11c). A uniform shell of TiO_2 was observed, about 16 nm in thickness, covering $NiFe_2O_4$ nanorods with a length of 300–600 nm. The enhancements in surface area and porosity were demonstrated *via* BET measurements, with an observed surface area of about 137.48 $m^2\ g^{-1}$ and a total pore volume of 0.26 $cm^3\ g^{-1}$. Besides, the structural stability can be seen, as the CE remained stable at around 98% even after 100 cycles and a reversible capacity of 1034 mA h g^{-1} was delivered. In contrast, for the uncoated $NiFe_2O_4$ electrode, these values decayed rapidly, achieving 321 mA h g^{-1} after 100 cycles. More interestingly, most recent designs based on core–shell structures have been developed and fabricated on a large scale using various special nanostructures, such as yolk–shell,[203] $MnFe_2O_4$@TiO_2 mesoporous spheres,[204] octahedral structures,[205] $NiFe_2O_4$/NiO@Fe_2O_3 nanocubes,[206] and $ZnFe_2O_4$@MnO_2 nanosheets.[207,208] Namely, Liu *et al.*[203] pointed out that a novel heterogeneous design of yolk–shell CuO@$CuFe_2O_4$ showed positive effects on the electrical and ionic conductivities owing to the high activity space of both the movable core and the hollow space between the core and shell. Like a large number of normal core–shell structures, the transportation of Li ions and electrons is also improved, and volume change is mitigated. Moreover, for the yolk–shell structure, it needs to be stressed that more active sites were created due to the additional inside core, leading to a higher trap density than for a normal core–shell structure. Clearly, this development is a promising new approach for designing effective SFN electrode materials for LIB applications. Secondly, for composite designs involving random arrangements between SFNs and metal oxides, the facile combination of the individual components with different morphologies can provide many unique features. There are not many changes in composition, but the appearance of synergistic effects among active materials with high theoretical capacity is still attributed as being the most important factor for improving the capacity. However, from a structural aspect, the self-growth and random arrangement create highly porous architectures with a large surface area containing micro- and macro-pores, and more sites for Li ion insertion, along with the formation of intimate interconnection effects, which are beneficial for the Li ion diffusion pathways and electron transfer, and buffering volume changes, leading to structural integrity, long-term cycle life, and good rate performance[10,209–213] (Fig. 11d). Besides, the self-growth and random arrangement offer a large number of open networks and extra spaces in the conductive skeletons, resulting in the full penetration of the electrolyte. As a result, Wang *et al.*[214] exhibited that the presence of dual-network porous/nanoporous $NiFe_2O_4$/NiO composites led to excellent lithium storage properties in terms of reversible

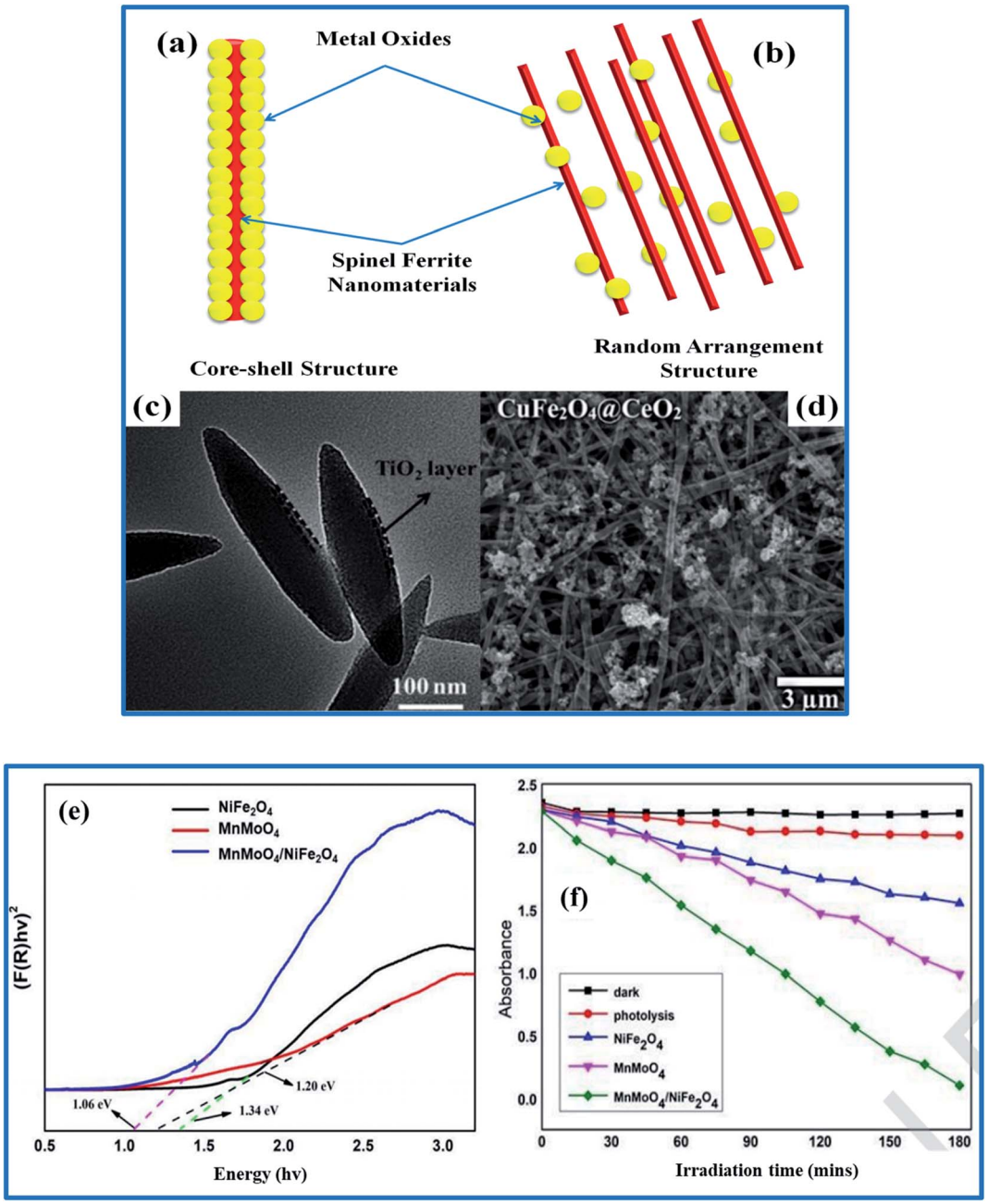

Fig. 11 (a and b) The two main hybrid designs involving SFNs and metal oxides. (c and d) TEM and SEM images of core–shell $NiFe_2O_4$@TiO_2 nanorods and $CuFe_2O_4$@CeO_2 nanofibers. (e and f) A Kubela–Munk plot of $MnMoO_4$/$NiFe_2O_4$ *via* UV-vis DRS measurements and the photodegradation of MB (reprinted with permission from ref. 90, 215 and 216; copyright: 2014, John Wiley and Sons, copyright: 2016, Balaban, and copyright: 2020, Elsevier Ltd, respectively).

capacity, rate performance, and cycling stability. A specific capacity of 1618 mA h g^{-1} was achieved after 100 cycles at 200 mA g^{-1}, higher than both pure $NiFe_2O_4$ and NiO.

With a focus not only on LIB applications, the tendency of hybrid designs involving SFNs and metal oxides to show structural stability, recyclability, shorter reduction times, and high catalytic efficiency for environmental uses has also generated increased attention with a rise in recent reports, as summarized in Table 5. Herein, synergistic effects arising from the co-catalytic properties of the SFN and metal oxide components still play a crucial role in supporting a high reaction activity and the rapid reduction of pollutants. As can be seen, as individual SFN and metal oxide components have varied rather wide band gaps, it is indeed challenging to reach excited states under visible light irradiation. In Paul's work, the effective integration of $NiFe_2O_4$ with $MnMoO_4$ resulted in a narrow bandgap (Fig. 11e) because of the formation not only of more efficient electron transfer channels between $MnMoO_4$ and $NiFe_2O_4$ interfaces but also a p–n heterojunction structure, which enhanced the harvesting of visible light.[216] Metal oxides and

Table 5 A comparison of catalytic activities of hybrid designs based on SFNs and metal oxides for the removal of contaminants from the environment[a]

Catalytic material	Target contaminant	Dosage (mg L^{-1})	Degradation (%)	Time (min)	Ref.
$CuS/CoFe_2O_4$	MB	25	100	30	219
$ZnS/CoFe_2O_4$ (core–shell)	MB	25	100	70	220
$CuO/CoFe_2O_4$ (core–shell)	MB	50	>90	—	218
SnO_2–$TiO_2/CoFe_2O_4$ (core–shell)	RhB	10	100	120	221
$ZnO/CoFe_2O_4$ (core–shell)	MB	10	100	60	222
$ZnO/CoFe_2O_4$ (composite)	HIn	10^{-6} M	89	60	223
$CuO/MnFe_2O_4$	LVF	1000	91.3	120	224
$ZnO/MnFe_2O_4$	CR	50	90.32	35	225
$MnO/ZnFe_2O_4$	CR	50	98.5	35	225
$InVO_4/ZnFe_2O_4$	MB	25	88.74	240	226
$ZnO/NiFe_2O_4$	CR	20	94.55	10	227
$MnMoO_4/NiFe_2O_4$	MB	6×10^{-5} M	96	180	216

[a] MB: methylene blue; RhB: rhodamine B; LVF: levofloxacin; HIn: phenolphthalein; CR: Congo red.

SFNs can act as catalyst supports, each aiming to restrain the crystallization and size growth of the other, as well as helping to form larger specific surface areas in these hybrid designs.[217] They also contributed to impeding the recombination of e^-/h^+ pairs and prolonging the lifetimes of photo-excited electrons. As a result, superior photocatalytic performance was shown, with 96% removal of MB at a rate constant 19 and 5 times higher than those of bare $NiFe_2O_4$ and $MnMoO_4$, respectively (Fig. 11f). More specially, the recovery and reusability of the $NiFe_2O_4$/$MnMoO_4$ catalyst without any negatively effects on its activity were observed, further confirming it to be a promising candidate for solving environmental problems. However, it needs to be stressed that unique features arising from the structural and morphology characteristics of the synthesized catalytic material remarkably affected the catalytic performance. For example, Huang and co-workers[218] fabricated a novel hollow core–shell $CoFe_2O_4$/CuO nanostructure to demonstrate its excellent catalytic performance for 4-nitrophenol removal. The hollow core–shell structure possessed a specific surface area of 36.86 m^2 g^{-1} and an abundant distribution of micro/mesopores, together with a large number of controlled dopants, leading to the construction of a stable open-framework, which minimizes the number of buried non-active metal atoms, leading to an increase in the number of active sites for the catalytic process and effective accessibility. More particularly, each $CoFe_2O_4$/CuO structural unit exhibited millions of nanoreactors in the entire inner hollow space, supporting the reduction process *via* relaying electrons.

On the other hand, some reports have also discovered the high adsorption capacities, along with the photodegradation properties, for toxic pollutants of these hybrid designs.[215,228,229] It is worth noting that synergistic effects contribute to optimizing the removal of pollutants with higher performances and faster reaction times. It can be believed that the high surface area from the formation of open networks may help improve target absorbance on both the surfaces and insides of the adsorbent. To study how pollutant adsorption can be carried out on the surface of the composite, Borhan *et al.*[228] assumed that MO itself created face-to-face dimers *via* π–π stacking interactions between aromatic rings. So far, two main adsorption mechanisms have been proposed, including chemisorption (the formation of new bonds) and electrostatic adsorption.[230,231] With a huge specific surface area of 220.5 m^2 g^{-1} and a Langmuir surface area of 315.4 m^2 g^{-1}, γ-Fe_2O_3@$NiFe_2O_4$ adsorbed most MO after 2 min. Also, its considerable magnetic behavior also largely solved any reuse issues. The formation of p–n junctions at the heterojunction interface between metal oxides and SFNs significantly affects the initial resistance (R_a) compared with pristine metal oxides for sensor applications.[232–234] A formed hierarchical hybrid structure provides more active sites for the target adsorption process and sensing reaction due to the large quantity of reaction sites and absorbed oxygen ion species on the surface. In addition, the effective and rapid diffusion rates of pollutants toward both the inner and surface regions of the adsorbent are supported by the existence of a porous structure arising from space between components. Therefore, a strong response and short response time towards 10 ppm H_2S gas were recorded in a report by Hu, approximately 20 times higher in comparison to the use of bare CuO microspheres.[235]

For biomedical applications, combining SFNs and metal oxides is considered to be a facile approach for enhancing the biocompatibility, dispersibility in water, and thermostability of SFNs. For example, Kamzin *et al.*[236] pointed out the great efficiency of using inert SiO_2 coating layers to protect SFNs from size increases, aggregation, and leaching under physiological conditions. Along with that, the formation of new strong bonds between silane groups and other functional groups, as well as covalent bonds (–Si–O–Si–) in biological systems, completely replaced weak interactions in the material architecture. Studies of the magnetic and Mössbauer properties exhibited that the $MgFe_2O_4/SiO_2$ nanocomposites had a Curie temperature in the range of 320 K, which is promising for hyperthermal therapy. Likewise, the surface modification of $NiFe_2O_4$ and $MnFe_2O_4$ by TiO_2, SiO_2, and CuO/FeO also showed outstanding features for biosensor use.[237–239] A novel biosensor was constructed based on $NiFe_2O_4$/CuO/FeO–CS nanocomposites to quantify cholesterol

oxidase (ChO_x).[237] Through tight connections between ChO_x and the surface of the $NiFe_2O_4$/CuO/FeO design modified by CS, this unique sensor provided a wide linear dynamic range from 50 to 5000 mg L^{-1}, a low detection limit of 313 mg L^{-1}, a high sensitivity of 0.043 μA mg L^{-1} cm^2 even at low concentrations, a fast response time of about 10 s, and long-term reusability over 3 months. For other applications, a hybrid between SFNs and metal oxides, more specifically between ZnO and $ZnFe_2O_4$, exhibited great suitability for MRI applications.[240] The poor dispersity of ZnO/$ZnFe_2O_4$ composites was promoted *via* surface modification with a hydrophilic molecule (dehydroascorbic acid (DHA)). The MRI contrast properties of the synthetic material were studied *via* T_1- and T_2-weighted MRI imaging, and the obtained T_1 and T_2 relaxivity values were 21.76 and 0.148 ppm^{-1} mS^{-1}.

3.4. Hybrid designs between spinel ferrites (AFe_2O_4) and transition-metal dichalcogenides (MS_2)

Recently, combinations between SFNs and MS_2 (MoS_2 and WS_2) have received lots of attention from researchers for energy storage applications because of the electronic flexibility and unique layered structure of MS_2. Like graphene and GO, the presence of the 2D layered structure of MS_2 results in a uniform and large surface area, along with weak van der Waals forces and covalent bonds between layers arising from three stacked atomic layers (S-M-S). This facilitates the easy access of Li ions and electrons, as well as providing more channels for Li ions and electron transportation.[241–243] Moreover, due to its inherently good electrical conductivity and strong connectivity with other materials, MS_2 can improve the retention capacity and cycling stability significantly. This was proved in Zhao's report, when $NiFe_2O_4$/MoS_2 composites displayed excellent capacity retention of over 90.7% after 3000 cycles, acting as a promising electrode for supercapacitors.[244] In another example, Jiang *et al.*[241] fabricated for the first time ternary composites of $ZnFe_2O_4$/MoS_2/rGO, which showed good electrochemical properties owing to the synergistic effects of MoS_2 with its three-dimensional conductive networks. The obtained discharge capacity was about 1568 mA h g^{-1} after 100 cycles at 200 mA g^{-1} and high rate performance was observed. These great results were compared with some previous reports to see the innovation arising from the existence of MS_2 in the hybrid designs (Table 6). Although the advantages of the hybrid design between MS_2 and SFNs cannot be denied, research relating to this field has not, in fact, been much reported yet, and thus further investigations are essential.

For environmental applications, the presence of crystallized MS_2 layers with excellent electronic conductivity is considered to be suitable for the construction of heterostructures, creating the advantages of a close coating on semiconductors instead of using standard carbonaceous materials. With its highly reactive edge sites owing to unsaturated S atoms and narrow bandgap, MS_2 can also strongly absorb in the visible region and improve the light utilization efficiency.[249–256] Unfortunately, self-stacking among MS_2 layers increases the S-M-S layer thickness and simultaneously reduces the exposure of active edge sites. Furthermore, the conductivity among the vertically aligned interlayers is smaller than that among the horizontal intralayers. Notably, a hybrid approach involving SFNs, inhibiting the aggregation of MS_2 layers as well as regaining their electronic conductivity, is very promising in the area of photodegradation. Also, these hybrid designs are expected to show stability and retrievability because their high magnetization is strong enough to separate them from reaction mixtures.[249,250] Fan *et al.*[257] demonstrated that the formation of stable $MgFe_2O_4$/MoS_2 heterostructures provided higher contact interfacial areas and lower R_{ct} values due to reducing defects at the interface and enhancing the separation and mobility of e^-/h^+ pairs. As a result, an optimal photoelectrochemical degradation rate of tetracycline (TC) of up to 92% was achieved. To understand more clearly the enhancement in the separation and mobility of the e^-/h^+ pairs and the light-harvesting efficiency, Ren *et al.*[249] pointed out that in the visible light region, both $CoFe_2O_4$ and MoS_2 in the hybrid design can be excited to create more e^-/h^+ pairs. The electrons formed in the conduction band (CB) of MoS_2 can quickly transfer to the CB of $CoFe_2O_4$ at the exposure interface because of the difference in the CB potentials; thus, the holes in the VB of MoS_2 have a more long-term lifetime, as shown in Fig. 12a. More importantly, as seen in Table 7, when comparing the addition of various amounts of MoS_2 into the hybrid design, the obtained results once again confirmed the important changes in the photocatalytic performance and the synergetic effects between the MoS_2 and $CoFe_2O_4$ co-catalysts.

Most efforts have been aimed at creating new hybrid structures to remove toxic pollutants from the environment, however, to the best of our knowledge, less effort seems to have been devoted to sensor applications, where it is challenging to find any reports associated with this field to date. Normally,

Table 6 A comparison of electrochemical performance between $ZnFe_2O_4$/MoS_2/rGO, $ZnFe_2O_4$/C, MoS_2/C, MoS_2/graphene, $ZnFe_2O_4$/graphene, and $ZnFe_2O_4$ for LIB applications

Electrode material	Current density (mA g^{-1})	Coulombic efficiency (%)	Capacity retention/cycles	Ref.
$ZnFe_2O_4$	116	69	833.6/50	245
$ZnFe_2O_4$/C	65	80	841/30	246
MoS_2/C	100	82	601.7/50	244
MoS_2/graphene	100	67	1100/100	247
$ZnFe_2O_4$/graphene	100	59.2	956/50	248
$ZnFe_2O_4$/MoS_2/rGO	200	76.5	1568/100	241

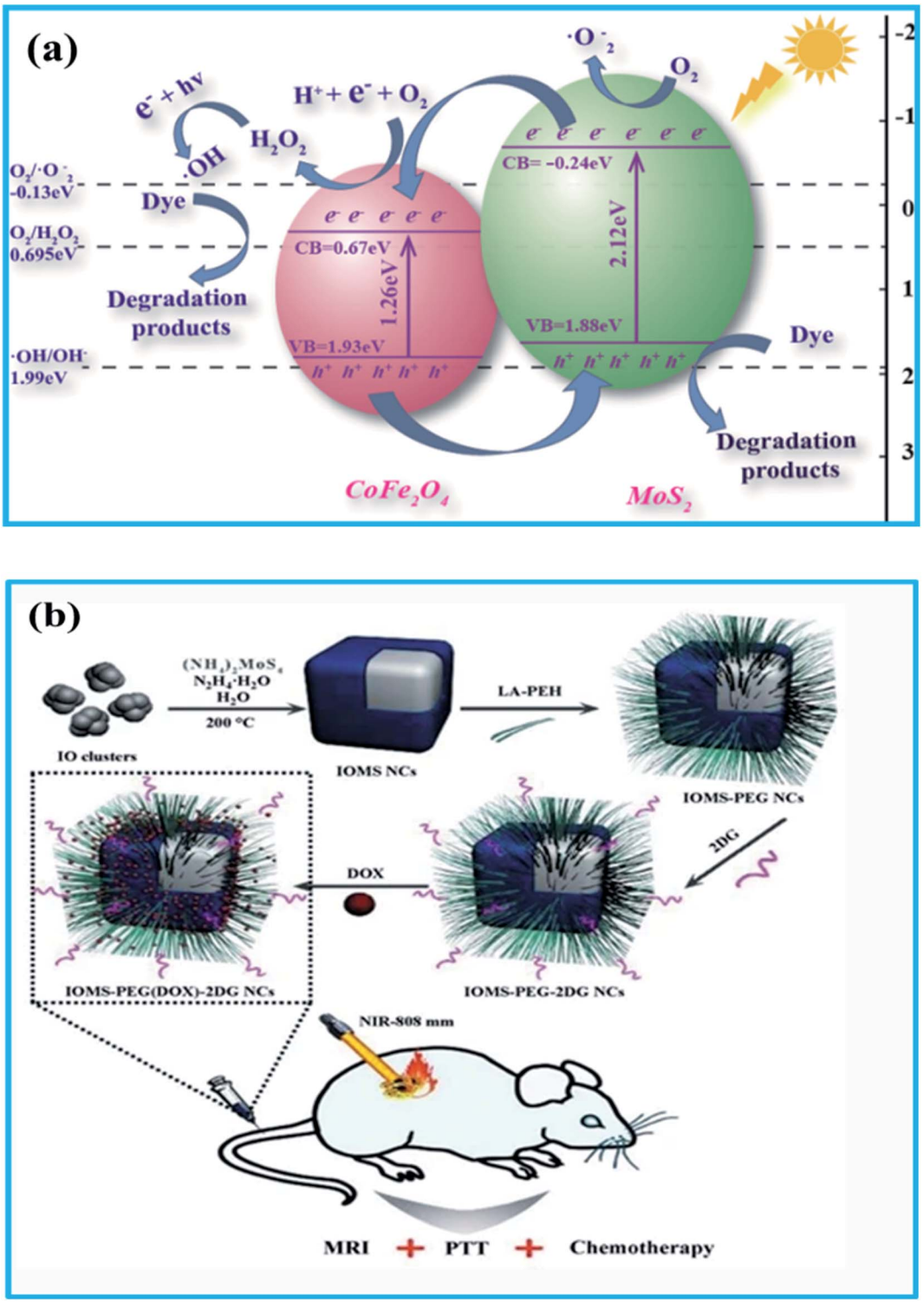

Fig. 12 (a) A possible mechanism explaining the photocatalytic activity of $CoFe_2O_4/MoS_2$ heterojunctions for the degradation of CR under visible light irradiation. (b) A schematic illustration of the fabrication process of IOMS-PEG(DOX)-2DG NCs for MRI-guided chemo-photothermal cancer therapy (reprinted with permission from ref. 249 and 258; copyright: 2018, Elsevier Ltd.).

a sensing mechanism is based on resistance changes arising from chemical reactions on a semiconductor oxide surface. Meanwhile, the combination of MS_2 and SFNs is considered to have the ability to create an effective exposure interface and large surface area, which can enrich surface reactions. Thus, it would be very worthwhile to take advantage of these benefits for sensor applications, aiming to develop high-performance sensing materials with high sensitivity, low detection limits, and fast response/recovery speeds.

Table 7 A summary of kinetic data from the photocatalytic degradation of CR using prepared photocatalysts under visible light irradiation[249]

No.	Photocatalyst	Degradation efficiency (%)	Rate constant, k (min^{-1})	R^2
1	$CoFe_2O_4$	7.3	0.095×10^{-3}	0.940
2	MoS_2	22.4	3.49×10^{-3}	0.954
3	$CoFe_2O_4/MoS_2$ (0.5)	59.1	11.6×10^{-3}	0.968
4	$CoFe_2O_4/MoS_2$ (1)	94.9	44.1×10^{-3}	0.977
5	$CoFe_2O_4/MoS_2$ (2)	63.6	14.9×10^{-3}	0.967

Table 8 Some hybrid designs based on SFNs and polymers for the removal of toxic pollutants[a]

Catalytic material	Target contaminant	Dosage (mg L^{-1})	Degradation (%)	Time (min)	Degradation retention/cycles	Ref.
$CS/CoFe_2O_4$	2-CP	100	95.4	240	80/4	270
$PEG/CoFe_2O_4$	CR	100	—	—	—	271
$CS/CoFe_2O_4$	IBD	750	93.12	15	—	272
$SA@CoFe_2O_4$–PDA	MB	100	92.71	60	—	273
$P\text{-}CS/CoFe_2O_4$	Pb(II), Cd(II)	40	97.45, 92.15	—	—	266
$CS/CoFe_2O_4$, $CS/NiFe_2O_4$	Cd(II)	40	95, 92	90	70/7	274
$Ppy/CoFe_2O_4$	RhB	10	99.7	120	91.2/5	268
$Pth/NiFe_2O_4$	JG	70	94.6	60	72.8/4	267
$PANI/NiFe_2O_4$	ARS	30	93.8	90	82/6	275
$PPy/NiFe_2O_4$	Cr(VI)	500	99.79	—	—	276
$DNSA/CS/MnFe_2O_4$	MB	60	98.9	30	83.1/5	277
$CPVC/MgFe_2O_4$	Cr(VI)	20	100	160	96/6	278
$SnFe_2O_4/g\text{-}C_3N_4$	RhB	—	99	30	—	279

[a] CS: chitosan; 2-CP: 2-chlorophenol; PEG: polyethylene glycol; IBD: indigotine blue dye; SA: alginate beads; PDA: polydopamine; MB: methylene blue; PPy: polypyrrole; RhB: rhodamine B; Pth: polythiophene; JG: janus green B; PANI: polyaniline; ARS: alizarin red S; DNSA: 3,5-dinitrosalicylic acid; MO: methyl orange; CPVC: conjugated polyvinyl chloride.

According to observations from the literature, it seems that hybrid designs based on AFe_2O_4 and MS_2 for biomedical applications have only been recently examined. However, the obtained results are extremely impressive, showing great potential in some fields such as drug delivery, hyperthermia, and, especially, MRI applications. By only evaluating the basic characteristics of $MnFe_2O_4/MoS_2$ design, Wang *et al.*[259] proved that this design had a high surface area of 97.16 $m^2 g^{-1}$, without the appearance of aggregation phenomenon or the restacking of layered MoS_2; more importantly, it showed superior superparamagnetic behavior with high magnetic sensitivity and excellent solution dispersibility, making it promising for various biomedical applications. Also, to enhance the circulation time in the blood and the accumulation of drugs at cancer sites and to ease drug loading on the hybrid design, in a recent report, a hybrid design of $Fe_3O_4@MoS_2$ nanocubes (IOMS NCs) not only was modified using PEGylation and 2-deoxy-D-glucose (2-DG), but it also was investigated in detail for targeted MRI-guided precise chemo-photothermal therapy (Fig. 12b). The results exhibited a T_2 relaxivity coefficient of 48.86 mM^{-1} s^{-1} and great chemo-photothermal effects. The fast and clear detection of tumor sites after injection was recorded based on the T_2-weighted contrast ability of the MRI signal. Upon exposure to NIR laser radiation and the appearance of an external magnetic field, fast temperature increases at the tumor site were found, causing the successful inhibition of tumor growth.[258] The same results were observed in reports by Liu[260] and Yu,[261] where MoS_2/Fe_3O_4 composites were functionalized using polyethyleneimine (PEI) and polyethylene glycol (PEG), respectively. These composites showed excellent T_2-weighted MRI and photoacoustic trimodal bioimaging (PAT) abilities, as well as great magnetically targeted chemo-photothermal antitumor efficacy stemming from the successful combination of photothermal therapy, photodynamic therapy, and chemotherapy triggered by strong NIR absorption.

3.5. Hybrid designs between spinel ferrite (AFe_2O_4) and other materials

Although hybrid designs based on SFNs, polymers, and other unique nanomaterials have not found LIB applications to date, they have been employed and studied in detail as innovative electrodes for supercapacitor and Na battery applications.[91,262] In a recent report by Scindia,[91] the fabrication of a special core–shell structured electrode from $NiFe_2O_4$ and Ppy yielded extremely promising specific capacitance and high stability, with a specific capacitance of 721.66 F g^{-1}, specific energy of 51.95 W h kg^{-1}, specific power of 6.18 kW kg^{-1}, and CE of 99.08%. The superior results were mainly ascribed to the uniform distribution of SFN in the conductive polymer matrix and the strong interconnections in the structure. Like the above-mentioned carbonaceous materials, in this case, conductive polymers not only act as conducting agents and

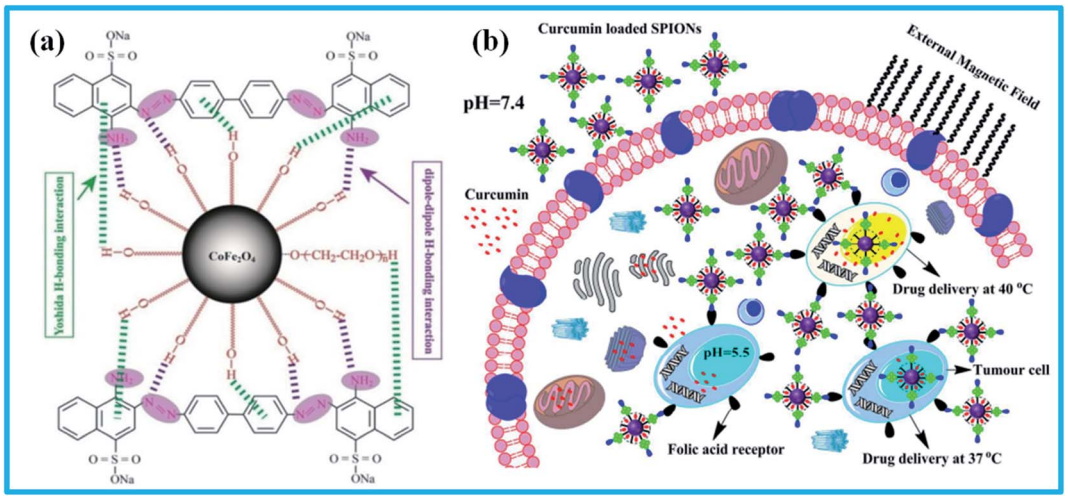

Fig. 13 (a) The proposed adsorption mechanism of CR on the as-synthesized samples. (b) A schematic illustration of the tumor cell uptake of curcumin with and without the drug carrier, along with a representation of the promoted and targeted uptake in the presence of an external magnetic field (reprinted with permission from ref. 271 and 286; copyright: 2016, Elsevier Ltd, and copyright: 2015, American Chemical Society Publications, respectively).

supporting matrices to enhance the diffusion and transport of electrons/ions, but they also relieve the strain during huge volumetric change, leading to enhanced conductivity and structural stability. Also, hybrid designs between SFNs and alloys/carbon nanomaterials with three-dimensional structures have also been evaluated widely for LIB applications.[263–265] It is not surprising that the electrochemical performance reaches a high level and the cycling stability is promoted remarkably, owing to synergistic combinations between the individual constituents. Indeed, the abundance and flexibility of interfacial surfaces, active sites within the 3D-hierarchical spaces, and the close attachment between the two materials again favor the charge-transfer reaction and Li-ion storage in this design.

From an environmental perspective, some special hybrids between SFNs and other nanomaterials, in particular conductive polymers, seem to show many impressive results for the adsorption and photodegradation of toxic pollutants, as described in Table 8. Properties such as ease of fabrication, high carrier mobility, chemical stability, flexible morphology, high surface area, large porosity, and the specificity of functional groups in polymer chains when coordinating and interacting with contaminants all help these materials to become some of the most important adsorbents, even though there are separation and regeneration difficulties[266,267] (Fig. 13a). The combination of SFNs with polymers not only solves reusability issues, thanks to magnetic recyclability under an external magnetic field, but it also helps to optimize the merits of potential photocatalysts/adsorbents (SFNs) with narrow bandgap energies, leading to improved electron transfer capabilities, light absorption, and optical absorption. Deng *et al.*[268] demonstrated that, owing to the above merits, Ppy/$CoFe_2O_4$ nanocomposites could serve as a convenient, effective, reusable, and recyclable photo-Fenton catalyst for the degradation of RhB in the presence of H_2O_2. Moreover, great catalytic activities were still observed after 5 cycles, demonstrating the successful combination and the outstanding synergistic effects between the Fenton activity and photocatalytic activity. In another report, the formation of a 3D hierarchical porous structure based on a hybrid of $ZnFe_2O_4$ NPs and MgAl-LDH nanosheets led to synthetic composites with a high adsorption capacity for CR of about 294.12 mg g^{-1} *via* strong electrostatic attraction and anion exchange between functional groups and the adsorbent, as well as notable recyclability.[269] Clearly, due to the above great abilities, strong potential is demonstrated for wide-spread and large-scale practical applications, especially pollutant removal from the environment, in the future.

The fact also is that there are many studies evaluating the usability of hybrid designs involving SFNs and other polymers for hyperthermia or targeted drug delivery applications, such as $CoFe_2O_4$-coated PEG,[280] poly(maleic anhydride-*alt*-1-octadecene) (PMAO),[281] $MnFe_2O_4$-coated poly(*N*-isopropyl acrylamide-*co*-acrylamide),[282] PEG,[283] poly(isobutylene-*alt*-maleic anhydride) (PBMA-*g*-C_{12}),[284] CS,[285] poly(*N*-isopropyl acrylamide-*co*-glutamic acid),[286] $ZnFe_2O_4$-coated CS,[287] and $NiFe_2O_4$ coated with PEG.[288] Indeed, for a long time, polymers were popularly used in biomedical fields, such as in cell immobilization, in drug delivery, and as carriers in tissue engineering thanks to their good dispersibility, inertness in biological systems, non-toxicity, high biocompatibility, and flexibility. With rich functional groups in the molecule structures, polymers can strongly associate with other materials *via* strong chemical bonds or weaker interactions, like electrostatic interactions and van der Waals interactions. Here, the appearance of polymers as effective surface modifiers in SFN-based designs not only creates stable connections between SFNs and polymers but also makes drug loading at higher levels easier and more effective. Furthermore, this contributes to preventing the agglomeration of SFNs, improving their long-term stability in water and under physiological conditions. Patra *et al.*[286] constructed polymer-modified superparamagnetic iron oxide NPs (SPIONs), and

this design offered an outstanding loading capacity and the efficient encapsulation of curcumin, 89% and 98%, respectively, and showed an effective and fast drug release process. A large amount of the SPION-loaded curcumin (99%) was easily guided to the target site at a distance of 30 cm in 2 min due to the superparamagnetic properties of SFNs. Then, the localized hyperthermia process was carried out there, and the obtained results showed a very fast and efficient temperature increase under the effects of an external magnetic field (Fig. 13b). The same result was also recorded in Shah's report where the temperature of PEG-coated $MnFe_2O_4$ in a magnetic fluid rose from 25 to 45 °C in about 22 min in the presence of a high-frequency magnetic field.[283] Simultaneously, these hybrid designs exhibited promising antibacterial effects against both Gram-negative and Gram-positive bacteria.[289,290] From all these studies, it can be seen that the combination of SFNs and polymers is an excellent approach for targeted drug delivery and localized hyperthermia for cancer tumor treatment.

More interestingly, some special materials, such as TEOS, PVP, glucose oxidase, and CS were employed to hybridize SFNs, aiming to create biosensors with detection sensitivity, high specificity, good reproducibility, and high stability.[291–293] Zeynali and co-workers[293] demonstrated that PVP-modified $CoFe_2O_4$@-CdSe/GCE showed an excellent electrocatalytic response towards the oxidation of rifampicin. In this case, PVP served as an effective protective shell for the outer surface of the SFN; also, the presence of CdSe is of very particular importance to increase the optical and electrical properties, and the stability of the synthetic composites. As a result, the sensor exhibited a wide linear range, high biocompatibility, and a very low detection limit (4.55×10^{-17} M), suggesting that it is a promising candidate to act as a novel basis for the fabrication of electrochemical biosensors in the future.

4. Summary and future perspectives

The study of recent reports on using SFN-based heterostructured designs as smart and effective nanomaterials for Li-ion storage, environmental monitoring, and biomedical applications has demonstrated that researchers are more and more attuned to the outstanding advantages of these hybrid designs. The unique morphologies, physicochemical and superparamagnetic properties, and electrochemical properties arising from suitable combinations of SFNs and various components, such as carbonaceous materials, metal/metal oxides, and TMDs, are very beneficial and consistent with the modern demands for nanomaterial development. In this review, recent developmental progress relating to SFN-based hybrid designs has been has been summarized in detail and logically for the following 4 major hybrid structures: SFNs/carbonaceous nanomaterials; SFNs/metal–metal oxides; SFNs/MS_2; and SFNs/other materials. Each hybrid structure has been analyzed and assessed individually from the perspective of additional interactions, combination effects, and its potential use in LIBs, environmental monitoring, and biomedical applications. Of course, each mentioned hybrid design has its own specific advantages and disadvantages arising from differences in morphologies, structures, and even active compositions, however they share common benefits arising from great electron conductivity, high charge carrier mobility, large surface area, physicochemical and structural stability, positive electrode/electrolyte interactions, and inner exposure of electrode materials to electrolytes, leading to significant increases in LIB capacitance, energy density, volume density, rate performance, and cycle life. Furthermore, some unique features, such as high biocompatibility, good biodegradability, nontoxicity, high dispersity, and, most importantly, high coercivity and magnetic anisotropy, good superparamagnetic properties, and moderate M_s values, help these hybrid structures to act appropriately for a variety of biomedical applications, for instance, targeted delivery, hyperthermia, MR imaging, *etc.* With these properties, SFN-based hybrid designs also feature on a list of ideal adsorbents, photocatalysts, and sensors, with high removal efficiencies, good sensitivity and selectivity, wide linear ranges, safety, stability, low cost, and, particularly, high reusability and recyclability, for a wide range of environmental pollutant treatment applications.

In future designs, continuing to utilize the great advantages while overcoming issues is a real challenge. Optimizing and controlling the effective size growth, dimensions, morphology, porosity, the weight proportions of material components, and synthesis techniques may be very promising pathways. Besides, a few hybrid designs have not yet been applied or studied widely in some specific areas, as discussed in the sections above, suggesting that these should be investigated and reported on in more detail to assess their potential properly. To be honest, summarizing and finding common development trends relating to SFN-based designs in a complete and detailed manner in all three fields, LIBs, environmental monitoring, and biomedical applications, is extremely difficult when they are regularly applied and widely evaluated in many different fields on a daily basis. We know that this report may not be comprehensive in all three areas, but it is an attempt to help readers get an overview and obtain the simplest approach when starting to develop and research SFNs. For future prospects, this will be an important and useful review, which can contribute to the development of SFNs for near-future technological applications.

Conflicts of interest

There are no conflicts to declare.

Acknowledgements

This research was funded by the Vietnam National Foundation for Science and Technology Development (NAFOSTED) under grant number 103.02-2019.01.

References

1 W. S. Galvão, D. M. A. Neto, R. M. Freire and P. B. A. Fechine, Super-Paramagnetic Nanoparticles with Spinel Structure: A Review of Synthesis and Biomedical Applications, *Solid State Phenom.*, 2015, **241**, 139–176.

2 Q. W. D. Chen, R. Wang and G. Shen, Ternary oxide nanostructured materials for supercapacitors: a review, *J. Mater. Chem. A*, 2015, **3**, 10158–10173.
3 D. H. K. Reddy and Y.-S. Yun, Spinel ferrite magnetic adsorbents: alternative future materials for water purification?, *Coord. Chem. Rev.*, 2016, **315**, 90–111.
4 T. N. Pham, J. Hur, I. T. Kim, Y. Lee and Y.-C. Lee, Hybrid Electrode Innovations in Triple and Quadruple Dimensions for Lithium-Ion Batteries, *ChemElectroChem*, 2019, **6**, 5911–5927.
5 H. Gao, S. Liu, Y. Li, E. Conte and Y. Cao, A Critical Review of Spinel Structured Iron Cobalt Oxides Based Materials for Electrochemical Energy Storage and Conversion, *Energies*, 2017, **10**, 1787.
6 K. K. Kefeni, B. B. Mamba and T. A. M. Msagati, Application of spinel ferrite nanoparticles in water and wastewater treatment: a review, *Sep. Purif. Technol.*, 2017, **188**, 399–422.
7 M. Kumar, H. Singh Dosanjh, Sonika, J. Singh, K. Monir and H. Singh, Review on magnetic nanoferrites and their composites as alternatives in waste water treatment: synthesis, modifications and applications, *Environ. Sci.: Water Res. Technol.*, 2020, **6**, 491–514.
8 A. Šutka and K. A. Gross, Spinel ferrite oxide semiconductor gas sensors, *Sens. Actuators, B*, 2016, **222**, 95–105.
9 M. Amiri, M. Salavati-Niasari and A. Akbari, Magnetic nanocarriers: evolution of spinel ferrites for medical applications, *Adv. Colloid Interface Sci.*, 2019, **265**, 29–44.
10 S. Balamurugan, M. D. Devi, I. Prakash and S. Devaraj, Lithium-ion doped $NiFe_2O_4/SiO_2$ nanocomposite aerogel for advanced energy storage devices, *Appl. Surf. Sci.*, 2018, **449**, 542–550.
11 M. M. El-Wekil, A. M. Mahmoud, S. A. Alkahtani, A. A. Marzouk and R. Ali, A facile synthesis of 3D $NiFe_2O_4$ nanospheres anchored on a novel ionic liquid modified reduced graphene oxide for electrochemical sensing of ledipasvir: application to human pharmacokinetic study, *Biosens. Bioelectron.*, 2018, **109**, 164–170.
12 M. A. Gabal, N. G. Al-Zahrani, Y. M. Al Angari, A. A. Al-Juaid, M. A. Abdel-Fadeel, S. R. Alharbi and R. M. El-Shishtawy, $CoFe_2O_4$/MWCNTs nano-composites structural, thermal, magnetic, electrical properties and dye removal capability, *Mater. Res. Express*, 2019, **6**, 105059.
13 T. Tatarchuk, M. Naushad, J. Tomaszewska, P. Kosobucki, M. Myslin, H. Vasylyeva and P. Ścigalski, Adsorption of Sr(II) ions and salicylic acid onto magnetic magnesium-zinc ferrites: isotherms and kinetic studies, *Environ. Sci. Pollut. Res.*, 2020, **27**, 26681–26693.
14 D. S. Mathew and R.-S. Juang, An overview of the structure and magnetism of spinel ferrite nanoparticles and their synthesis in microemulsions, *Chem. Eng. J.*, 2007, **129**, 51–65.
15 K. E. Sickafus, J. M. Wills and N. W. Grimes, Structure of Spinel, *J. Am. Ceram. Soc.*, 1999, **82**, 3279–3292.
16 L. Néel, Théorie du traînage magnétique des substances massives dans le domaine de Rayleigh, *J. Phys. Radium*, 1950, **11**, 49–61.
17 I. Ganesh, A review on magnesium aluminate ($MgAl_2O_4$) spinel: synthesis, processing and applications, *Int. Mater. Rev.*, 2013, **58**(2), 63–112.
18 T. Tatarchuk, A. Shyichuk, J. Lamkiewicz and J. Kowalik, Inversion degree, morphology and colorimetric parameters of cobalt aluminate nanopigments depending on reductant type in solution combustion synthesis, *Ceram. Int.*, 2020, **46**, 14674–14685.
19 P. R. Garcês Gonçalves, H. A. De Abreu and H. A. Duarte, Stability, Structural, and Electronic Properties of Hausmannite (Mn_3O_4) Surfaces and Their Interaction with Water, *J. Phys. Chem. C*, 2018, **122**, 20841–20849.
20 S. Raghuvanshi, S. N. Kane, T. R. Tatarchuk and F. Mazaleyrat, Effect of Zn addition on structural, magnetic properties, antistructural modeling of $Co_{1-x}Zn_xFe_2O_4$ nano ferrite, *AIP Conf. Proc.*, 2018, **1953**, 030055.
21 B. F. Bogacz, R. Gargula, P. M. KurzyeBo, A. T. Ph'dziwiatr, T. Tatarchuk and N. D. J. A. P. P. A. Paliychuk, Two-level model description of superparamagnetic relaxation in nanoferrites $(Co,Zn)Fe_2O_4$, *Acta Phys. Pol., A*, 2018, **134**, 993–998.
22 P. V. Kovtunenko, Defect formation in spinels in oxygen nonstoichiometry (a review), *Glass Ceram.*, 1997, **54**, 143–148.
23 D. M. A. N. W. S. Galvao, R. M. Freire and P. B. A. Fechine, Super-paramegnetic Nanoparticles with Spinel Structure: A Review of Synthesis and Biomedical Applications, *Solid State Phenom.*, 2016, **241**, 139–176.
24 T. Tatarchuk, N. Paliychuk, M. Pacia, W. Kaspera, W. Macyk, A. Kotarba, B. F. Bogacz, A. T. Pędziwiatr, I. Mironyuk, R. Gargula, P. Kurzydło and A. Shyichuk, Structure–redox reactivity relationships in $Co_{1-x}Zn_xFe_2O_4$: the role of stoichiometry, *New J. Chem.*, 2019, **43**, 3038–3049.
25 T. Tatarchuk, I. Mironyuk, V. Kotsyubynsky, A. Shyichuk, M. Myslin and V. Boychuk, Structure, morphology and adsorption properties of titania shell immobilized onto cobalt ferrite nanoparticle core, *J. Mol. Liq.*, 2020, **297**, 111757.
26 T. Tatarchuk, M. Myslin, I. Mironyuk, M. Bououdina, A. T. Pędziwiatr, R. Gargula, B. F. Bogacz and P. Kurzydło, Synthesis, morphology, crystallite size and adsorption properties of nanostructured Mg–Zn ferrites with enhanced porous structure, *J. Alloys Compd.*, 2020, **819**, 152945.
27 Z. Zhang, G. Yao, X. Zhang, J. Ma and H. Lin, Synthesis and characterization of nickel ferrite nanoparticles via planetary ball milling assisted solid-state reaction, *Ceram. Int.*, 2015, **41**, 4523–4530.
28 F. Chen, M. Chen, C. Yang, J. Liu, N. Luo, G. Yang, D. Chen and L. Li, Terbium-doped gadolinium oxide nanoparticles prepared by laser ablation in liquid for use as a fluorescence and magnetic resonance imaging dual-modal contrast agent, *Phys. Chem. Chem. Phys.*, 2015, **17**, 1189–1196.

29 L. Chen, Y. Shen and J. Bai, Large-scale synthesis of uniform spinel ferrite nanoparticles from hydrothermal decomposition of trinuclear heterometallic oxo-centered acetate clusters, *Mater. Lett.*, 2009, **63**, 1099–1101.

30 J. Li, H. Yuan, G. Li, Y. Liu and J. Leng, Cation distribution dependence of magnetic properties of sol–gel prepared $MnFe_2O_4$ spinel ferrite nanoparticles, *J. Magn. Magn. Mater.*, 2010, **322**, 3396–3400.

31 V. Verma, M. Kaur and S. Sharma, Superoxide dismutase mimic activity of spinel ferrite MFe_2O_4 (M = Mn, Co and Cu) nanoparticles, *Bull. Mater. Sci.*, 2019, **42**, 120–126.

32 D. Makovec, A. Košak, A. Žnidaršič and M. Drofenik, The synthesis of spinel–ferrite nanoparticles using precipitation in microemulsions for ferrofluid applications, *J. Magn. Magn. Mater.*, 2005, **289**, 32–35.

33 S. Maensiri, C. Masingboon, B. Boonchom and S. Seraphin, A simple route to synthesize nickel ferrite ($NiFe_2O_4$) nanoparticles using egg white, *Scr. Mater.*, 2007, **56**, 797–800.

34 M. Madhukara Naik, H. S. Bhojya Naik, G. Nagaraju, M. Vinuth, H. Raja Naika and K. Vinu, Green synthesis of zinc ferrite nanoparticles in Limonia acidissima juice: characterization and their application as photocatalytic and antibacterial activities, *Microchem. J.*, 2019, **146**, 1227–1235.

35 M. Goodarz Naseri, E. B. Saion, H. A. Ahangar, M. Hashim and A. H. Shaari, Synthesis and characterization of manganese ferrite nanoparticles by thermal treatment method, *J. Magn. Magn. Mater.*, 2011, **323**, 1745–1749.

36 M. G. Naseri, E. B. Saion, M. Hashim, A. H. Shaari and H. A. Ahangar, Synthesis and characterization of zinc ferrite nanoparticles by a thermal treatment method, *Solid State Commun.*, 2011, **151**, 1031–1035.

37 H. M. Fan, J. B. Yi, Y. Yang, K. W. Kho, H. R. Tan, Z. X. Shen, J. Ding, X. W. Sun, M. C. Olivo and Y. P. Feng, Single-Crystalline MFe_2O_4 Nanotubes/Nanorings Synthesized by Thermal Transformation Process for Biological Applications, *ACS Nano*, 2009, **3**, 2798–2808.

38 L. Zhen, K. He, C. Y. Xu and W. Z. Shao, Synthesis and characterization of single-crystalline $MnFe_2O_4$ nanorods via a surfactant-free hydrothermal route, *J. Magn. Magn. Mater.*, 2008, **320**, 2672–2675.

39 Sapna, N. Budhiraja, V. Kumar and S. K. Singh, Nanoparticles-assembled $ZnFe_2O_4$ mesoporous nanorods for physicochemical and magnetic properties, *J. Mater. Sci.: Mater. Electron.*, 2019, **30**, 3078–3087.

40 Z. Yang, Z. Zhang, Y. Jiang, M. Chi, G. Nie, X. Lu and C. Wang, Palladium nanoparticles modified electrospun $CoFe_2O_4$ nanotubes with enhanced peroxidase-like activity for colorimetric detection of hydrogen peroxide, *RSC Adv.*, 2016, **6**, 33636–33642.

41 H. Xia, J. Li, L. Ma, Q. Liu and J. Wang, Electrospun porous $CuFe_2O_4$ nanotubes on nickel foam for nonenzymatic voltammetric determination of glucose and hydrogen peroxide, *J. Alloys Compd.*, 2018, **739**, 764–770.

42 J. Wang, G. Yang, L. Wang and W. Yan, Fabrication of one-dimensional $CdFe_2O_4$ yolk/shell flat nanotubes as a high-performance anode for lithium-ion batteries, *J. Mater. Sci.*, 2016, **52**, 4096–4108.

43 Z. Zhang, A. J. Rondinone, J. X. Ma, J. Shen and S. Dai, Morphologically Templated Growth of Aligned Spined $CoFe_2O_4$ Nanorods, *Adv. Mater.*, 2005, **17**, 1415–1419.

44 X. Hou, J. Feng, X. Xu and M. Zhang, Synthesis and characterizations of spinel $MnFe_2O_4$ nanorod by seed–hydrothermal route, *J. Alloys Compd.*, 2010, **491**, 258–263.

45 N. Wang, H. Xu, L. Chen, X. Gu, J. Yang and Y. Qian, A general approach for MFe_2O_4 (M = Zn, Co, Ni) nanorods and their high performance as anode materials for lithium ion batteries, *J. Power Sources*, 2014, **247**, 163–169.

46 N. Labchir, A. Hannour, D. Vincent, A. Ihlal and M. Sajieddine, Magnetic field effect on electrodeposition of $CoFe_2O_4$ nanowires, *Appl. Phys. A*, 2019, **125**, 748–757.

47 F. Li, L. Song, D. Zhou, T. Wang, Y. Wang and H. Wang, Fabrication and magnetic properties of $NiFe_2O_4$ nanocrystalline nanotubes, *J. Mater. Sci.*, 2007, **42**, 7214–7219.

48 Y. Xu, J. Wei, J. Yao, J. Fu and D. Xue, Synthesis of $CoFe_2O_4$ nanotube arrays through an improved sol–gel template approach, *Mater. Lett.*, 2008, **62**, 1403–1405.

49 A. Yourdkhani and G. Caruntu, Highly ordered transition metal ferrite nanotube arrays synthesized by template-assisted liquid phase deposition, *J. Mater. Chem.*, 2011, **21**, 7145.

50 S. Giri, D. Ghosh, A. P. Kharitonov and C. K. Das, Study of Copper Ferrite Nanowire Formation in Presence of Carbon Nanotubes and Influence of Fluorination on High Performance Supercapacitor Energy Storage Application, *Funct. Mater. Lett.*, 2012, **05**, 1250046.

51 C. Pham-Huu, N. Keller, C. Estournes, G. Ehret and M. J. Ledoux, Synthesis of $CoFe_2O_4$ nanowire in carbon nanotubes. A new use of the confinement effect, *Chem. Commun.*, 2002, **17**, 1882–1883.

52 J. Xu, J. Wang, B. Hong, X. Peng, X. Wang, H. Ge and J. Hu, Tailoring magnetic properties with interfacial spins interaction for bundled cobalt ferrites nanowires, *J. Magn. Magn. Mater.*, 2019, **483**, 1–4.

53 S. Menchaca-Nal, C. L. Londono-Calderon, P. Cerrutti, M. L. Foresti, L. Pampillo, V. Bilovol, R. Candal and R. Martinez-Garcia, Facile synthesis of cobalt ferrite nanotubes using bacterial nanocellulose as template, *Carbohydr. Polym.*, 2016, **137**, 726–731.

54 H. Q. Alijani, S. Pourseyedi, M. Torkzadeh-Mahani, A. Seifalian and M. Khatami, Bimetallic nickel ferrite nanorod particles greener synthesis using rosemary and its biomedical efficiency, *Artif. Cells, Nanomed., Biotechnol.*, 2019, **1**, 242–251.

55 X. Cao, L. Gu, X. Lan, C. Zhao, D. Yao and W. Sheng, Spinel $ZnFe_2O_4$ nanoplates embedded with Ag clusters: preparation, characterization, and photocatalytic application, *Mater. Chem. Phys.*, 2007, **106**, 175–180.

56 P. Sivakumar, R. Ramesh, A. Ramanand, S. Ponnusamy and C. Muthamizhchelvan, Synthesis and characterization of $NiFe_2O_4$ nanosheet via polymer assisted co-precipitation method, *Mater. Lett.*, 2011, **65**, 483–485.

57 P. Sivakumar, R. Ramesh, A. Ramanand, S. Ponnusamy and C. Muthamizhchelvan, Synthesis, studies and growth mechanism of ferromagnetic $NiFe_2O_4$ nanosheet, *Appl. Surf. Sci.*, 2012, **258**, 6648–6652.

58 K. Sakthivel, G. Mani, S.-M. Chen, S.-H. Lin, A. Muthumariappan and V. Mani, A novel synthesis of non-aggregated spinel nickel ferrite nanosheets for developing non-enzymatic reactive oxygen species sensor in biological samples, *J. Electroanal. Chem.*, 2018, **820**, 161–167.

59 L. Han, X. Zhou, L. Wan, Y. Deng and S. Zhan, Synthesis of $ZnFe_2O_4$ nanoplates by succinic acid-assisted hydrothermal route and their photocatalytic degradation of rhodamine B under visible light, *J. Environ. Chem. Eng.*, 2014, **2**, 123–130.

60 H. Gao, J. Xiang and Y. Cao, Hierarchically porous $CoFe_2O_4$ nanosheets supported on Ni foam with excellent electrochemical properties for asymmetric supercapacitors, *Appl. Surf. Sci.*, 2017, **413**, 351–359.

61 G. Huang, X. Du, F. Zhang, D. Yin and L. Wang, A Facile Molten-Salt Route for Large-Scale Synthesis of $NiFe_2O_4$ Nanoplates with Enhanced Lithium Storage Capability, *Chem*, 2015, **21**, 14140–14145.

62 L. Peng, P. Xiong, L. Ma, Y. Yuan, Y. Zhu, D. Chen, X. Luo, J. Lu, K. Amine and G. Yu, Holey two-dimensional transition metal oxide nanosheets for efficient energy storage, *Nat. Commun.*, 2017, **8**, 15139.

63 L. Li, S. Liu and L. Lu, Synthesis and significantly enhanced microwave absorption properties of cobalt ferrite hollow microspheres with protrusions/polythiophene composites, *J. Alloys Compd.*, 2017, **722**, 158–165.

64 Y. Meng, D. Chen and X. Jiao, Synthesis and Characterization of $CoFe_2O_4$ Hollow Spheres, *Eur. J. Inorg. Chem.*, 2008, **2008**, 4019–4023.

65 A. Yan, X. Liu, R. Yi, R. Shi, N. Zhang and G. Qiu, Selective Synthesis and Properties of Monodisperse Zn Ferrite Hollow Nanospheres and Nanosheets, *J. Phys. Chem. C*, 2008, **112**, 8558–8563.

66 X. Ni, Z. He, X. Liu, Q. Jiao, H. Li, C. Feng and Y. Zhao, Ionic liquid-assisted solvothermal synthesis of hollow $CoFe_2O_4$ microspheres and their absorbing performances, *Mater. Lett.*, 2017, **193**, 232–235.

67 P. R. Matli, X. Zhou, D. Shiyu and Q. Huang, Fabrication, characterization, and magnetic behavior of porous $ZnFe_2O_4$ hollow microspheres, *Int. Nano Lett.*, 2015, **5**, 53–59.

68 J. Wei, X. Zhang, Q. Liu, Z. Li, L. Liu and J. Wang, Magnetic separation of uranium by $CoFe_2O_4$ hollow spheres, *Chem. Eng. J.*, 2014, **241**, 228–234.

69 S. Briceño, J. Suarez and G. Gonzalez, Solvothermal synthesis of cobalt ferrite hollow spheres with chitosan, *Mater. Sci. Eng., C*, 2017, **78**, 842–846.

70 X. Sun, H. Zhang, L. Zhou, X. Huang and C. Yu, Polypyrrole-Coated Zinc Ferrite Hollow Spheres with Improved Cycling Stability for Lithium-Ion Batteries, *Small*, 2016, **12**, 3732–3737.

71 M. Fu, Q. Jiao, Y. Zhao and H. Li, Vapor diffusion synthesis of $CoFe_2O_4$ hollow sphere/graphene composites as absorbing materials, *J. Mater. Chem. A*, 2014, **2**, 735–744.

72 F. G. D. Silva, J. Depeyrot, A. F. C. Campos, R. Aquino, D. Fiorani and D. Peddis, Structural and Magnetic Properties of Spinel Ferrite Nanoparticles, *J. Nanosci. Nanotechnol.*, 2019, **19**, 4888–4902.

73 Q. Li, C. W. Kartikowati, S. Horie, T. Ogi, T. Iwaki and K. Okuyama, Correlation between particle size/domain structure and magnetic properties of highly crystalline Fe_3O_4 nanoparticles, *Sci. Rep.*, 2017, **7**, 9894.

74 J. Frenkel and J. Doefman, Spontaneous and Induced Magnetisation in Ferromagnetic Bodies, *Nature*, 1930, **126**, 274–275.

75 N. Guijarro, P. Bornoz, M. Prévot, X. Yu, X. Zhu, M. Johnson, X. Jeanbourquin, F. Le Formal and K. Sivula, Evaluating spinel ferrites MFe_2O_4 (M = Cu, Mg, Zn) as photoanodes for solar water oxidation: prospects and limitations, *Sustainable Energy Fuels*, 2018, **2**, 103–117.

76 S. Chandrasekaran, C. Bowen, P. Zhang, Z. Li, Q. Yuan, X. Ren and L. Deng, Spinel photocatalysts for environmental remediation, hydrogen generation, CO_2 reduction and photoelectrochemical water splitting, *J. Mater. Chem. A*, 2018, **6**, 11078–11104.

77 N. Helaïli, Y. Bessekhouad, K. Bachari and M. Trari, Synthesis and physical properties of the $CuFe_{2-x}Mn_xO_4$ ($0 \leq x \leq 2$) solid solution, *Mater. Chem. Phys.*, 2014, **148**, 734–743.

78 A. Kezzim, N. Nasrallah, A. Abdi and M. Trari, Visible light induced hydrogen on the novel hetero-system $CuFe_2O_4$/TiO_2, *Energy Convers. Manage.*, 2011, **52**, 2800–2806.

79 I. Sharifi, H. Shokrollahi and S. Amiri, Ferrite-based magnetic nanofluids used in hyperthermia applications, *J. Magn. Magn. Mater.*, 2012, **324**, 903–915.

80 Ç. E. Demirci Dönmez, P. K. Manna, R. Nickel, S. Aktürk and J. van Lierop, Comparative Heating Efficiency of Cobalt-, Manganese-, and Nickel-Ferrite Nanoparticles for a Hyperthermia Agent in Biomedicines, *ACS Appl. Mater. Interfaces*, 2019, **11**, 6858–6866.

81 Y. Fu, Y. Wan, H. Xia and X. Wang, Nickel ferrite–graphene heteroarchitectures: toward high-performance anode materials for lithium-ion batteries, *J. Power Sources*, 2012, **213**, 338–342.

82 Y. Zhao, X. Li, B. Yan, D. Xiong, D. Li, S. Lawes and X. Sun, Recent Developments and Understanding of Novel Mixed Transition-Metal Oxides as Anodes in Lithium Ion Batteries, *Adv. Energy Mater.*, 2016, **6**, 1502175.

83 L. Yin, Z. Zhang, Z. Li, F. Hao, Q. Li, C. Wang, R. Fan and Y. Qi, Spinel $ZnMn_2O_4$ Nanocrystal-Anchored 3D Hierarchical Carbon Aerogel Hybrids as Anode Materials for Lithium Ion Batteries, *Adv. Funct. Mater.*, 2014, **24**, 4176–4185.

84 B. Joshi, E. Samuel, M.-W. Kim, K. Kim, T.-G. Kim, M. T. Swihart, W. Y. Yoon and S. S. Yoon, Electrosprayed graphene films decorated with bimetallic (zinc-iron) oxide for lithium-ion battery anodes, *J. Alloys Compd.*, 2019, **782**, 699–708.

85 H. Guo, Y. Zhang, A. C. Marschilok, K. J. Takeuchi, E. S. Takeuchi and P. Liu, A first principles study of spinel $ZnFe_2O_4$ for electrode materials in lithium-ion batteries, *Phys. Chem. Chem. Phys.*, 2017, **19**, 26322–26329.

86 Y. Gao, L. Yin, S. J. Kim, H. Yang, I. Jeon, J.-P. Kim, S. Y. Jeong, H. W. Lee and C. R. Cho, Enhanced lithium storage by $ZnFe_2O_4$ nanofibers as anode materials for lithium-ion battery, *Electrochim. Acta*, 2019, **296**, 565–574.

87 R. Alcántara, M. Jaraba, P. Lavela, J. L. Tirado, J. C. Jumas and J. Olivier-Fourcade, Changes in oxidation state and magnetic order of iron atoms during the electrochemical reaction of lithium with $NiFe_2O_4$, *Electrochem. Commun.*, 2003, **5**, 16–21.

88 P. Lavela and J. L. Tirado, $CoFe_2O_4$ and $NiFe_2O_4$ synthesized by sol–gel procedures for their use as anode materials for Li ion batteries, *J. Power Sources*, 2007, **172**, 379–387.

89 Y. Zou, Z. Li, Y. Liu, J. Duan and B. Long, Coaxial structure of $NiFe_2O_4$/CNTs composites as anodes for enhanced lithium ion batteries, *J. Alloys Compd.*, 2020, **820**, 153085.

90 G. Huang, F. Zhang, X. Du, J. Wang, D. Yin and L. Wang, Core-shell $NiFe_2O_4$@TiO_2 nanorods: an anode material with enhanced electrochemical performance for lithium-ion batteries, *Chem*, 2014, **20**, 11214–11219.

91 S. S. Scindia, R. B. Kamble and J. A. Kher, Nickel ferrite/polypyrrole core-shell composite as an efficient electrode material for high-performance supercapacitor, *AIP Adv.*, 2019, **9**, 055218–055226.

92 Y.-Q. Chu, Z.-W. Fu and Q.-Z. Qin, Cobalt ferrite thin films as anode material for lithium ion batteries, *Electrochim. Acta*, 2004, **49**, 4915–4921.

93 H. Qiao, Y. Yu, R. Li, X. Xue and Q. Wei, Facile synthesis of one-dimensional mesoporous cobalt ferrite nanofibers for high lithium storage anode material, *Ionics*, 2018, **25**, 125–132.

94 Y. N. NuLi, Y. Q. Chu and Q. Z. Qin, Nanocrystalline $ZnFe_2O_4$ and Ag-Doped $ZnFe_2O_4$ Films Used as New Anode Materials for Li-Ion Batteries, *J. Electrochem. Soc.*, 2004, **151**, 1077–1083.

95 A. F. S. Abu-Hani, S. T. Mahmoud, F. Awwad and A. I. Ayesh, Design, fabrication, and characterization of portable gas sensors based on spinel ferrite nanoparticles embedded in organic membranes, *Sens. Actuators, B*, 2017, **241**, 1179–1187.

96 M. A. Haija, A. I. Ayesh, S. Ahmed and M. S. Katsiotis, Selective hydrogen gas sensor using $CuFe_2O_4$ nanoparticle based thin film, *Appl. Surf. Sci.*, 2016, **369**, 443–447.

97 M. A. Haija, G. Basina, F. Banat and A. I. Ayesh, Adsorption and gas sensing properties of $CuFe_2O_4$ nanoparticles, *Mater. Sci.-Pol.*, 2019, **37**, 289–295.

98 K. K. Kefeni, T. A. M. Msagati, T. T. Nkambule and B. B. Mamba, Spinel ferrite nanoparticles and nanocomposites for biomedical applications and their toxicity, *Mater. Sci. Eng., C*, 2020, **107**, 110314.

99 B. Peeples, V. Goornavar, C. Peeples, D. Spence, V. Parker, C. Bell, D. Biswal, G. T. Ramesh and A. K. Pradhan, Structural, stability, magnetic, and toxicity studies of nanocrystalline iron oxide and cobalt ferrites for biomedical applications, *J. Nanopart. Res.*, 2014, **16**, 2290.

100 N. Sivakumar, S. R. P. Gnanakan, K. Karthikeyan, S. Amaresh, W. S. Yoon, G. J. Park and Y. S. Lee, Nanostructured $MgFe_2O_4$ as anode materials for lithium-ion batteries, *J. Alloys Compd.*, 2011, **509**, 7038–7041.

101 C. Gong, Y.-J. Bai, Y.-X. Qi, N. Lun and J. Feng, Preparation of carbon-coated $MgFe_2O_4$ with excellent cycling and rate performance, *Electrochim. Acta*, 2013, **90**, 119–127.

102 L. Luo, H. Yang, Z. Bai, D. Tao, S. Zhang, W. Xu, S. Sha and Q. Wei, Polyvinylpyrrolidone-derived carbon-coated magnesium ferrite composite nanofibers as anode material for high-performance lithium-ion batteries, *Ionics*, 2017, **24**, 297–301.

103 D. Bresser, E. Paillard, R. Kloepsch, S. Krueger, M. Fiedler, R. Schmitz, D. Baither, M. Winter and S. Passerini, Carbon Coated $ZnFe_2O_4$ Nanoparticles for Advanced Lithium-Ion Anodes, *Adv. Energy Mater.*, 2013, **3**, 513–523.

104 Y. H. Jin, S. D. Seo, H. W. Shim, K. S. Park and D. W. Kim, Synthesis of core/shell spinel ferrite/carbon nanoparticles with enhanced cycling stability for lithium ion battery anodes, *Nanotechnology*, 2012, **23**, 125402.

105 F. Jiang, X. Du, S. Zhao, J. Guo, B. Huang, X. Huang, Q. Su, J. Zhang and G. Du, Preparation of carbon-coated $MnFe_2O_4$ nanospheres as high-performance anode materials for lithium-ion batteries, *J. Nanopart. Res.*, 2015, **17**, 173.

106 X. Yao, J. Kong, C. Zhao, D. Zhou, R. Zhou and X. Lu, Zinc ferrite nanorods coated with polydopamine-derived carbon for high-rate lithium ion batteries, *Electrochim. Acta*, 2014, **146**, 464–471.

107 R. Q. Bao, Y. R. Zhang, Z. L. Wang, Y. Liu, L. R. Hou and C. Z. Yuan, Core-shell N-doped carbon coated zinc ferrite nanofibers with enhanced Li-storage behaviors: a promising anode for Li-ion batteries, *Mater. Lett.*, 2018, **224**, 89–91.

108 G. Gao, L. Shi, S. Lu, T. Gao, Z. Li, Y. Gao and S. Ding, Ethylene glycol-mediated rapid synthesis of carbon-coated $ZnFe_2O_4$ nanoflakes with long-term and high-rate performance for lithium-ion batteries, *Dalton Trans.*, 2018, **47**, 3521–3529.

109 R. Jin, H. Jiang, Y. Sun, Y. Ma, H. Li and G. Chen, Fabrication of $NiFe_2O_4$/C hollow spheres constructed by mesoporous nanospheres for high-performance lithium-ion batteries, *Chem. Eng. J.*, 2016, **303**, 501–510.

110 T. Zeng, M. Yu, H. Zhang, Z. He, X. Zhang, J. Chen and S. Song, In situ synthesis of cobalt ferrites-embedded hollow N-doped carbon as an outstanding catalyst for elimination of organic pollutants, *Sci. Total Environ.*, 2017, **593**, 286–296.

111 S. Zhang, Z. Qi, Y. Zhao, Q. Jiao, X. Ni, Y. Wang, Y. Chang and C. Ding, Core/shell structured composites of hollow spherical $CoFe_2O_4$ and CNTs as absorbing materials, *J. Alloys Compd.*, 2017, **694**, 309–312.

112 Z. J. Song, W. Ran and F. Y. Wei, One-step approach for the synthesis of $CoFe_2O_4$@rGO core-shell nanocomposites as efficient adsorbent for removal of organic pollutants, *Water Sci. Technol.*, 2017, **75**, 397–405.

113 Y. Huang, Y. Liang, Y. Rao, D. Zhu, J. J. Cao, Z. Shen, W. Ho and S. C. Lee, Environment-Friendly Carbon Quantum Dots/$ZnFe_2O_4$ Photocatalysts: Characterization, Biocompatibility, and Mechanisms for NO Removal, *Environ. Sci. Technol.*, 2017, **51**, 2924–2933.

114 M. Gorgizadeh, N. Azarpira and N. Sattarahmady, In vitro and in vivo tumor annihilation by near-infrared photothermal effect of a $NiFe_2O_4$/C nanocomposite, *Colloids Surf., B*, 2018, **170**, 393–400.

115 G. Wang, Y. Ma, J. Mu, Z. Zhang, X. Zhang, L. Zhang, H. Che, Y. Bai, J. Hou and H. Xie, Monodisperse polyvinylpyrrolidone-coated $CoFe_2O_4$ nanoparticles: synthesis, characterization and cytotoxicity study, *Appl. Surf. Sci.*, 2016, **365**, 114–119.

116 M. Lickmichand, C. S. Shaji, N. Valarmathi, A. S. Benjamin, R. K. A. Kumar, S. Nayak, R. Saraswathy, S. Sumathi and N. A. N. Raj, In vitro biocompatibility and hyperthermia studies on synthesized cobalt ferrite nanoparticles encapsulated with polyethylene glycol for biomedical applications, *Mater. Today: Proc.*, 2019, **15**, 252–261.

117 S. B. Somvanshi, P. B. Kharat, M. V. Khedkar and K. M. Jadhav, Hydrophobic to hydrophilic surface transformation of nano-scale zinc ferrite via oleic acid coating: magnetic hyperthermia study towards biomedical applications, *Ceram. Int.*, 2020, **46**, 7642–7653.

118 X. Sun, X. Zhu, X. Yang, J. Sun, Y. Xia and D. Yang, $CoFe_2O_4$/carbon nanotube aerogels as high performance anodes for lithium ion batteries, *Green Energy Environ.*, 2017, **2**, 160–167.

119 H. Kim, J.-W. Lee, D. Byun and W. Choi, Coaxial-nanostructured $MnFe_2O_4$ nanoparticles on polydopamine-coated MWCNT for anode materials in rechargeable batteries, *Nanoscale*, 2018, **10**, 18949–18960.

120 H. Fu, Z.-j. Du, W. Zou, H.-q. Li and C. Zhang, Simple fabrication of strongly coupled cobalt ferrite/carbon nanotube composite based on deoxygenation for improving lithium storage, *Carbon*, 2013, **65**, 112–123.

121 S. Ren, X. Zhao, R. Chen and M. Fichtner, A facile synthesis of encapsulated $CoFe_2O_4$ into carbon nanofibres and its application as conversion anodes for lithium ion batteries, *J. Power Sources*, 2014, **260**, 205–210.

122 S. Liu, J. Xie, C. Fang, G. Cao, T. Zhu and X. Zhao, Self-assembly of a $CoFe_2O_4$/graphene sandwich by a controllable and general route: towards a high-performance anode for Li-ion batteries, *J. Mater. Chem.*, 2012, **22**, 19738–19743.

123 M. Yu, Z. Feng, Y. Huang, K. Wang and L. Liu, $CoFe_2O_4$ nanoparticles directly grown on carbon nanotube with coralline structure as anodes for lithium ion battery, *J. Mater. Sci.: Mater. Electron.*, 2019, **30**, 4174–4183.

124 D. Narsimulu, B. N. Rao, N. Satyanarayana and E. S. Srinadhu, High Capacity Electrospun $MgFe_2O_4$–C Composite Nanofibers as an Anode Material for Lithium Ion Batteries, *ChemistrySelect*, 2018, **3**, 8010–8017.

125 L. Wang, D. C. Bock, J. Li, E. A. Stach, A. C. Marschilok, K. J. Takeuchi and E. S. Takeuchi, Synthesis and Characterization of $CuFe_2O_4$ Nano/Submicron Wire–Carbon Nanotube Composites as Binder-free Anodes for Li-Ion Batteries, *ACS Appl. Mater. Interfaces*, 2018, **10**, 8770–8785.

126 M. Mujahid, R. Ullah Khan, M. Mumtaz, Mubasher, S. A. Soomro and S. Ullah, $NiFe_2O_4$ nanoparticles/MWCNTs nanohybrid as anode material for lithium-ion battery, *Ceram. Int.*, 2019, **45**, 8486–8493.

127 H. Luan, J. Xu, Z. Tan, A. Zheng and H. Huang, Adsorptive filtration of As(III) from drinking water by $CuFe_2O_4$ particles embedded in carbon nanotube membranes, *J. Chem. Technol. Biotechnol.*, 2019, **94**, 2816–2825.

128 O. A. Oyetade, V. O. Nyamori, B. S. Martincigh and S. B. Jonnalagadda, Effectiveness of carbon nanotube–cobalt ferrite nanocomposites for the adsorption of rhodamine B from aqueous solutions, *RSC Adv.*, 2015, **5**, 22724–22739.

129 X. Li, H. Lu, Y. Zhang and F. He, Efficient removal of organic pollutants from aqueous media using newly synthesized polypyrrole/CNTs-$CoFe_2O_4$ magnetic nanocomposites, *Chem. Eng. J.*, 2017, **316**, 893–902.

130 M. Bahgat, A. A. Farghali, W. M. A. El Rouby and M. H. Khedr, Efficiency, Kinetics and Thermodynamics of Toluidine Blue Dye Removal from Aqueous Solution Using MWCNTs Decorated with $NiFe_2O_4$, *Fullerenes, Nanotubes, Carbon Nanostruct.*, 2014, **22**, 454–470.

131 H. Y. Zhu, R. Jiang, S. H. Huang, J. Yao, F. Q. Fu and J. B. Li, Novel magnetic $NiFe_2O_4$/multi-walled carbon nanotubes hybrids: facile synthesis, characterization, and application to the treatment of dyeing wastewater, *Ceram. Int.*, 2015, **41**, 11625–11631.

132 L. Zhou, L. Ji, P. C. Ma, Y. Shao, H. Zhang, W. Gao and Y. Li, Development of carbon nanotubes/$CoFe_2O_4$ magnetic hybrid material for removal of tetrabromobisphenol A and Pb(II), *J. Hazard. Mater.*, 2014, **265**, 104–114.

133 F. Wang, W. Sun, W. Pan and N. Xu, Adsorption of sulfamethoxazole and 17β-estradiol by carbon nanotubes/$CoFe_2O_4$ composites, *Chem. Eng. J.*, 2015, **274**, 17–29.

134 M. Nawaz, A. Shahzad, K. Tahir, J. Kim, M. Moztahida, J. Jang, M. B. Alam, S.-H. Lee, H.-Y. Jung and D. S. Lee, Photo-Fenton reaction for the degradation of sulfamethoxazole using a multi-walled carbon nanotube-$NiFe_2O_4$ composite, *Chem. Eng. J.*, 2020, **382**, 123053.

135 P. Xiong, Y. Fu, L. Wang and X. Wang, Multi-walled carbon nanotubes supported nickel ferrite: a magnetically recyclable photocatalyst with high photocatalytic activity on degradation of phenols, *Chem. Eng. J.*, 2012, **195**, 149–157.

136 A. A. Ensafi, A. R. Allafchian, B. Rezaei and R. Mohammadzadeh, Characterization of carbon nanotubes decorated with $NiFe_2O_4$ magnetic nanoparticles as a novel electrochemical sensor: application for highly selective determination of sotalol using voltammetry, *Mater. Sci. Eng., C*, 2013, **33**, 202–208.

137 D. M. Fernandes, N. Silva, C. Pereira, C. Moura, J. M. C. S. Magalhães, B. Bachiller-Baeza, I. Rodríguez-Ramos, A. Guerrero-Ruiz, C. Delerue-Matos and C. Freire, $MnFe_2O_4$@CNT-N as novel electrochemical nanosensor

for determination of caffeine, acetaminophen and ascorbic acid, *Sens. Actuators, B*, 2015, **218**, 128–136.

138 R. Hajihashemi, A. M. Rashidi, M. Alaie, R. Mohammadzadeh and N. Izadi, The study of structural properties of carbon nanotubes decorated with $NiFe_2O_4$ nanoparticles and application of nano-composite thin film as H_2S gas sensor, *Mater. Sci. Eng., C*, 2014, **44**, 417–421.

139 S. L. Darshane, S. S. Suryavanshi and I. S. Mulla, Nanostructured nickel ferrite: a liquid petroleum gas sensor, *Ceram. Int.*, 2009, **35**, 1793–1797.

140 P. Norouzi, M. R. Ganjali, A. S. Emami Meibodi and B. Larijani, Sotalol nanolevel detection at an Au microelectrode in flowing solutions, *Russ. J. Electrochem.*, 2008, **44**, 1024.

141 M. E. Ghica and C. M. A. Brett, Simple and Efficient Epinephrine Sensor Based on Carbon Nanotube Modified Carbon Film Electrodes, *Anal. Lett.*, 2013, **46**, 1379–1393.

142 A. A. Ensafi, F. Saeid, B. Rezaei and A. R. Allafchian, $NiFe_2O_4$ nanoparticles decorated with MWCNTs as a selective and sensitive electrochemical sensor for the determination of epinephrine using differential pulse voltammetry, *Anal. Methods*, 2014, **6**, 6885–6892.

143 F. Cui and X. Zhang, Electrochemical sensor for epinephrine based on a glassy carbon electrode modified with graphene/gold nanocomposites, *J. Electroanal. Chem.*, 2012, **669**, 35–41.

144 M. Amoli-Diva and K. Pourghazi, $CoFe_2O_4$ nanoparticles grafted multi-walled carbon nanotubes coupled with surfactant-enhanced spectrofluorimetry for determination of ofloxacin in human plasma, *Nanochem. Res.*, 2018, **3**, 17–23.

145 M. Hassannezhad, M. Hosseini, M. R. Ganjali and M. Arvand, Electrochemical Sensor Based on Carbon Nanotubes Decorated with $ZnFe_2O_4$ Nanoparticles Incorporated Carbon Paste Electrode for Determination of Metoclopramide and Indomethacin, *ChemistrySelect*, 2019, **4**, 7616–7626.

146 H. Fan, X. Xing, Y. Yang, B. Li, C. Wang and D. Qiu, Triple function nanocomposites of porous silica-$CoFe_2O_4$-MWCNTs as a carrier for pH-sensitive anti-cancer drug controlled delivery, *Dalton Trans.*, 2017, **46**, 14831–14838.

147 C. Sun, Y. Liu, W. Ding, Y. Gou, K. Xu, G. Xia and Q. Ding, Synthesis and characterization of superparamagnetic $CoFe_2O_4$/MWCNT hybrids for tumor-targeted therapy, *J. Nanosci. Nanotechnol.*, 2013, **13**, 236–241.

148 M. Tiwaree, P. Seal, J. P. Borah and N. Paul, Functionalization of Carbon Nanotubes and its Nanocomposites for Hyperthermia studies, *Mater. Today: Proc.*, 2019, **18**, 1317–1323.

149 P. Seal, M. Hazarika, N. Paul and J. P. Borah, MWCNT-$MnFe_2O_4$ nanocomposite for efficient hyperthermia applications, *AIP Conf. Proc.*, 2018, **1942**, 050083.

150 M. K. Aslam, S. S. A. Shah, T. Najam, S. Li and C. Chen, Decoration of cobalt/iron oxide nanoparticles on N-doped carbon nanosheets: electrochemical performances for lithium-ion batteries, *J. Appl. Electrochem.*, 2019, **49**, 433–442.

151 S. Li, B. Wang, J. Liu and M. Yu, In situ one-step synthesis of $CoFe_2O_4$/graphene nanocomposites as high-performance anode for lithium-ion batteries, *Electrochim. Acta*, 2014, **129**, 33–39.

152 S. Li, B. Wang, B. Li, J. Liu, M. Yu and X. Wu, Self-assembly of 2D sandwich-structured $MnFe_2O_4$/graphene composites for high-performance lithium storage, *Mater. Res. Bull.*, 2015, **61**, 369–374.

153 K. Wu, G. Hu, Y. Cao, Z. Peng and K. Du, Facile and green synthesis of $MnFe_2O_4$/reduced graphene oxide nanocomposite as anode materials for Li-ion batteries, *Mater. Lett.*, 2015, **161**, 178–180.

154 P. Kollu, P. R. Kumar, C. Santosh, D. K. Kim and A. N. Grace, A high capacity $MnFe_2O_4$/rGO nanocomposite for Li and Na-ion battery applications, *RSC Adv.*, 2015, **5**, 63304–63310.

155 B. Wang, S. Li, J. Liu, M. Yu, B. Li and X. Wu, An efficient route to a hierarchical $CoFe_2O_4$ @graphene hybrid films with superior cycling stability and rate capability for lithium storage, *Electrochim. Acta*, 2014, **146**, 679–687.

156 B. Wang, S. Li, B. Li, J. Liu and M. Yu, Facile and large-scale fabrication of hierarchical $ZnFe_2O_4$/graphene hybrid films as advanced binder-free anodes for lithium-ion batteries, *New J. Chem.*, 2015, **39**, 1725–1733.

157 E. K. Heidari, B. Zhang, M. H. Sohi, A. Ataie and J.-K. Kim, Sandwich-structured graphene–$NiFe_2O_4$–carbon nanocomposite anodes with exceptional electrochemical performance for Li ion batteries, *J. Mater. Chem. A*, 2014, **2**, 8314.

158 C. Li, X. Wang, S. Li, Q. Li, J. Xu, X. Liu, C. Liu, Y. Xu, J. Liu, H. Li, P. Guo and X. S. Zhao, Optimization of $NiFe_2O_4$/rGO composite electrode for lithium-ion batteries, *Appl. Surf. Sci.*, 2017, **416**, 308–317.

159 B. Dong, M. Li, C. Xiao, D. Ding, G. Gao and S. Ding, Tunable growth of perpendicular cobalt ferrite nanosheets on reduced graphene oxide for energy storage, *Nanotechnology*, 2016, **28**, 055401.

160 J. Wang, Q. Deng, M. Li, K. Jiang, J. Zhang, Z. Hu and J. Chu, Copper ferrites@reduced graphene oxide anode materials for advanced lithium storage applications, *Sci. Rep.*, 2017, **7**, 8903.

161 B. Mandal, J. Panda, P. K. Paul, R. Sarkar and B. Tudu, $MnFe_2O_4$ decorated reduced graphene oxide heterostructures: nanophotocatalyst for methylene blue dye degradation, *Vacuum*, 2020, **173**, 109150.

162 A. Alazmi, V. Singaravelu, N. M. Batra, J. Smajic, M. Alyami, N. M. Khashab and P. M. F. J. Costa, Cobalt ferrite supported on reduced graphene oxide as a T_2 contrast agent for magnetic resonance imaging, *RSC Adv.*, 2019, **9**, 6299–6309.

163 M. Israr, J. Iqbal, A. Arshad, S. O. Aisida and I. Ahmad, A unique $ZnFe_2O_4$/graphene nanoplatelets nanocomposite for electrochemical energy storage and efficient visible light driven catalysis for the degradation of organic

noxious in wastewater, *J. Phys. Chem. Solids*, 2020, **140**, 109333.

164 M. L. Baynosa, A. H. Mady, V. Q. Nguyen, D. R. Kumar, M. S. Sayed, D. Tuma and J. J. Shim, Eco-friendly synthesis of recyclable mesoporous zinc ferrite@reduced graphene oxide nanocomposite for efficient photocatalytic dye degradation under solar radiation, *J. Colloid Interface Sci.*, 2020, **561**, 459–469.

165 Y. Yao, Y. Cai, F. Lu, F. Wei, X. Wang and S. Wang, Magnetic recoverable $MnFe_2O_4$ and $MnFe_2O_4$-graphene hybrid as heterogeneous catalysts of peroxymonosulfate activation for efficient degradation of aqueous organic pollutants, *J. Hazard. Mater.*, 2014, **270**, 61–70.

166 N. Ueda Yamaguchi, R. Bergamasco and S. Hamoudi, Magnetic $MnFe_2O_4$–graphene hybrid composite for efficient removal of glyphosate from water, *Chem. Eng. J.*, 2016, **295**, 391–402.

167 A. Meidanchi and O. Akhavan, Superparamagnetic zinc ferrite spinel–graphene nanostructures for fast wastewater purification, *Carbon*, 2014, **69**, 230–238.

168 L. S. K. Achary, A. Kumar, B. Barik, P. S. Nayak, N. Tripathy, J. P. Kar and P. Dash, Reduced graphene oxide-$CuFe_2O_4$ nanocomposite: a highly sensitive room temperature NH_3 gas sensor, *Sens. Actuators, B*, 2018, **272**, 100–109.

169 G. Wang, Y. Ma, L. Zhang, J. Mu, Z. Zhang, X. Zhang, H. Che, Y. Bai and J. Hou, Facile synthesis of manganese ferrite/graphene oxide nanocomposites for controlled targeted drug delivery, *J. Magn. Magn. Mater.*, 2016, **401**, 647–650.

170 Y. Yang, H. Shi, Y. Wang, B. Shi, L. Guo, D. Wu, S. Yang and H. Wu, Graphene oxide/manganese ferrite nanohybrids for magnetic resonance imaging, photothermal therapy and drug delivery, *J. Biomater. Appl.*, 2016, **30**, 810–822.

171 N. Venkatesha, P. Poojar, R. Ashwini, Y. Qurishi, S. Geethanath and C. Srivastava, Ultrafine graphene oxide–$CoFe_2O_4$ nanoparticle composite as T_1 and T_2 contrast agent for magnetic resonance imaging, *RSC Adv.*, 2016, **6**, 17423–17429.

172 E. Peng, E. S. Choo, P. Chandrasekharan, C. T. Yang, J. Ding, K. H. Chuang and J. M. Xue, Synthesis of manganese ferrite/graphene oxide nanocomposites for biomedical applications, *Small*, 2012, **8**, 3620–3630.

173 M. Wu, Y. Yang, K. Cao, C. Zhao, X. Qiao and C. Hong, Microwave-assisted preparation of $ZnFe_2O_4$-Ag/rGO nanocomposites for amplification signal detection of alpha-fetoprotein, *Bioelectrochemistry*, 2020, **132**, 107434.

174 W. Liu, H. Yang, C. Ma, Y.-n. Ding, S. Ge, J. Yu and M. Yan, Graphene–palladium nanowires based electrochemical sensor using $ZnFe_2O_4$–graphene quantum dots as an effective peroxidase mimic, *Anal. Chim. Acta*, 2014, **852**, 181–188.

175 A. A. Ensafi, H. A. Alinajafi, M. Jafari-Asl, B. Rezaei and F. Ghazaei, Cobalt ferrite nanoparticles decorated on exfoliated graphene oxide, application for amperometric determination of NADH and H_2O_2, *Mater. Sci. Eng., C*, 2016, **60**, 276–284.

176 A. Shokri, S. F. Shayesteh and K. Boustani, The role of Co ion substitution in $SnFe_2O_4$ spinel ferrite nanoparticles: study of structural, vibrational, magnetic and optical properties, *Ceram. Int.*, 2018, **44**, 22092–22101.

177 X. Tang, X. Hou, L. Yao, S. Hu, X. Liu and L. Xiang, Mn-doped $ZnFe_2O_4$ nanoparticles with enhanced performances as anode materials for lithium ion batteries, *Mater. Res. Bull.*, 2014, **57**, 127–134.

178 J. Mao, X. Hou, F. Huang, K. Shen, K.-h. Lam, Q. Ru and S. Hu, Zn substitution $NiFe_2O_4$ nanoparticles with enhanced conductivity as high-performances electrodes for lithium ion batteries, *J. Alloys Compd.*, 2016, **676**, 265–274.

179 I. Quinzeni, V. Berbenni, D. Capsoni and M. Bini, Ca- and Al-doped $ZnFe_2O_4$ nanoparticles as possible anode materials, *J. Solid State Electrochem.*, 2018, **22**, 2013–2024.

180 B. Bashir, W. Shaheen, M. Asghar, M. F. Warsi, M. A. Khan, S. Haider, I. Shakir and M. Shahid, Copper doped manganese ferrites nanoparticles anchored on graphene nano-sheets for high performance energy storage applications, *J. Alloys Compd.*, 2017, **695**, 881–887.

181 R. Indhrajothi, I. Prakash, M. Venkateswarlu and N. Satyanarayana, Lanthanum ion (La^{3+}) substituted $CoFe_2O_4$ anode material for lithium ion battery applications, *New J. Chem.*, 2015, **39**, 4601–4610.

182 D. Narsimulu, B. N. Rao, G. Nagaraju, J. S. Yu and N. Satyanarayana, Enhanced energy storage performance of nanocrystalline Sm-doped $CoFe_2O_4$ as an effective anode material for Li-ion battery applications, *J. Solid State Electrochem.*, 2020, **24**, 225–236.

183 L. Lv, Y. Wang, P. Cheng, B. Zhang, F. Dang and L. Xu, Ultrasonic spray pyrolysis synthesis of three-dimensional $ZnFe_2O_4$-based macroporous spheres for excellent sensitive acetone gas sensor, *Sens. Actuators, B*, 2019, **297**, 126755.

184 C. Zhao, W. Lan, H. Gong, J. Bai, R. Ramachandran, S. Liu and F. Wang, Highly sensitive acetone-sensing properties of Pt-decorated $CuFe_2O_4$ nanotubes prepared by electrospinning, *Ceram. Int.*, 2018, **44**, 2856–2863.

185 M. S. Khandekar, N. L. Tarwal, I. S. Mulla and S. S. Suryavanshi, Nanocrystalline Ce doped $CoFe_2O_4$ as an acetone gas sensor, *Ceram. Int.*, 2014, **40**, 447–452.

186 A. Bhardwaj, A. Kumar, U. Sim, H.-N. Im and S.-J. Song, Synergistic enhancement in the sensing performance of a mixed-potential NH_3 sensor using SnO_2@$CuFe_2O_4$ sensing electrode, *Sens. Actuators, B*, 2020, **308**, 127748.

187 F. R. Mariosi, J. Venturini, A. da Cas Viegas and C. P. Bergmann, Lanthanum-doped spinel cobalt ferrite ($CoFe_2O_4$) nanoparticles for environmental applications, *Ceram. Int.*, 2020, **46**, 2772–2779.

188 E. Ranjith Kumar, R. Jayaprakash, G. Sarala Devi and P. Siva Prasada Reddy, Synthesis of Mn substituted $CuFe_2O_4$ nanoparticles for liquefied petroleum gas sensor applications, *Sens. Actuators, B*, 2014, **191**, 186–191.

189 V. Manikandan, M. Singh, B. C. Yadav, R. S. Mane, S. Vigneselvan, A. Mirzaei and J. Chandrasekaran, Room temperature LPG sensing properties of tin substituted

copper ferrite (Sn–$CuFe_2O_4$) thin film, *Mater. Chem. Phys.*, 2020, **240**, 122265.

190 R. Dou, H. Cheng, J. Ma and S. Komarneni, Manganese doped magnetic cobalt ferrite nanoparticles for dye degradation via a novel heterogeneous chemical catalysis, *Mater. Chem. Phys.*, 2020, **240**, 122181.

191 A. G. Abraham, A. Manikandan, E. Manikandan, S. Vadivel, S. K. Jaganathan, A. Baykal and P. S. Renganathan, Enhanced magneto-optical and photo-catalytic properties of transition metal cobalt (Co^{2+} ions) doped spinel $MgFe_2O_4$ ferrite nanocomposites, *J. Magn. Magn. Mater.*, 2018, **452**, 380–388.

192 N. Sanpo, J. Wang and C. C. Berndt, Sol-Gel Synthesized Copper-Substituted Cobalt Ferrite Nanoparticles for Biomedical Applications, *J. Nano Res.*, 2013, **25**, 110–121.

193 N. Sanpo, C. C. Berndt, C. Wen and J. Wang, Transition metal-substituted cobalt ferrite nanoparticles for biomedical applications, *Acta Biomater.*, 2013, **9**, 5830–5837.

194 K. Elayakumar, A. Manikandan, A. Dinesh, K. Thanrasu, K. Kanmani Raja, R. Thilak Kumar, Y. Slimani, S. K. Jaganathan and A. Baykal, Enhanced magnetic property and antibacterial biomedical activity of Ce^{3+} doped $CuFe_2O_4$ spinel nanoparticles synthesized by sol-gel method, *J. Magn. Magn. Mater.*, 2019, **478**, 140–147.

195 S. Velho-Pereira, A. Noronha, A. Mathias, R. Zakane, V. Naik, P. Naik, A. V. Salker and S. R. Naik, Antibacterial action of doped $CoFe_2O_4$ nanocrystals on multidrug resistant bacterial strains, *Mater. Sci. Eng., C*, 2015, **52**, 282–287.

196 A. Apostolov, I. Apostolova and J. Wesselinowa, Specific absorption rate in Zn-doted ferrites for self-controlled magnetic hyperthermia, *Eur. Phys. J. B*, 2019, **92**, 58.

197 R. D. Raland and J. P. Borah, Efficacy of heat generation in CTAB coated Mn doped $ZnFe_2O_4$ nanoparticles for magnetic hyperthermia, *J. Phys. D: Appl. Phys.*, 2016, **50**, 035001.

198 R. Arulmurugan, G. Vaidyanathan, S. Sendhilnathan and B. Jeyadevan, Mn–Zn ferrite nanoparticles for ferrofluid preparation: study on thermal–magnetic properties, *J. Magn. Magn. Mater.*, 2006, **298**, 83–94.

199 Z. Beji, A. Hanini, L. S. Smiri, J. Gavard, K. Kacem, F. Villain, J. M. Grenèche, F. Chau and S. Ammar, Magnetic properties of Zn-substituted $MnFe_2O_4$ nanoparticles synthesized in polyol as potential heating agents for hyperthermia. Evaluation of their toxicity on Endothelial cells, *Chem. Mater.*, 2010, **22**, 5420–5429.

200 N. A. Alghamdi, J. H. Hankiewicz, N. R. Anderson, K. F. Stupic, R. E. Camley, M. Przybylski, J. Żukrowski and Z. Celinski, Development of Ferrite-Based Temperature Sensors for Magnetic Resonance Imaging: A Study of $Cu_{1-x}Zn_xFe_2O_4$, *Phys. Rev. Appl.*, 2018, **9**, 054030.

201 Z. Ghasemian, D. Shahbazi-Gahrouei and S. Manouchehri, Cobalt Zinc Ferrite Nanoparticles as a Potential Magnetic Resonance Imaging Agent: An In vitro Study, *Avicenna J. Med. Biotechnol.*, 2015, **7**, 64–68.

202 G. Huang, F. Zhang, L. Zhang, X. Du, J. Wang and L. Wang, Hierarchical $NiFe_2O_4/Fe_2O_3$ nanotubes derived from metal organic frameworks for superior lithium ion battery anodes, *J. Mater. Chem. A*, 2014, **2**, 8048–8053.

203 P. Liu, W. Lei, X. Xia and Q. Hao, Novel Heterogeneous Hybrid of Yolk–Shell CuO@$CuFe_2O_4$: Facile Synthesis and Enhanced Lithium-Storage Performance, *ChemElectroChem*, 2017, **4**, 2068–2074.

204 W. Lu, J. Wang, L. Zhao, C. Hu, X. Zhang and L. Duan, The double synergies of core-shell $MnFe_2O_4$@TiO_2 mesoporous spheres for enhancing electrochemical performance of anode material as lithium-ion batteries, *Mater. Sci. Eng., B*, 2019, **242**, 17–22.

205 G. Qin, X. Wu, J. Wen, J. Li and M. Zeng, A Core-Shell $NiFe_2O_4$@SiO_2 Structure as a High Performance Anode Material for Lithium-Ion Batteries, *ChemElectroChem*, 2019, **6**, 911–916.

206 Z. Xue, L. Li, L. Cao, W. Zheng, W. Yang and X. Yu, A simple method to fabricate $NiFe_2O_4$/NiO@Fe_2O_3 core-shelled nanocubes based on Prussian blue analogues for lithium ion battery, *J. Alloys Compd.*, 2020, **825**, 153966.

207 H. Gao, S. Cao and Y. Cao, Hierarchical Core-Shell Nanosheet Arrays with MnO_2 Grown on Mesoporous $CoFe_2O_4$ Support for High-Performance Asymmetric Supercapacitors, *Electrochim. Acta*, 2017, **240**, 31–42.

208 C. Liu, T. Peng, C. Wang, Y. Lu, H. Yan and Y. Luo, Three-dimensional $ZnFe_2O_4$@MnO_2 hierarchical core/shell nanosheet arrays as high-performance battery-type electrode materials, *J. Alloys Compd.*, 2017, **720**, 86–94.

209 X. W. Hu, S. Liu, B. T. Qu and X. Z. You, Starfish-shaped $Co_3O_4/ZnFe_2O_4$ Hollow Nanocomposite: Synthesis, Supercapacity, and Magnetic Properties, *ACS Appl. Mater. Interfaces*, 2015, **7**, 9972–9981.

210 X. Yang, H. Xue, Q. Yang, R. Yuan, W. Kang and C.-S. Lee, Preparation of porous ZnO/$ZnFe_2O_4$ composite from metal organic frameworks and its applications for lithium ion batteries, *Chem. Eng. J.*, 2017, **308**, 340–346.

211 S. Balaji, R. Vasuki and D. Mutharasu, A feasibility study on $SnO_2/NiFe_2O_4$ nanocomposites as anodes for Li ion batteries, *J. Alloys Compd.*, 2013, **554**, 25–31.

212 K. Ali, J. Iqbal, T. Jan, I. Ahmad, D. Wan and I. Ahmad, Influence of NiO concentration on structural, dielectric and magnetic properties of core/shell $CuFe_2O_4$/NiO nanocomposites, *Mater. Chem. Phys.*, 2017, **195**, 283–294.

213 A. K. Rai, J. Gim, T. V. Thi, D. Ahn, S. J. Cho and J. Kim, High Rate Capability and Long Cycle Stability of Co_3O_4/$CoFe_2O_4$ Nanocomposite as an Anode Material for High-Performance Secondary Lithium Ion Batteries, *J. Phys. Chem. C*, 2014, **118**, 11234–11243.

214 Z. Wang, X. Zhang, X. Liu, W. Zhang, Y. Zhang, Y. Li, C. Qin, W. Zhao and Z. Bakenov, Dual-network nanoporous $NiFe_2O_4$/NiO composites for high performance Li-ion battery anodes, *Chem. Eng. J.*, 2020, **388**, 124207.

215 F. Talebzadeh, R. Zandipak and S. Sobhanardakani, CeO_2 nanoparticles supported on $CuFe_2O_4$ nanofibers as novel adsorbent for removal of Pb(II), Ni(II), and V(V) ions from

petrochemical wastewater, *Desalin. Water Treat.*, 2016, **57**, 28363–28377.

216 A. Paul and S. S. Dhar, Construction of hierarchical $MnMoO_4/NiFe_2O_4$ nanocomposite: highly efficient visible light driven photocatalyst in the degradation of different polluting dyes in aqueous medium, *Colloids Surf., A*, 2020, **585**, 124090.

217 Y. Du, W. Ma, P. Liu, B. Zou and J. Ma, Magnetic $CoFe_2O_4$ nanoparticles supported on titanate nanotubes ($CoFe_2O_4$/TNTs) as a novel heterogeneous catalyst for peroxymonosulfate activation and degradation of organic pollutants, *J. Hazard. Mater.*, 2016, **308**, 58–66.

218 Y.-F. Huang, X.-Y. Sun, S.-H. Huo, Y. Li and C. Zhong, Core-shell dual-MOF heterostructures derived magnetic $CoFe_2O_4$/CuO (sub)microcages with superior catalytic performance, *Appl. Surf. Sci.*, 2019, **466**, 637–646.

219 F. Siadatnasab, S. Farhadi and A. Khataee, Sonocatalytic performance of magnetically separable $CuS/CoFe_2O_4$ nanohybrid for efficient degradation of organic dyes, *Ultrason. Sonochem.*, 2018, **44**, 359–367.

220 S. Farhadi, F. Siadatnasab and A. Khataee, Ultrasound-assisted degradation of organic dyes over magnetic $CoFe_2O_4$@ZnS core-shell nanocomposite, *Ultrason. Sonochem.*, 2017, **37**, 298–309.

221 J. Huang, H.-x. Jing, N. Li, L.-x. Li and W.-z. Jiao, Fabrication of magnetically recyclable SnO_2-$TiO_2/CoFe_2O_4$ hollow core-shell photocatalyst: improving photocatalytic efficiency under visible light irradiation, *J. Solid State Chem.*, 2019, **271**, 103–109.

222 A. Wilson, S. R. Mishra, R. Gupta and K. Ghosh, Preparation and photocatalytic properties of hybrid core–shell reusable $CoFe_2O_4$–ZnO nanospheres, *J. Magn. Magn. Mater.*, 2012, **324**, 2597–2601.

223 C. Borgohain, K. K. Senapati, K. C. Sarma and P. Phukan, A facile synthesis of nanocrystalline $CoFe_2O_4$ embedded one-dimensional ZnO hetero-structure and its use in photocatalysis, *J. Mol. Catal. A: Chem.*, 2012, **363**, 495–500.

224 Q. Ma, H. Zhang, X. Zhang, B. Li, R. Guo, Q. Cheng and X. Cheng, Synthesis of magnetic $CuO/MnFe_2O_4$ nanocompisite and its high activity for degradation of levofloxacin by activation of persulfate, *Chem. Eng. J.*, 2019, **360**, 848–860.

225 A. Zamani, M. S. Sadjadi, A. Mahjoub, M. Yousefi and N. Farhadyar, Synthesis and characterization $ZnFe_2O_4$@MnO and $MnFe_2O_4$@ZnO magnetic nanocomposites: investigation of photocatalytic activity for the degradation of Congo Red under visible light irradiation, *Int. J. Nano Dimens.*, 2020, **11**, 58–73.

226 Z. Wang, J. Wang, Y. Pan, F. Liu, Y. Lai, J. Li and L. Jiang, Preparation and characterization of a novel and recyclable $InVO_4/ZnFe_2O_4$ composite for methylene blue removal by adsorption and visible-light photocatalytic degradation, *Appl. Surf. Sci.*, 2020, **501**, 144006.

227 H.-Y. Zhu, R. Jiang, Y.-Q. Fu, R.-R. Li, J. Yao and S.-T. Jiang, Novel multifunctional $NiFe_2O_4$/ZnO hybrids for dye removal by adsorption, photocatalysis and magnetic separation, *Appl. Surf. Sci.*, 2016, **369**, 1–10.

228 A. I. Borhan, D. Gherca, Ş. Cojocaru, N. Lupu, T. Roman, M. Zaharia, M. N. Palamaru and A. R. Iordan, One-pot synthesis of hierarchical magnetic porous γ-Fe_2O_3@$NiFe_2O_4$ composite with solid-phase morphology changes promoted by adsorption of anionic azo-dye, *Mater. Res. Bull.*, 2020, **122**, 110664.

229 H. Zhang, B. Xia, P. Wang, Y. Wang, Z. Li, Y. Wang, L. Feng, X. Li and S. Du, From waste to waste treatment: mesoporous magnetic $NiFe_2O_4$/ZnCuCr-layered double hydroxide composite for wastewater treatment, *J. Alloys Compd.*, 2020, **819**, 153053.

230 L. Lu, J. Li, J. Yu, P. Song and D. H. L. Ng, A hierarchically porous $MgFe_2O_4$/γ-Fe_2O_3 magnetic microspheres for efficient removals of dye and pharmaceutical from water, *Chem. Eng. J.*, 2016, **283**, 524–534.

231 X. Wang, Z. Zhang, Y. Zhao, K. Xia, Y. Guo, Z. Qu and R. Bai, A Mild and Facile Synthesis of Amino Functionalized $CoFe_2O_4$@SiO_2 for Hg(II) Removal, *Nanomaterials*, 2018, **8**, 673.

232 X. Li, C. Wang, H. Guo, P. Sun, F. Liu, X. Liang and G. Lu, Double-Shell Architectures of $ZnFe_2O_4$ Nanosheets on ZnO Hollow Spheres for High-Performance Gas Sensors, *ACS Appl. Mater. Interfaces*, 2015, **7**, 17811–17818.

233 X. Li, D. Lu, C. Shao, G. Lu, X. Li and Y. Liu, Hollow $CuFe_2O_4$/α-Fe_2O_3 composite with ultrathin porous shell for acetone detection at ppb levels, *Sens. Actuators, B*, 2018, **258**, 436–446.

234 G. Lin, H. Wang, X. Li, X. Lai, Y. Zou, X. Zhou, D. Liu, J. Wan and H. Xin, Chestnut-like $CoFe_2O_4$@SiO_2@In_2O_3 nanocomposite microspheres with enhanced acetone sensing property, *Sens. Actuators, B*, 2018, **255**, 3364–3373.

235 X. Hu, Z. Zhu, Z. Li, L. Xie, Y. Wu and L. Zheng, Heterostructure of CuO microspheres modified with $CuFe_2O_4$ nanoparticles for highly sensitive H_2S gas sensor, *Sens. Actuators, B*, 2018, **264**, 139–149.

236 A. S. Kamzin, H. Das, N. Wakiya and A. A. Valiullin, Magnetic Core/Shell Nanocomposites $MgFe_2O_4/SiO_2$ for Biomedical Application: Synthesis and Properties, *Phys. Solid State*, 2018, **60**, 1752–1761.

237 J. Singh, M. Srivastava, P. Kalita and B. D. Malhotra, A novel ternary $NiFe_2O_4$/CuO/FeO-chitosan nanocomposite as a cholesterol biosensor, *Process Biochem.*, 2012, **47**, 2189–2198.

238 Z. Rashid, M. Soleimani, R. Ghahremanzadeh, M. Vossoughi and E. Esmaeili, Effective surface modification of $MnFe_2O_4$@SiO_2@PMIDA magnetic nanoparticles for rapid and high-density antibody immobilization, *Appl. Surf. Sci.*, 2017, **426**, 1023–1029.

239 S. Karmakar, K. L. Routray, B. Panda, B. Sahoo and D. Behera, Construction of core@shell nanostructured $NiFe_2O_4$@TiO_2 ferrite NAND logic gate using fluorescence quenching mechanism for TiO_2 sensing, *J. Alloys Compd.*, 2018, **765**, 527–537.

240 H. Gupta, P. Paul and N. Kumar, Synthesis and Characterization of DHA/ZnO/$ZnFe_2O_4$ Nanostructures for Biomedical Imaging Application, *Procedia Mater. Sci.*, 2014, **5**, 198–203.

241 L. Jiang, W. Gao, B. Jin, H. Li, S. Li, G. Zhu and Q. Jiang, $ZnFe_2O_4/MoS_2$/rGO composite as an anode for rechargeable Lithium-ion batteries, *J. Electroanal. Chem.*, 2018, **823**, 407–415.

242 P. M. Ette, A. Chithambararaj, A. S. Prakash and K. Ramesha, MoS_2 Nanoflower-Derived Interconnected $CoMoO_4$ Nanoarchitectures as a Stable and High Rate Performing Anode for Lithium-Ion Battery Applications, *ACS Appl. Mater. Interfaces*, 2020, **12**, 11511–11521.

243 S. Wen, Y. Liu, F. Zhu, R. Shao and W. Xu, Hierarchical MoS_2 nanowires/$NiCo_2O_4$ nanosheets supported on Ni foam for high-performance asymmetric supercapacitors, *Appl. Surf. Sci.*, 2018, **428**, 616–622.

244 Y. Zhao, L. Xu, J. Yan, W. Yan, C. Wu, J. Lian, Y. Huang, J. Bao, J. Qiu, L. Xu, Y. Xu, H. Xu and H. Li, Facile preparation of $NiFe_2O_4/MoS_2$ composite material with synergistic effect for high performance supercapacitor, *J. Alloys Compd.*, 2017, **726**, 608–617.

245 Y. Ding, Y. Yang and H. Shao, High capacity $ZnFe_2O_4$ anode material for lithium ion batteries, *Electrochim. Acta*, 2011, **56**, 9433–9438.

246 Y. Deng, Q. Zhang, S. Tang, L. Zhang, S. Deng, Z. Shi and G. Chen, One-pot synthesis of $ZnFe_2O_4$/C hollow spheres as superior anode materials for lithium ion batteries, *Chem. Commun.*, 2011, **47**, 6828–6830.

247 K. Chang and W. Chen, l-Cysteine-Assisted Synthesis of Layered MoS_2/Graphene Composites with Excellent Electrochemical Performances for Lithium Ion Batteries, *ACS Nano*, 2011, **5**, 4720–4728.

248 H. Xia, Y. Qian, Y. Fu and X. Wang, Graphene anchored with $ZnFe_2O_4$ nanoparticles as a high-capacity anode material for lithium-ion batteries, *Solid State Sci.*, 2013, **17**, 67–71.

249 B. Ren, W. Shen, L. Li, S. Wu and W. Wang, 3D $CoFe_2O_4$ nanorod/flower-like MoS_2 nanosheet heterojunctions as recyclable visible light-driven photocatalysts for the degradation of organic dyes, *Appl. Surf. Sci.*, 2018, **447**, 711–723.

250 S. Chakrabarty, A. Mukherjee and S. Basu, RGO-MoS_2 supported $NiCo_2O_4$ catalyst towards solar water splitting and dye degradation, *ACS Sustainable Chem. Eng.*, 2018, **6**, 5238–5247.

251 Y. Zeng, N. Guo, Y. Song, Y. Zhao, H. Li, X. Xu, J. Qiu and H. Yu, Fabrication of Z-scheme magnetic $MoS_2/CoFe_2O_4$ nanocomposites with highly efficient photocatalytic activity, *J. Colloid Interface Sci.*, 2018, **514**, 664–674.

252 S. Samakchi, N. Chaibakhsh and Z. Moradi-Shoeili, Synthesis of $MoS_2/MnFe_2O_4$ nanocomposite with highly efficient catalytic performance in visible light photo-Fenton-like process, *J. Photochem. Photobiol., A*, 2018, **367**, 420–428.

253 Y. Pang, L. Kong, D. Chen and G. Yuvaraja, Rapid Cr(VI) reduction in aqueous solution using a novel microwave-based treatment with MoS_2-$MnFe_2O_4$ composite, *Appl. Surf. Sci.*, 2019, **471**, 408–416.

254 Y. Jia, H. Ma and C. Liu, Au nanoparticles enhanced Z-scheme Au-$CoFe_2O_4/MoS_2$ visible light photocatalyst with magnetic retrievability, *Appl. Surf. Sci.*, 2019, **463**, 854–862.

255 W. Fu, X. Xu, W. Wang, M. Ye and J. Shen, In-situ growth of $NiFe_2O_4$/2D-MoS_2 p–n heterojunction immobilizing palladium nanoparticles for enhanced visible-light photocatalytic activities, *ACS Sustainable Chem. Eng.*, 2018, **6**, 8935–8944.

256 Y. Lu, B. Ren, S. Chang, W. Mi, J. He and W. Wang, Achieving effective control of the photocatalytic performance for $CoFe_2O_4/MoS_2$ heterojunction via exerting external magnetic fields, *Mater. Lett.*, 2020, **260**, 126979.

257 W. Fan, M. Li, H. Bai, D. Xu, C. Chen, C. Li, Y. Ge and W. Shi, Fabrication of $MgFe_2O_4/MoS_2$ Heterostructure Nanowires for Photoelectrochemical Catalysis, *Langmuir*, 2016, **32**, 1629–1936.

258 W. Xie, Q. Gao, D. Wang, Z. Guo, F. Gao, X. Wang, Q. Cai, S.-s. Feng, H. Fan, X. Sun and L. Zhao, Doxorubicin-loaded Fe_3O_4@MoS_2-PEG-2DG nanocubes as a theranostic platform for magnetic resonance imaging-guided chemo-photothermal therapy of breast cancer, *Nano Res.*, 2018, **11**, 2470–2487.

259 G. Wang, F. Zhou, T. Du, Z. Lu, Y. Ma, J. Mu, Y. Wang, Z. Zhang, H. Che, X. Zhang and R. Yu, Controlled assembly of $MnFe_2O_4$ nanoparticles on MoS_2 nanosheets by a facile sonochemical method, *J. Magn. Magn. Mater.*, 2019, **476**, 453–458.

260 B. Liu, C. Li, G. Chen, B. Liu, X. Deng, Y. Wei, J. Xia, B. Xing, P. a. Ma and J. Lin, Synthesis and Optimization of MoS_2@Fe_3O_4-ICG/Pt(IV) Nanoflowers for MR/IR/PA Bioimaging and Combined PTT/PDT/Chemotherapy Triggered by 808 nm Laser, *Adv. Sci.*, 2017, **4**, 1600540.

261 J. Yu, W. Yin, X. Zheng, G. Tian, X. Zhang, T. Bao, X. Dong, Z. Wang, Z. Gu, X. Ma and Y. Zhao, Smart MoS_2/Fe_3O_4 Nanotheranostic for Magnetically Targeted Photothermal Therapy Guided by Magnetic Resonance/Photoacoustic Imaging, *Theranostics*, 2015, **5**, 931–945.

262 Q. He, K. Rui, C. Chen, J. Yang and Z. Wen, Interconnected $CoFe_2O_4$-Polypyrrole Nanotubes as Anode Materials for High Performance Sodium Ion Batteries, *ACS Appl. Mater. Interfaces*, 2017, **9**, 36927–36935.

263 L. Wang, L. Zhuo, H. Cheng, C. Zhang and F. Zhao, Porous carbon nanotubes decorated with nanosized cobalt ferrite as anode materials for high-performance lithium-ion batteries, *J. Power Sources*, 2015, **283**, 289–299.

264 L. Lu, X. Jiao, J. Fan, W. Lei, Y. Ouyang, X. Xia, Z. Xue and Q. Hao, Cobalt ferrite on honeycomb-like algae-derived nitrogen-doped carbon for electrocatalytic oxygen reduction and ultra-cycle-stable lithium storage, *Electrochim. Acta*, 2019, **295**, 461–471.

265 B. Jiang, C. Han, B. Li, Y. He and Z. Lin, In-Situ Crafting of $ZnFe_2O_4$ Nanoparticles Impregnated within Continuous Carbon Network as Advanced Anode Materials, *ACS Nano*, 2016, **10**, 2728–2735.

266 D. Wu, Y. Wang, Y. Li, Q. Wei, L. Hu, T. Yan, R. Feng, L. Yan and B. Du, Phosphorylated chitosan/$CoFe_2O_4$ composite for

the efficient removal of Pb(II) and Cd(II) from aqueous solution: adsorption performance and mechanism studies, *J. Mol. Liq.*, 2019, **277**, 181–188.

267 D. Hussain, M. F. Siddiqui and T. A. Khan, Preparation of $NiFe_2O_4$/polythiophene nanocomposite and its enhanced adsorptive uptake of Janus green B and Fuchsin basic from aqueous solution: isotherm and kinetics studies, *Environ. Prog. Sustainable Energy*, 2020, **39**, 13371.

268 Y. Deng, X. Zhao, J. Luo, Z. Wang and J. Tang, Magnetic recyclable $CoFe_2O_4$@PPy prepared by in situ Fenton oxidization polymerization with advanced photo-Fenton performance, *RSC Adv.*, 2020, **10**, 1858–1869.

269 Q. Sun, M. Tang, P. V. Hendriksen and B. Chen, Biotemplated fabrication of a 3D hierarchical structure of magnetic $ZnFe_2O_4$/MgAl-LDH for efficient elimination of dye from water, *J. Alloys Compd.*, 2020, **829**, 154552.

270 M. F. A. Taleb, Adsorption and photocatalytic degradation of 2-CP in wastewater onto CS/$CoFe_2O_4$ nanocomposite synthesized using gamma radiation, *Carbohydr. Polym.*, 2014, **114**, 65–72.

271 X. Wu, W. Wang, F. Li, S. Khaimanov, N. Tsidaeva and M. Lahoubi, PEG-assisted hydrothermal synthesis of $CoFe_2O_4$ nanoparticles with enhanced selective adsorption properties for different dyes, *Appl. Surf. Sci.*, 2016, **389**, 1003–1011.

272 J. M. N. dos Santos, C. R. Pereira, L. A. A. Pinto, T. Frantz, É. C. Lima, E. L. Foletto and G. L. Dotto, Synthesis of a novel $CoFe_2O_4$/chitosan magnetic composite for fast adsorption of indigotine blue dye, *Carbohydr. Polym.*, 2019, **217**, 6–14.

273 X. Li, H. Lu, Y. Zhang, F. He, L. Jing and X. He, Fabrication of magnetic alginate beads with uniform dispersion of $CoFe_2O_4$ by the polydopamine surface functionalization for organic pollutants removal, *Appl. Surf. Sci.*, 2016, **389**, 567–577.

274 A. Homayonfard, M. Miralinaghi, R. H. S. M. Shirazi and E. Moniri, Efficient removal of cadmium(II) ions from aqueous solution by $CoFe_2O_4$/chitosan and $NiFe_2O_4$/chitosan composites as adsorbents, *Water Sci. Technol.*, 2018, **78**, 2297–2307.

275 Y.-d. Liang, Y.-j. He, Y.-h. Zhang and Q.-q. Zhu, Adsorption property of alizarin red S by $NiFe_2O_4$/polyaniline magnetic composite, *J. Environ. Chem. Eng.*, 2018, **6**, 416–425.

276 W. Sun, Y. Zhou, J. Liu, Y. Wang, L. Chen and Z. Tian, Polypyrrole/$NiFe_2O_4$ composites with improved hexavalent chromium removal from aqueous solution, *Polym. Compos.*, 2017, **38**, 2779–2787.

277 K. Shoueir, H. El-Sheshtawy, M. Misbah, H. El-Hosainy, I. El-Mehasseb and M. El-Kemary, Fenton-like nanocatalyst for photodegradation of methylene blue under visible light activated by hybrid green DNSA@Chitosan@$MnFe_2O_4$, *Carbohydr. Polym.*, 2018, **197**, 17–28.

278 Z. Jiang, K. Chen, Y. Zhang, Y. Wang, F. Wang, G. Zhang and D. D. Dionysiou, Magnetically recoverable $MgFe_2O_4$/conjugated polyvinyl chloride derivative nanocomposite with higher visible-light photocatalytic activity for treating Cr(VI)-polluted water, *Sep. Purif. Technol.*, 2020, **236**, 116272.

279 W.-K. Jo, S. Moru and S. Tonda, Magnetically responsive $SnFe_2O_4$/g-C_3N_4 hybrid photocatalysts with remarkable visible-light-induced performance for degradation of environmentally hazardous substances and sustainable hydrogen production, *Appl. Surf. Sci.*, 2020, **506**, 144939.

280 A. V. Humbe, S. D. Birajdar, J. M. Bhandari, N. N. Waghule, V. R. Bhagwat and K. M. Jadhav, Polyethylene glycol coated $CoFe_2O_4$ nanoparticles: a potential spinel ferrite for biomedical applications, *AIP Conf. Proc.*, 2015, **1665**, 050138.

281 P. H. Nam, L. T. Lu, P. H. Linh, D. H. Manh, L. T. Thanh Tam, N. X. Phuc, P. T. Phong and I.-J. Lee, Polymer-coated cobalt ferrite nanoparticles: synthesis, characterization, and toxicity for hyperthermia applications, *New J. Chem.*, 2018, **42**, 14530–14541.

282 S. A. Shah, M. H. Asdi, M. U. Hashmi, M. F. Umar and S.-U. Awan, Thermo-responsive copolymer coated $MnFe_2O_4$ magnetic nanoparticles for hyperthermia therapy and controlled drug delivery, *Mater. Chem. Phys.*, 2012, **137**, 365–371.

283 S. A. Shah, A. Majeed, K. Rashid and S.-U. Awan, PEG-coated folic acid-modified superparamagnetic $MnFe_2O_4$ nanoparticles for hyperthermia therapy and drug delivery, *Mater. Chem. Phys.*, 2013, **138**, 703–708.

284 X. L. Liu, E. S. G. Choo, A. S. Ahmed, L. Y. Zhao, Y. Yang, R. V. Ramanujan, J. M. Xue, D. D. Fan, H. M. Fan and J. Ding, Magnetic nanoparticle-loaded polymer nanospheres as magnetic hyperthermia agents, *J. Mater. Chem. B*, 2014, **2**, 120–128.

285 Y. Oh, N. Lee, H. W. Kang and J. Oh, In vitrostudy on apoptotic cell death by effective magnetic hyperthermia with chitosan-coated $MnFe_2O_4$, *Nanotechnology*, 2016, **27**, 115101.

286 S. Patra, E. Roy, P. Karfa, S. Kumar, R. Madhuri and P. K. Sharma, Dual-Responsive Polymer Coated Superparamagnetic Nanoparticle for Targeted Drug Delivery and Hyperthermia Treatment, *ACS Appl. Mater. Interfaces*, 2015, **7**, 9235–9246.

287 A. Esmaeili and N. Alizadeh Hadad, Preparation of $ZnFe_2O_4$–chitosan-doxorubicin hydrochloride nanoparticles and investigation of their hyperthermic heat-generating characteristics, *Ceram. Int.*, 2015, **41**, 7529–7535.

288 M. R. Phadatare, V. M. Khot, A. B. Salunkhe, N. D. Thorat and S. H. Pawar, Studies on polyethylene glycol coating on $NiFe_2O_4$ nanoparticles for biomedical applications, *J. Magn. Magn. Mater.*, 2012, **324**, 770–772.

289 E. Zachanowicz, J. Pigłowski, A. Zięcina, K. Rogacki, B. Poźniak, M. Tikhomirov, M. Marędziak, K. Marycz, J. Kisała, K. Hęclik and R. Pązik, Polyrhodanine cobalt ferrite (PRHD@$CoFe_2O_4$) hybrid nanomaterials-Synthesis, structural, magnetic, cytotoxic and antibacterial properties, *Mater. Chem. Phys.*, 2018, **217**, 553–561.

290 A. Esmaeili and S. Ghobadianpour, Vancomycin loaded superparamagnetic $MnFe_2O_4$ nanoparticles coated with

PEGylated chitosan to enhance antibacterial activity, *Int. J. Pharm.*, 2016, **501**, 326–330.

291 L. Luo, Q. Li, Y. Xu, Y. Ding, X. Wang, D. Deng and Y. Xu, Amperometric glucose biosensor based on $NiFe_2O_4$ nanoparticles and chitosan, *Sens. Actuators, B*, 2010, **145**, 293–298.

292 S. Q. Tang, S. J. Moon, K. H. Park, S. H. Paek, K.-W. Chung and S. Bae, Feasibility of TEOS Coated $CoFe_2O_4$ Nanoparticles to a GMR Biosensor Agent for Single Molecular Detection, *J. Nanosci. Nanotechnol.*, 2011, **11**, 82–89.

293 K. Asadpour-Zeynali and F. Mollarasouli, Novel electrochemical biosensor based on PVP capped $CoFe_2O_4$@CdSe core-shell nanoparticles modified electrode for ultra-trace level determination of rifampicin by square wave adsorptive stripping voltammetry, *Biosens. Bioelectron.*, 2017, **92**, 509–516.